Leibniz-Institut für
Astrophysik Potsdam

Universität Potsdam

VARIABILITY OF QUASARS DURING THE EPOCH OF HELIUM REIONIZATION

Patricia Aparicio Marcos
University of Potsdam

A thesis submitted for
the degree of *Master of Science*

Supervisor: Dr. Laura Keating

First Referee: Prof. Dr. Christoph Pfrommer

Second Referee: Prof. Dr. Philipp Richter

November 2022

CONTENTS

Statement of originality 2

Abstract 4

List of figures 7

List of tables 9

1 Introduction 11

1.1 The early Universe 12

1.2 Formation of the large-scale structures in the Universe 14

1.3 Intergalactic medium 15
  1.3.1 The reionization epoch 16
  1.3.2 Hydrogen reionization epoch 17
  1.3.3 Helium reionization epoch 19

1.4 Quasars 20
  1.4.1 Lyman α forest 21
  1.4.2 The He II Lyα forest 24
  1.4.3 Statistics of the Lyα forest 24
  1.4.4 The proximity effect 25
  1.4.5 The lifetime of quasars 30

1.4.6 The growth of supermassive black holes (SMBHs) 31
1.4.7 Variability of quasars 34

2 Simulations and codes **36**

2.1 Cosmological hydrodynamical simulations 36

2.2 1D radiative transfer algorithm 37

2.3 Optical depth calculations 39

3 Modelling proximity zones in the lightbulb model **42**

3.1 Results of the radiative transfer code 42

3.2 Proximity zone sizes and the lightbulb model 46
3.2.1 Variation of the proximity zone with the ionizing background 47
3.2.2 Variation of the proximity zone with the quasar lifetime 49
3.2.3 Variation of the proximity zone with the luminosity 51
3.2.4 Distribution of the proximity zone sizes 54

3.3 Summary 56

4 Modelling proximity zones in the variable model **57**

4.1 Behaviour of the He II fractions under variability 58

4.2 He II fluxes under variability 61

4.3 Behaviour of the proximity zones under variability 63

4.4 Summary 69

5 Conclusions and future work **70**

5.1 Results and conclusions 70

5.2 Caveats and future work 72

Bibliography **80**

A Zusammenfassung **82**

B Flickering models and proximity zone distributions **84**

STATEMENT OF ORIGINALITY

I hereby declare that the submitted Master's thesis is my own work and that, to the best of my knowledge, it contains no sources or resources other than the ones mentioned and acknowledged. During the writing of the thesis, I indicated all quotes, citations, and references that were taken from published or unpublished publications, such as books, journals, academic articles, newspapers, reports, etc. Furthermore, the research described in this thesis is based on work conducted at the Leibniz-Institut für Astrophysik Potsdam (AIP) and no part of this thesis has been submitted elsewhere for any other degree or qualification.

Copyright © 2022 by Patricia Aparicio Marcos. "The copyright of this thesis rests with the author. No quotations from it should be published without the author's prior written consent and information derived from it should be acknowledged".

ABSTRACT

The last major phase transition of the Universe occurred during the era of helium reionization, when hard photons produced by quasars powered by supermassive black holes doubly ionized the helium in the intergalactic medium. Furthermore, observations of the He II Lyman-α forest, a pattern of absorption lines in the spectra of these quasars, can provide insight into the ionization state of the intergalactic medium at these redshifts. Additionally, the regions closest to quasars have a higher degree of ionization caused by photons that come directly from them. These regions are called "proximity zones" and their size is determined by the properties of the intergalactic medium as well as the properties of the quasar itself. In this project, we aim to model the proximity zones and analyze their impact on the He II Lyman-α forest. A combination of cosmological hydrodynamical simulations and 1D radiative transfer algorithm is used to make mock observations of the He II Lyman-α forest, which is used to measure the sizes of the quasar proximity zones and compare it with observations. Two different approaches were used in this project. In the first approach, we consider constant sources, also called the "lightbulb model", in which the luminosity of the quasar remains constant at all times once the quasar becomes active. In the second approach, varying sources are assumed, known as the "flickering model", where the quasar's luminosity varies, as expected from changes in accretion rates. Our research demonstrates that a flickering light curve model with a large duty cycle of $f_{\rm duty} = 0.5$ and an on-time episode of 5 Myrs can explain the larger proximity zone sizes for a long quasar lifetime of $89 \leq t_{\rm Q} \leq 94$ Myrs. In contrast, a small duty cycle of $f_{\rm duty} = 0.1$ and an on-time episode of 1 Myr can explain the small proximity zones observed during the helium reionization epoch for long quasar lifetimes of $88 \leq t_{\rm Q} \leq 91$ Myrs. Thus, according to this model, black holes may grow for longer quasar lifetimes and small proximity zones may still be observed.

LIST OF PLOTS

1.1 Main stages in the evolution of the Universe since the Big Bang 14
1.2 Cosmic web obtained from dark matter-only simulations 16
1.3 Temperature as a function of redshift when the duration of He II reionization varies 16
1.4 Reionization process 18
1.5 Spectrum in the optical wavelength of QSO Q1422+231 at $z_{em} = 3.625$ 21
1.6 Spectra of the brightest quasar in the far UV, HE2347-4342 at z = 2.9 25
1.7 He II effective optical depth in function of redshift for 17 He II sightlines . . . 26
1.8 Sketch of the proximity zone of a QSO 26
1.9 Sketch of the transverse proximity zone of a QSO 27
1.10 He II proximity zone size R_{pz} as a function of the quasar absolute magnitude M_{1450} 28
1.11 Probability density function (PDF) of the observed proximity zones from Worseck et al. (2021) and Khrykin et al. (2019). 30
1.12 He II proximity zone size R_{pz} on quasar lifetime t_{Q} from (Khrykin et al. 2019) 31

2.1 Representation of optical depth and flux along the line of sight 40

3.1 Evolution of He II and He III fractions along one sightline with different ionization backgrounds 43
3.2 Dependence of He II and He III fractions along a sightline for different quasar lifetimes 44
3.3 He II / He III fractions, He II optical depth and He II flux as a function of distance in Mpc for a quasar lifetime of 45 Myrs 45
3.4 Representation of the proximity zone size 46
3.5 Variation of the proximity zone sizes with the UVB 47
3.6 He II proximity zone sizes as a function of the He II fraction $\mathrm{x}_{\mathrm{He}II,0}$ at fixed $\mathrm{t_Q} = 100$ Myr 48
3.7 Variation of the proximity zone sizes with the quasar lifetime 49

3.8 He II proximity zone sizes R_{pz} as a function of the quasar lifetime $\mathrm{t_Q}$ with a fixed $\mathrm{x_{HeII,0}} = 0.05$ and $\mathrm{x_{HeIII,0}} = 0.95$. 50
3.9 Variation of the proximity zone size with the luminosity 51
3.10 He II proximity zone sizes $\mathrm{R_{pz}}$ as a function of the absolute magnitude $\mathrm{M_{1450}}$. 52
3.11 Comparison of the proximity zone sizes R_{pz} as a function of magnitude M_{1450} between our RT code and that used in Worseck et al. (2021) for each model . . 53
3.12 Change in the He II transmission for five different sightlines with the same parameter model 54
3.13 Probability density function (PDF) of the proximity zones in our radiative transfer simulations for different quasar lifetimes and He II fractions 55

4.1 Illustration of the relevant parameters in the flickering model for a light curve. . 58
4.2 Evolution of the He II fraction as a function of the distance for a duty cycle of $f_{\mathrm{duty}} = 0.5$, a quasar on-time of $t_{\mathrm{on}} = 10$ Myr and a quasar off-time of $t_{\mathrm{off}} = 10$ Myr 59
4.3 Evolution of the He II fraction as a function of the distance for different duty cycles, $f_{\mathrm{duty}} \in \{0.8, 0.5, 0.2\}$, quasar on-times $t_{\mathrm{on}} \in \{15, 10, 5\}$ Myrs and quasar off-times $t_{\mathrm{off}} \in \{3.75, 10, 20\}$ Myrs 60
4.4 Evolution of the He II fluxes as a function of the distance for a duty cycle of $f_{\mathrm{duty}} = 0.5$, a quasar on-time of $t_{\mathrm{on}} = 10$ Myr and a quasar off-time of $t_{\mathrm{off}} = 10$ Myr 61
4.5 Evolution of the He II fluxes as a function of the distance for different duty cycles, $f_{\mathrm{duty}} \in \{0.8, 0.5, 0.2\}$, quasar on-times $t_{\mathrm{on}} \in \{15, 10, 5\}$ Myrs and quasar off-times $t_{\mathrm{off}} \in \{3.75, 10, 20\}$ Myrs 62
4.6 Proximity zones as a function of the quasar lifetime for the lightbulb and flickering quasar models with $f_{\mathrm{duty}} = 0.5$, $t_{\mathrm{on}} = 10$ Myrs and $t_{\mathrm{off}} = 10$ Myrs . . . 64
4.7 Evolution of the proximity zone as a function of the quasar lifetime for a fixed duty cycle $\mathrm{f_{duty}} = 0.2$ and varying on-time $\mathrm{t_{on}} \in \{5, 10, 15\}$ Myr 65
4.8 Evolution of the proximity zone as a function of the quasar lifetime for a fixed quasar on-time $\mathrm{t_{on}} = 15$ Myr and varying duty cycle $\mathrm{f_{duty}} \in \{0.2, 0.5, 0.8\}$ . . 67
4.9 He II proximity zone sizes $\mathrm{R_{pz}}$ as a function of the absolute magnitude $\mathrm{M_{1450}}$ in variability 68

B.1 Evolution of the proximity zones as a function of the quasar lifetime for different duty cycles and quasar on-times. 85
B.2 Probability density functions (PDF) of the proximity zone sizes for different duty cycles and quasar on-times. 86

TABLES

1.1 Sample of 24 quasars with He II proximity zones from Worseck et al. (2021) . . 29
1.2 Constraints on the QSO lifetime taken from Martini (2003) 32

CHAPTER 1

INTRODUCTION

One of the major changes in the ionization state of the Universe occurred in the *Epoch of Reionization*, going from a neutral to a completely ionized state. The presence of redshifted hydrogen lines observed in the spectra of quasars, discovered in 1963, shed new light on the understanding of the primitive Universe, as well as on the ionization state of the hydrogen atom, leading astronomers to conclude that these objects must be located at great cosmological distances. The Lyα transition is a strong resonant transition, which occurs between the ground and the first excited state of the hydrogen, and therefore when a photon of suitable energy encounters a hydrogen atom, it will be absorbed. In fact, quasars show a series of absorption lines at different wavelengths in their spectra from intervening hydrogen at different distances and, together with the quasar's continuum radiation form a very particular configuration called *Lyman* α *forest*. Hence, for a quasar very far away from us, along the line of sight, we would be sampling a significant fraction of the Universe's history and, by studying the Lyman α forest we are essentially reconstructing the history of structure formation.

Similar to hydrogen reionization, it is also possible to give some constraints to helium reionization by direct observations of the intergalactic He II Lyα forest, which appears redshifted to the far-ultraviolet (far UV) in the quasar spectra at z $\simeq$ 2 - 4. The steps in which neutral helium is thought to be completely ionized have much in common with hydrogen, although there is one fundamental difference: helium has a single and double ionization state. The change from He I to He II is very similar to that of hydrogen since it occurs almost at the same redshift and requires almost the same photon energy coming from the same sources, i.e, galaxies. However, the transition from He II to He III requires much more energetic photons, and the best source that can provide these photons are quasars, cosmological objects thought to be powered by supermassive black holes (SMBHs). In addition, a higher degree of ionization of hydrogen and helium is expected to be found around these sources. This region is called *the proximity zone* and its size depends not only on the properties of the intergalactic medium but also on the properties of the quasar itself.

Observations and theoretical studies of proximity zones have been conducted in the last two decades but because the spectral resolutions are limited, most studies have focused only on measuring or modeling the ‘sizes’ of the proximity zones. In observational work, the quasar proximity zone is often defined as the distance from the quasar to the first point along the line of sight where the transmitted flux drops below 10 % in a Gaussian smoothed spectrum, according to Fan et al. (2006). The proximity zone is therefore related to the quasar ionization front (I-front), which is further influenced by the quasar age and the neutral fraction of the intergalactic medium (IGM). Hence, these two physical quantities can be constrained by measuring the proximity zone size distribution and evolution (Chen & Gnedin 2021). In general, the He II proximity zones depend on the redshift. Some studies (Shull et al. 2010a; Zheng et al. 2015; Worseck et al. 2021) suggest that some quasars show He II proximity zones spanning a wide range of sizes from 2 pMpc < R_{pz} < 15 pMpc (proper Mpc). However, at higher redshifts, about 1 - 2% of old (30 million years) quasars were found to have extremely small H I proximity zone sizes (< 1 pMpc) (Chen & Gnedin 2021).

The main goal of this thesis is to model the proximity zones around quasars at redshift z = 3 and analyze its impact on the He II Lyα forest by post-processing sightlines extracted from a cosmological hydrodynamic simulation with a 1D radiative transfer code. The results are expected to provide a better understanding of the physical processes governing the growth of supermassive black holes through the study of the lifetime of quasars. This thesis is divided as follows: section 1 provides a brief theoretical introduction to the history and evolution of the early Universe, as well as the thermal history of the intergalactic medium (IGM) and the properties of quasar spectra. The cosmological hydrodynamic simulation as well as the radiative transfer used in this project are discussed in the section 2. We present the results of our first attempt to model proximity zones using the lightbulb model in section 3. Additionally, the analysis of proximity zones under variability can be found in section 4. In the final section 5, the conclusions are presented along with future prospects. Throughout this work, we assume a flat ΛCDM cosmology with the following set of cosmological parameters ($\Omega_{\rm m}$, $\Omega_{\rm b}h^2$, Ω_Λ, h, σ_8, n) = (0.26, 0.024, 0.74, 0.72, 0.85, 0.95) respectively.

1.1 The early Universe

Cosmology has always pursued a deep understanding of the physical laws that govern the Universe. Explaining its origin, tracing the most important events that have occurred during its evolution, and determining its content are the most fundamental and ambitious goals of this field. Today, the standard cosmological theory that has managed to accurately describe the Big Bang and the abundance of primordial elements, the large-scale structure in the distribution of galaxies, and the accelerated expansion of the Universe, is the *Lambda Cold Dark Matter* (ΛCDM) model. In the ΛCDM model, the Universe consists of *dark energy*, which is described with the cosmological constant Λ. This constant is responsible for inducing what is commonly called “gravitational repulsion”, a negative pressure that causes accelerated expansion and contributes about $\sim$ 68.3% (Ade et al. 2016) of the total mass-energy composition of the Universe at redshift

0. Subsequently, the *cold dark matter* is known for being non-baryonic, cold, collisionless, and dissipationless and its only way of interaction is via gravity, providing the 26.8% (Ade et al. 2016) of the total energy density. This form of matter has been supported by observations because it might explain some features found primarily in clusters and galaxies, e.g. flat rotation curves. Lastly, the visible baryonic matter accounts for the remaining 4.9% (Ade et al. 2016) and is made of leptons and hadrons. To explain the physical properties of the Universe, cosmology also relies on the *cosmological principle*, which states that the Universe is homogeneous, i.e. the same at every point, and isotropic, i.e., the same in all directions at sufficiently large scales.

According to the ΛCDM model, the history of the Universe began $\sim$ 13.8 Gyr ago, when space-time itself emerged from an initial phase of singularity, this event is known as the *Big Bang*. In $\sim 10^{-35}$ seconds after the Big Bang, *cosmic inflation*, driven by the cosmological constant Λ, caused a very hot, dense Universe to grow exponentially and cool down adiabatically (Tsujikawa 2003). During the inflation phase, the change of state of the *inflation field* generated a strongly accelerated expansion that led the Universe to become homogeneous, isotropic, and flat. Each point in space experiences *quantum fluctuations* in the amount of energy, caused by the constant creation and destruction of virtual particles as explained by Werner Heisenberg's Uncertainty Principle (Heisenberg 1927). During inflation, the exponential growth of the scale factor caused these quantum fluctuations to expand on macroscopic scales, producing near-scale invariant, Gaussian perturbations in the cosmic energy density. At later epochs, under the gravitational force, these fluctuations would become sites of structure formation.

Immediately after the cosmic inflation, the Universe consisted of a uniform bath of fundamental particles, such as quarks, electrons, their anti-particles, neutrinos, photons, and dark matter particles. Quarks tied each other together in trios, forming protons and neutrons, which are the basic constituents of atomic nuclei. About three minutes after the Big Bang, those protons and neutrons combined to form mainly hydrogen and helium. Up to this point, the density and the temperature of the Universe were extremely high, and these particles were tightly coupled to photons in a very hot photon-baryonic plasma. The interaction between particles was so frequent that photons could not travel freely, driving the Universe to be opaque. The decoupling between baryonic matter and photons could not occur until the Universe had expanded further and cooled down to a temperature of $\sim$ 3000 K, at approximately $z \sim 1100$ (Ryden 2003), a phase known as the *Recombination epoch*. At that point, protons and electrons could finally combine to form atoms of neutral hydrogen marking the beginning of a new period known as the *Dark ages*, where the vast Universe was cold and neutral.

The decoupling had two important effects: the first one is that photons experienced the last scattering and were able to propagate freely in the cosmos, imprinted in the Cosmic Microwave Background (CMB) which can be seen today (Ade et al. 2016). This radiation is *the first light of the Universe* and has been studied in depth using space-based experiments such as COBE, WMAP, or Planck. At scales smaller than about one degree, the CMB shows an oscillation pattern of sound waves due to the interplay between gravity, which pulled together the photon baryonic plasma, and radiation pressure, which pushed it away, causing a series of compressions

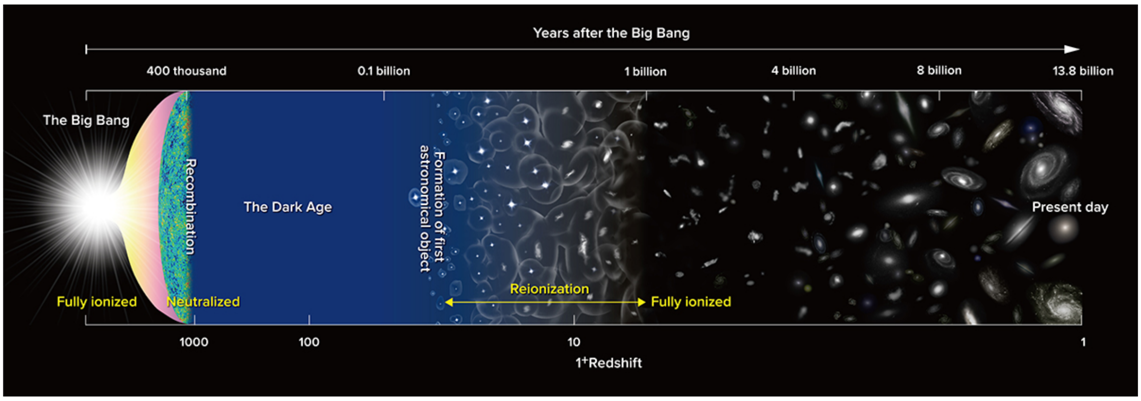
Years after the Big Bang
400 thousand
0.1 billion
1 billion
4 billion
8 billion
13.8 billion
The Big Bang
Recombination
The Dark Age
Formation of first astronomical object
Present day
Fully ionized
Neutralized
Reionization
Fully ionized
1000
100
10
1
1+Redshift

Figure 1.1: This diagram represents the main stages in the evolution of the Universe since the Big Bang, about 13.8 Gyrs ago. Credit: National Astronomical Observatory of Japan (NAOJ) https://www.nao.ac.jp/en/

everywhere in the fluid. This results in the pattern of sound waves that is visible in the central part of the power spectrum. From the shape of the oscillations, we can obtain information about the amount of baryonic matter relative to the amount of dark matter. Another effect is that baryons and dark matter began to undergo gravitational collapse. Denser concentrations of both types of matter grew denser and more massive, and since the dark matter had already created a network of dense and empty structures, the ordinary matter could fall into those denser concentrations of dark matter. Besides, baryonic matter heated up and emitted radiation, causing an even further sink into that highly dense regions. These gave rise to a substructure network of sheets (along one axis), filaments (along two axes), and subsequently halos (along three axes) of dark matter known as the *cosmic web*. This constitutes the skeleton for the later birth of stars, and galaxies, leading to the end of the Dark Ages and the beginning of the *Epoch of Reionization* (EoR). The process of ionization plays a fundamental role in the physical processes that shaped the galaxies of different luminosities and masses today, as the first sources provide seeds for the subsequent formation of larger galaxies due to the hierarchical structure formation of the Universe. [1]

1.2 Formation of the large-scale structures in the Universe

The CDM theory and, subsequently, the observations of the CMB led to the creation of the theory of the Hierarchical structure Formation (Press & Schechter 1974). The growth of perturbations can be divided into linear and non-linear regimes. In the linear regime, we can describe the Universe as an ideal pressureless fluid of particles, since in this regime there are no dark matter particle stream crossings or baryonic shocks. Solving the continuity and the Euler equations for a fluid, two solutions for the evolution of the perturbations are obtained, of which the growing one dominates. Over time, these small density perturbations grew becoming significantly denser than the mean density of the Universe, and the structure formation entered the nonlinear regime. In this regime, the clumps of dark matter experienced a gravitational collapse, giving rise to halos and voids. Up to this point, the baryonic matter, decoupled from radiation, started to feel the gravitational attraction from the dark matter haloes and sank into these potential wells until their density was sufficient that collapse under gravitational force. In this scenario, dark matter continued orbiting the halo meanwhile the baryonic matter was collapsing to the center of the systems, losing energy in the collision processes. Since the angular momentum must be conserved, the baryons evolved to a rotational configuration leading the gas to be distributed in a rotation disk system, commonly called *protogalaxies*. The gas in these configurations cool down and became denser, giving rise to the birth of the first stars. At later times, these structures would evolve due to internal and external processes such as gas accretion or different types of merging, and eventually, the gravitational force would put galaxies together in groups and clusters, forming a hierarchical structure (White & Rees 1978; Press & Schechter 1974).

---

[1] https://pages.aip.de/pfrommer/Lectures/cosmology.pdf

1.3 Intergalactic medium

The Universe has evolved from smooth conditions at z=1100 when the CMB was emitted, to the complex structures we see today. The baryonic matter that has not collapsed into objects such as stars, black holes, or galaxies is called the Intergalactic Medium (IGM) and its understanding is fundamental for many fields of astrophysics. For example, the IGM is used to measure the total ionizing photon production of galaxies (Nanayakkara et al. 2020) or to study the galaxies' stellar nucleosynthesis (Ferrara et al. 2000). Furthermore, it is thought that the IGM is the source of building blocks for galaxy formation and a gas reservoir from which galaxies can obtain gas for star formation. Galaxies and quasars, on the other hand, emit a huge number of ionizing photons that, if they escape into the intergalactic medium, can alter the state of the gas and, as a result, impact their own evolution. We can easily conclude that almost all the baryons in the IGM are placed in between galaxies, but this idea is observationally supported. From CMB fluctuations and the primordial abundance of deuterium, the cosmic density of baryons was calculated with a value of $\Omega_{b,0}h^2 = 0.0224 \pm 0.0002$ (Inomata et al. 2018). On the other hand, large-scale studies of galaxies in the nearby Universe have allowed us to create the galaxy *luminosity* function in different wavelength bands. The latter may be converted into a galaxy *mass* function using the mass-to-light ratio. The further integration of the mass function yields a result of $\Omega_{stars,0}h^2 = 0.0027 \pm 0.0005$ (Fukugita & Peebles 2004). When both results are compared, it is clear that stars account for only 6% of the total baryon density today. Because planets are meaningless in this context and interstellar gas boosts the proportion of baryons within the galaxy by less than a factor of 1.3, we may deduce that the vast majority of baryons must live in the space between galaxies.

In general, knowing the temperature of IGM has become quite an interesting task, as it may restrict the processes that occur in IGM, specifically the reionization history. When an ionization front swept and reionized intergalactic hydrogen, this ionization photo-heated the cold IGM. This heat injection was around 17 - 25 $\times 10^3$ K but may vary depending on the hardness of the incident spectrum and the speed of the ionization front (McQuinn 2016). The helium reionization epoch marks another important heating event, driven by the harder emission of quasars.

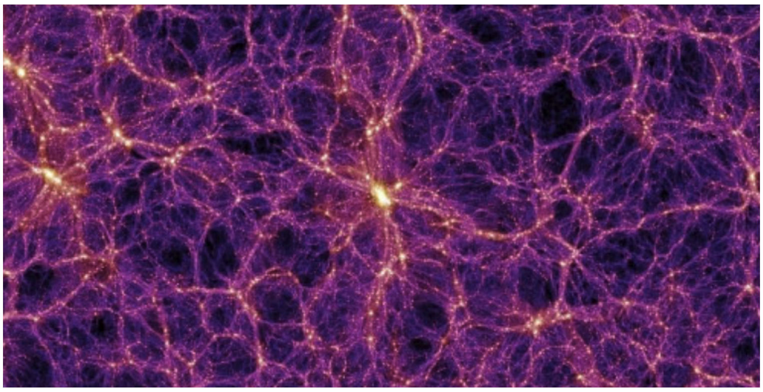

Figure 1.2: An illustration of the cosmic web obtained from dark matter-only simulations. The intergalactic gas follows the same pattern. It consists of filaments of galaxies and empty desolate voids, which occupy the vast majority of the volume of the Universe (Springel et al. 2005).

During this era, He III bubbles are blown around quasars and the IGM is additionally heated by 5-10 $\times 10^3$ K (McQuinn et al. 2009). After these events, the IGM cooled, mainly through the adiabatic cosmic expansion and through Compton cooling off of the CMB. In general, the temperature measurements rely on the width of Lyα absorption features from the low-density IGM being broader with higher temperatures, because of both thermal broadening and the broadening owing to pressure effects. This is one of the reasons why studying the Lyα forest is very important to constrain the properties of the IGM.

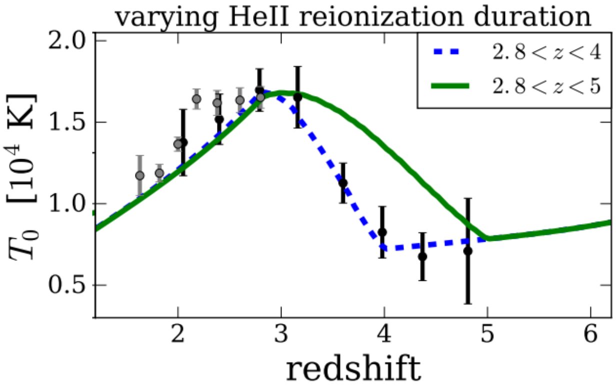

Figure 1.3: This figure shows the temperature variation with redshift as the duration of He II reionization varies. The peak temperature in the models (and probably also in the data) is related to the reionization of He II (Sanderbeck et al. 2016).

1.3.1 The reionization epoch

As seen in the section 1.1, the epoch of reionization corresponds to a phase transition that happened in the Universe when the ionization state of the intergalactic gas changed from neutral to highly ionized plasma. During this epoch, ionized regions spread around the sources, combine, and expand until the IGM is completely ionized. The velocity of the ionization fronts depends on the optical depth: ionization fronts expand slowly in dense regions and they spread more quickly in less dense regions. In order to describe specifically how the ionization takes place in the IGM, many numerical simulations have been carried out and one of the most interesting scenarios is described in Gnedin (2000). According to the latter, the ionization process may have happened in three different stages:

- ***Pre-overlap phase***: where the individual ionizing sources turn on and start to ionize their surrounding. Because of the hierarchical structure formation, the high-density regions host star-forming galaxies, where very high recombination rates mediate the propagation of the ionization fronts. After emerging from these high-density regions, photons start to ionize the low-density voids meanwhile those underdense areas which do not have sources remain neutral and unchanged. This leads to a two-phase medium made up of highly ionized and neutral regions. In this stage, the photon density in the ionized regions presents a high level of inhomogeneity and depends on the distance to neighboring sources. When these neighboring ionized regions start to merge, the reionization process moves to the next phase.

- ***Overlap phase***: since each point in the ionized region is exposed to all ionizing sources, the ionizing intensity increases rapidly, resulting in the expansion of the ionized region into a previously neutral, low-density gas. As the ionized regions merge, the intensity of the ionizing radiation increases, and the ionization gradually becomes more homogeneous. The hierarchical structure formation accelerates this phase transition because, at the respective redshift range, the rate of galaxy formation increases rapidly with time, increasing the ionizing intensity. Due to this process, the low-density regions of the IGM become highly ionized, while the ionizing radiation spreads to all regions except the self-shielded high-density areas. At this point, the reionization has taken place.

- ***Post-overlap phase***: neutral, self-shielded high-density regions are associated with Lyman Limit systems, also called damped Lyman α systems. The mean ionizing intensity increases as galaxy formation proceeds, gradually ionizing these previously shielded high-density regions, and becoming more uniform. The process of reionization can be visualized in figure 1.4 below.

Furthermore, since hydrogen and helium atoms in the IGM have different ionization potentials, the reionization process can also be divided into two steps: hydrogen reionization and helium reionization.

1.3.2 Hydrogen reionization epoch

As described above, at the end of the Age of Recombination the Universe moved into the Dark Age epoch. It is estimated that this period lasted about 400 million years, followed by the creation of the first stars and galaxies. The hydrogen and singly helium reionization began (H I $\rightarrow$ H II; He I $\rightarrow$ He II) when these stellar populations of newborn galaxies started emitting ionizing

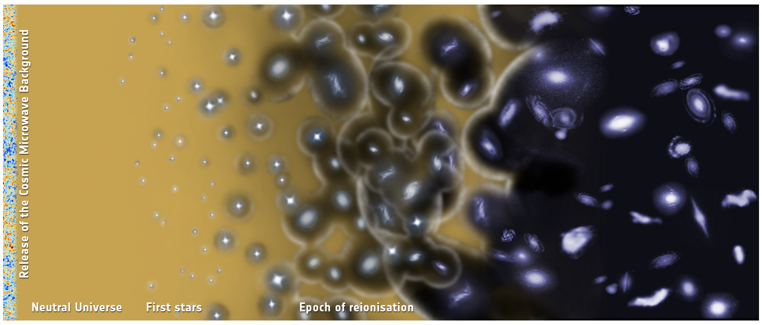

Figure 1.4: Illustration that represents how reionization occurred. Credit: ESA - C.Carreau.

radiation with energy $\geq$ 13.6 eV, as seen previously. Following the above explanation (section 1.3.1), the isolated H II and He II regions formed around individual galaxies started to grow, gradually expanded, and eventually overlapped, covering the entire Universe.

It is still unknown exactly when hydrogen reionization started and how long it took. Simulations may produce many reionization scenarios, but only some of them provide real observational constraints. One of the most accepted observations for constraint at the beginning of this epoch comes from the analysis of the secondary anisotropies of the CMB. The observation of these anisotropies includes measurements of the IGM's optical depth τ_e caused by Thomson scattering of CMB photons on free electrons produced during hydrogen reionization. The most recent measurements from Planck (Aghanim et al. 2020) yield an optical depth τ_e= 0.0561 $\pm$ 0.0071 and z_{reion}= 7.82 $\pm$ 0.71 respectively, although these values are obtained under the assumption of an instantaneous HI reionization. Despite this, to this day, there is still a struggle to obtain good constraints for the beginning of the era of hydrogen reionization, as the number of bright high redshift quasars decreases rapidly at z $\geq$ 5, (Wang et al. 2019), and the IGM becomes denser and neutral, making it difficult for us to obtain information. Another challenge is the fact that it is still unclear whether the number density of the observed star-forming galaxies at z $\sim$ 6 is sufficient to reionize HI. On the other hand, the chemical and radiative feedback of the first stars onto their surroundings is also important for constraining their impact on reionization. Nowadays, a possible observation of the redshifted 21 cm spin line of neutral hydrogen could be one of the most promising methods for studying the beginning of hydrogen reionization (Pritchard & Loeb 2012) although there is still no convincing detection of the 21 cm absorption or emission during reionization. Additionally, by means of the kinetic Sunyaev-Zel'dovich (kSZ) effect (Sunyaev & Zeldovich 1980), reionization history is also encoded in the secondary anisotropy temperature of the CMB. In ionized regions, photons from the CMB receive energy boosts by high-energy electrons with large peculiar velocities since these electrons interact with CMB photons using inverse Compton scattering. Thus, the kSZ power spectrum on small scales reflects the topology of reionized regions and may provide a constraint in the duration of the hydrogen reionization epoch, e.g, in this recent work Reichardt et al. (2021) they provide an upper limit of $\Delta z < 4.1$.

On the other hand, the most reliable observational indicator that marks the end of the HI reionization is the HI Lyα forest in high-redshift quasar spectra. The Lyman α transition is observed in absorption when neutral hydrogen in the ground state absorbs a photon with energy $\geq$ 13.6 eV, moving into the first excited state. Since neutral hydrogen has a "bound" electron to its proton, it can absorb and emit radiation through bound-bound radiative transitions between energy levels. When hydrogen is ionized, it can no longer absorb radiation through bound-bound or bound-free transitions (since it is already "free" of its electron). As the quasar radiation travels through the IGM, it is continually redshifted by the expansion of the Universe, thus if photons with wavelengths shorter than Lyα are redshifted to $\lambda_{rest} = 1216$ Å, they are absorbed by neutral hydrogen clouds. During this process, thin absorption lines appear blueward of the Lyα emission line in the spectrum of a quasar, and the set of these thin lines is called the HI *Lyα forest*. If the IGM presents a significant amount of neutral hydrogen clouds, we will see an opaque and saturated region in the quasar spectrum called a *Gunn-Peterson trough* (Gunn & Peterson 1965). Several studies, e.g, (Becker et al. 2015; Miralda-Escude 1998; Wang et al. 2020), pointed out that quasars that have been observed above z $\simeq$ 6 exhibited the characteristic GP trough in their spectra, while the HI Lyα forest was detected in the spectra of quasars placed at lower redshift, suggesting that hydrogen reionization is almost complete by z $\simeq$ 5.5 - 6, corresponding to the time when the HII regions of individual sources overlapped according to Gnedin (2000).

To sum up, the epoch of hydrogen reionization is, in essence, very inhomogeneous and complex, as it is affected by the properties of the sources, their feedback to the environment, their clustering properties, and our technological ability to develop surveys that help us to detect them at high redshifts.

1.3.3 Helium reionization epoch

There are two significant differences between helium (He I $\rightarrow$ He II $\rightarrow$ He III) and hydrogen's reionization morphology. First, helium reionization is thought to be a two-step process. Since HI and HeI have very similar ionization potentials, i.e. hν $\geq$ 13.6 eV for HI $\rightarrow$ H II and hν $\geq$ 24.6 eV for He I $\rightarrow$ He II, the first ionization of helium could likely happen at the same time as hydrogen with photons coming from the same sources at similar redshifts (z $\geq$ 6). The second difference lies in the fact that for doubly ionized helium, He II $\rightarrow$ He III, the sources must be more energetic than those designed to reionize hydrogen (star-forming galaxies) since this transition is characterized by an ionization potential of hν $\geq$ 54.4 eV. The best candidates responsible for doubly ionizing helium are quasars. Semi-analytic calculations along with full hydrodynamical and radiative transfer simulations (McQuinn et al. 2009; Caleb et al. 2019) predicted that the reionization of He II relative to hydrogen has been delayed to z$\simeq$ 3 - 4, which is consistent with an increase in the density of quasars at z $\simeq$ 3 and hardening of the intergalactic ionizing background (Furlanetto & Oh 2008).

As is the case with hydrogen reionization, constraints on He II reionization can be obtained from direct observations of the intergalactic He II Lyα forest absorption (λ_{rest}= 303.78 Å) in the spectra of z $\simeq$ 3 - 4 quasars, which are presently only achievable in the far-UV, e.g. with

Cosmic Origins Spectrograph (COS) onboard Hubble Space Telescope (HST). In some projects (Worseck et al. 2016; McQuinn & Switzer 2010) a dramatic reduction was observed in the opacity of the He II Lyα forest at redshift z $\leq$ 3, which is consistent with the tail end of He II reionization, as predicted by numerical simulations (McQuinn et al. 2009). Although, some of these models also predict a completely saturated He II Lyα forest absorption in the quasar spectra above z $>$ 3.2, which is inconsistent with the detected optically thin regions of IGM at z $\geq$ 3.5, e.g (Worseck et al. 2011; Makan et al. 2021). This might indicate that He II reionization began much earlier than simulations suggest and that there must be sources at z $\geq$ 4 providing the hard photons needed to reionize intergalactic helium by z $\geq$ 3.5. It appears that faint quasars can be found up to z = 7.5 (Wang et al. 2021) and might be responsible for the early He II reionization. However, according to alternative scenarios, He II reionization may also be aided by other, more exotic sources of energetic photons, such as redshifted X-ray radiation from primordial black holes or globular clusters (Power et al. 2009), thermal emissions from shock-heated gas during structure formation at high redshifts or high-redshift mini-quasars (Hao et al. 2015). The sensitivity of HST and COS, however, makes it very difficult to study intergalactic He II Lyα forest absorption in the spectra of z $\geq$ 4 quasars directly. In this sense, we should use another indirect method to constrain the helium reionization at high redshifts, for instance, one option is to measure the temperature of the IGM which is expected to increase dramatically during He II reionization, which can be seen in figure 1.3. Nevertheless, most of the models assume that quasars drive helium reionization, so they depend on several key quasar parameters, such as luminosity and abundance, which determine the amount of He II ionizing photons available for the reionization of helium atoms within a specified period.

1.4 Quasars

As a result of the hierarchical structure formation model, we now understand the formation of galaxies and galaxy clusters in the Universe. In the haloes of dark matter, these complex systems were equilibrated, and then, by recycling the gas reservoir, clumps of sufficiently fragmented, dense, and cool gas collapsed gravitationally and formed stars. However, it is believed that most galaxies have experienced another active phase in the evolution of their core regions, known as the *quasar phase*. Quasi-stellar objects (QSOs), commonly called Quasars, have dramatically changed our understanding of the evolution of galaxies and, after several years of research, we know that they are compact, extremely bright nuclei of distant galaxies, whose radiation is produced by mechanisms completely different from those of stars. Supermassive black holes (SMBHs) are believed to be the engines of quasar activity located at the center of the galaxy. Its enormous gravitational pull brings the gas closer to the event horizon, however, before the gas can fall on the SMBH, it must first lose its angular momentum. In this context, accretion disks (Salpeter 1964; Shakura & Sunyaev 1973) provided the necessary mechanism whereby gravity spirals the gas towards the event horizon along a line called *tendex line*, while friction heats the gas to extreme temperatures. Thus, the gravitational energy of the gas is converted into photons that are emitted mostly at UV and X-ray wavelengths. The total luminosity of quasars produced by gas accumulation at SMBH is typically $L = 10^{46}\mathrm{erg\,s^{-1}}$, which is about

100 times the energy emitted by all the stars in a typical galaxy (Merloni & Heinz 2013). This luminosity corresponds, considering asymmetrical spherical configuration, to an SMBH with a mass around $M = 10^8 M_\odot$, provided that the SMBH is irradiated at the Eddington luminosity (maximum luminosity a body may have when there is a balance between the force of radiation acting outward and the gravitational force acting inward).

1.4.1 Lyman α forest

Since QSOs are some of the brightest objects in the Universe and can therefore be observed at high redshifts (Wang et al. 2021; Cool et al. 2006; Bañados et al. 2018), we can use their spectra to infer information about the IGM. The light of the quasars, on its way to our telescopes on Earth, traverses vast expanses of space. Any gas, in or between galaxies, that happens to be between the QSO and us leaves its signature on the QSO spectrum in the form of absorption lines. QSO absorption line spectroscopy has been a rich field of study, both observationally and theoretically.

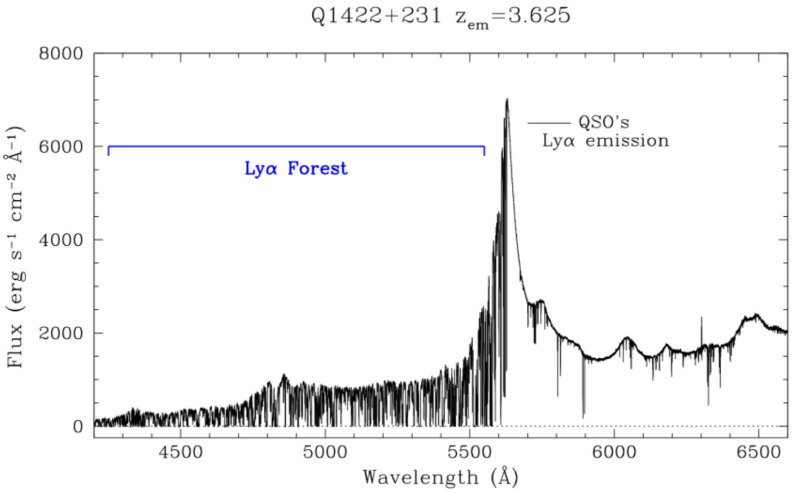

Figure 1.5: Spectrum in the optical wavelength of QSO Q1422+231 at $z_{em} = 3.625$, recorded with HIRES (High-Resolution Echelle Spectrograph) on the Keck I telescope. Credit: https://ned.ipac.caltech.edu/level5/March03/Pettini/Pettini3.html

As we can see in figure 1.5, the spectrum is just a plot of flux (energy per unit time) vs wavelength. The typical units of flux are erg $\mathrm{s}^{-1}\mathrm{cm}^{-2}$ Å and wavelength is in Å. Furthermore, the QSO intrinsic spectrum consists of a power-law continuum, and broad (several thousand $\mathrm{km\ s}^{-1}$) emission lines. We can infer the emission redshift through the relation $\lambda_{obs} = \lambda_0 \times (1 + z_{em})$, where λ_{obs} is the observed wavelength of the emission line and λ_0 is its wavelength at rest. We can also notice that the strongest emission line is the line of the Lyman α, which corresponds to a transition from the first excited level to the ground state. In addition, for this object $\lambda_{obs} = 5622$ Å, $\lambda_0 = 1216$ Å and $z_{em} = 3.625$ which means those photons were emitted around 12.1 million years ago. The spectrum also shows many narrow absorption lines and it is these lines that are the focus of QSO absorption spectroscopy. Absorption lines at wavelengths greater than that of the Lyα emission can be usually identified as the strongest lines of the most abundant elements, i. e. OI, CII, CIV, MgII, SiII, or FeII in well-defined redshift systems. These are the *metal-line* systems. On the other hand, only a small fraction of lines at wavelengths shorter than the Lyα emission can be identified as metal line transitions but they are just hard to see because of the forest. Most of them are individual Lyα lines that arise in clouds where the metallicity is too low to produce metal lines. In this case, the only spectral signatures we see are transitions from the Lyman series of H I. This is known as *Lyα forest*. There exist also Lyβ, Lyγ, Lyδ, etc. H I absorption forest corresponding to the upper n-Rydberg state. As *n* increases, it spreads out along a shorter path, falling on the lower redshift, so the forest is smaller with less absorption level, although the latter is just due to the lower oscillator strengths rather than the path length.

The modern paradigm of the Lyα forest, or IGM, is that the observed opacity results from fluctuations in the underlying dark matter density. The baryons, which are ionized with an ionization state determined by photoionization from extragalactic UV background (EUVB), are able to carry out the tracing of these dark matter fluctuations to yield the observed Lyα spectra. This paradigm leads to the formalism known as *the fluctuating Gunn-Peterson approximation* (FPGA) and we can derive it as follows (Dijkstra M. 2019). The Lyα optical depth at the line center is:

$$\tau_0 = \frac{\pi e^2}{m_e c\sqrt{\pi}} \frac{N_{\rm HI} f_{\rm Ly\alpha}}{\Delta\nu_{\rm D}} \tag{1.1}$$

where e and $m_{\rm e}$ are the electron charge and the electron mass, c the speed of light, $f_{\rm Ly\alpha}$ is the oscillator strength and, $\Delta\nu_D$ the width of the Doppler broadening. Expressing the $N_{\rm HI}$ column density as

$$N_{\rm HI} = n_{\rm HI}\Delta r \tag{1.2}$$

with Δr an interval in space and $n_{\rm HI}$ the gas density. In cosmology, we can relate distance to redshift as:

$$\Delta r = \frac{c\Delta z}{H(z)(1+z)} \tag{1.3}$$

then:

$$\tau_0 = \frac{\pi e^2}{m_{\rm e}} \frac{n_{\rm HI}\Delta z f_{\rm Ly\alpha}}{\Delta\nu_{\rm D} H(z)(1+z)} \tag{1.4}$$

Since absorption occurs over a small redshift interval, it is possible to express $\frac{\Delta z}{1+z} = \frac{\Delta\nu_{\rm Ly\alpha}}{\nu_{\rm Ly\alpha}}$ and identify $\Delta\nu_{\rm D}$ with $\Delta\nu_{\rm Ly\alpha}$, i.e, the line width is given by the cosmic expansion. In the IGM we only need to consider two processes (neglecting the contribution of helium): photoionization ($H^0 + h\nu \rightarrow H^+ + e^-$) and recombination. In a post-reionization IGM scenario, the ratio between the densities of two successive ionization stages (in this case $n_{\rm HI}$ and $n_{\rm HII}$) is given by the balance between the number of ionizations and the number of recombinations per unit volume per unit time, then:

$$\frac{n_{\rm HII}}{n_{\rm HI}} = \frac{\Gamma}{n_{\rm e}\alpha_{\rm HI}(T)} \tag{1.5}$$

where Γ is the photoionization rate, i.e, how many H atoms are becoming ionized per second, $\alpha_{\rm HI} = f(T)$ cm^3 s^{-1} is the recombination coefficient and $n_{\rm e} = n_{\rm HII} = 1 - n_{\rm HI}$ is the number density of free electrons. The latter equation assumes photoionization equilibrium and $x_{HI} < 1$, which holds as $\Gamma^{-1} \sim 30.000$ years (valid for a large range of redshifts). However, in regions that have been shocked heated to $10^5 - 10^6$ K, that equation is not valid because the collisional ionization becomes important (McQuinn 2016). Altogether now,

$$\tau_0 = \frac{\pi e^2 f_{\rm Ly\alpha}}{m_{\rm e}\nu_{Ly\alpha}}\frac{1}{H(z)}\frac{\alpha(T)n_{\rm HII}n_{\rm e}}{\Gamma} \tag{1.6}$$

In order to link the gas density with the dark matter density, we introduce the overdensity δ where:

$$\rho = \bar{\rho}(1+\delta) \tag{1.7}$$

with ρ and $\bar{\rho}$ the dark matter and the cosmic mean densities. We consider a gas made purely of hydrogen and helium, with mass fractions X and Y. To describe its ionization state, we define $(x, y_{\rm II}, y_{\rm III}) \equiv (n_{\rm HII}/n_{\rm H}, n_{\rm HeII}/n_{\rm He}, n_{\rm HeIII}/n_{\rm He})$:

$$n_{\rm HII} = \frac{\rho_{crit}\Omega_{\rm b}}{m_p}Xx(1+\delta)(1+z)^3 \tag{1.8}$$

Considering a similar expression for n_e including helium:

$$n_{\rm e} = \frac{\rho_{crit}\Omega_b}{m_{\rm p}}[Xx + 0.25Y(y_{\rm II} + 2y_{\rm III})](1+\delta)(1+z)^3 \tag{1.9}$$

where it has been used the fact that a helium atom weighs approximately $4m_{\rm p}$. For gas with $T \sim 10^4$ K, which is the temperature expected for a photoionized medium, $\alpha(T)$ is a power-law of the form $\alpha(T) \approx \alpha_0 T^{-0.7}$ (Hui & Gnedin 1997). Finally, assuming that the IGM gas follows a power law temperature-density relation $T = T_0(1+\delta)^\beta$ (Hui & Gnedin 1997), the FGPA expression becomes:

$$\tau = A(z)(1+\delta)^{2-0.7\beta} \tag{1.10}$$

where the opacity fluctuates with the local overdensity. The $A(z)$ term is proportional to $(1+z)^6/[H(z)\Gamma]$ or:

$$A(z) \equiv \frac{\pi e^2 f_{\mathrm{Ly}\alpha}}{m_{\mathrm{e}} \nu_{\mathrm{Ly}\alpha}} \left(\frac{\rho_{\mathrm{crit}} \Omega_{\mathrm{b}}}{m_{\mathrm{p}}} \right)^2 \frac{1}{H(z)} Xx \left[Xx + 0.25Y(y_{\mathrm{II}} + y_{\mathrm{III}}) \right] \frac{\alpha_0 T_0^{-0.7}}{\Gamma} (1+z)^6 \quad (1.11)$$

The FGPA provides an analytic expression, calibrated against cosmological simulations, for the IGM opacity (Dijkstra M. 2019). In particular, the FGPA is useful if we can only use a dark matter-only simulation, which is common for surveys requiring large simulations, $\sim$ Gpc scales, that are too expensive to run when gas is included. However, in this project, we are modeling the proximity zones so we do not need such a large volume. In this case, we can run complete hydrodynamic simulations instead and calculate the optical depth directly from the gas properties.

1.4.2 The He II Lyα forest

The Lyα forest is a characteristic that can also be observed in the quasar spectra but at a different wavelength to hydrogen Lyα. Since the He II Lyα line falls blueward of 912 Å, this spectral region is susceptible to foreground continuum absorption from neutral hydrogen. As a result of this foreground absorption, the He II forest can only be observed at z > 2 since at lower redshifts it gets absorbed by the $\geq 10^{19}\mathrm{cm}^{-2}$ H I columns in our galaxy. The intervening systems with $N(HI) \geq 10^{17}\mathrm{cm}^{-2}$ also absorb part of the He II Lyα spectral region, thus, the quasar sightlines that happen to intersect fewer of these systems will have a more usable He II Lyα forest spectrum (McQuinn 2016). There are several features of the existing Lyα forest in He II that can be seen in the He II spectrum. In particular, it can be observed that at high redshifts, He II absorption is largely saturated. For example, in Shull et al. (2010a), they study the spectrum of the quasar HE2347-4342 at 2.7 < z < 2.9 which shows the largest Gunn-Peterson trough signature (no transmission region detected). This means that the He II is in a neutral state as the photons are completely absorbed, so the He II has not completely reionized in these regions. This fact can be used to constrain the end of the helium ionization epoch. Indeed, since these troughs are observed to occur at z $\geq$ 2.7, this redshift is often taken to mark the end of He II reionization.

1.4.3 Statistics of the Lyα forest

There has been much research performed that has shown that mocks extracted from simulations are able to describe the standard statistical set applied to the Lyα forest data, and some have even used this result to constrain cosmological parameters. Some of the most important Lyα forest statistics are *the line of sight (LOS) power spectrum*, *the probability distribution function of transmission (TPDF)*, *the line-width distribution* or *the H I Column Density Distribution* (McQuinn 2016). However, in this project, we will only focus on the evolution of the effective optical depth, since it is most relevant for the He II Lyα forest.

The simplest observable quantity is the mean transmission of the Lyα forest, defined as $\langle F \rangle = \langle \frac{I_{obs}}{I_{transm}} \rangle$, where I_{obs} and I_{transm} are the observed and transmitted intensity, respectively. It is usually measured over a fixed spatial scale, typically 50 comoving Mpc/h, and, often expressed as an effective optical depth (neglecting redshift-space distortions):

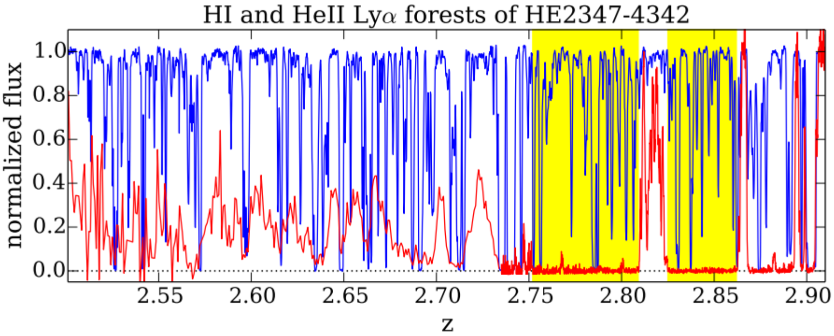

Figure 1.6: Spectra of the brightest quasar in the far UV, HE2347-4342 at z = 2.9. The blue and the red curve corresponds to the H I Lyα forest and the He II Lyα forest respectively. It can be observed that He II absorption is much stronger than H I absorption, where the highlighted areas in yellow represent the large GP trough in the He II Lyα forest at z $\geq$ 2.7. (McQuinn 2016; Fechner, C. & Reimers, D. 2007; Shull et al. 2010b)

$$\tau_{eff} = -ln\langle F\rangle = -ln\langle e^{-\tau}\rangle \tag{1.12}$$

The figure 1.7 shows a set of curves for $\tau_{\text{eff,HeII}}$ obtained varying $\frac{n_{\text{HeII}}}{n_{\text{HI}}}$ (Worseck et al. 2016). It can be seen, at z $<$ 2.6, the effective optical depth is low, i.e, there is a lot of transmitted flux in the He II Lyα forest so it must be highly ionized. At redshift z $\sim$ 2.7 - 3 some sightlines start to have higher optical depths, showing a large scatter between them as well so, in this case, there must be large variations in the He II fraction along different lines of sight. At z > 3 many of them show no transmitted flux at all, so there are only lower limits on the effective optical depth, but even at z = 3.4 some sightlines have a low optical depth, indicating that they are highly ionized. This seems to fit generally with the model represented by the blue line, which shows a specific He II reionization model.

1.4.4 The proximity effect

In quasar spectroscopy, the *proximity effect* refers to the relative absence of Lyα absorption near the ionizing source due to the enhanced photoionization rate caused by local radiation fields. At redshifts approaching the reionization epoch, it can be used to study the ionization level of the Universe and the environment and properties of QSOs. The way to detect this effect is both by looking along the line of sight of the quasar, i.e *proximity effect along the line of sight* and also by analyzing the effect produced in the Lyα forest of bright quasars by a foreground source located near to the quasar sightline, i.e *transverse proximity effect*, see figures 1.8 and 1.9. Therefore, this effect can be used to measure the background intensity: the more intense the background is, the smaller the proximity effect we expect at a fixed distance from the QSO since the QSO flux (known from its luminosity) is less important compared to the mean background.

However, this interpretation of the proximity effect to measure the ionizing background intensity is subject to several systematic uncertainties (Schirber et al. 2004). First, there may be

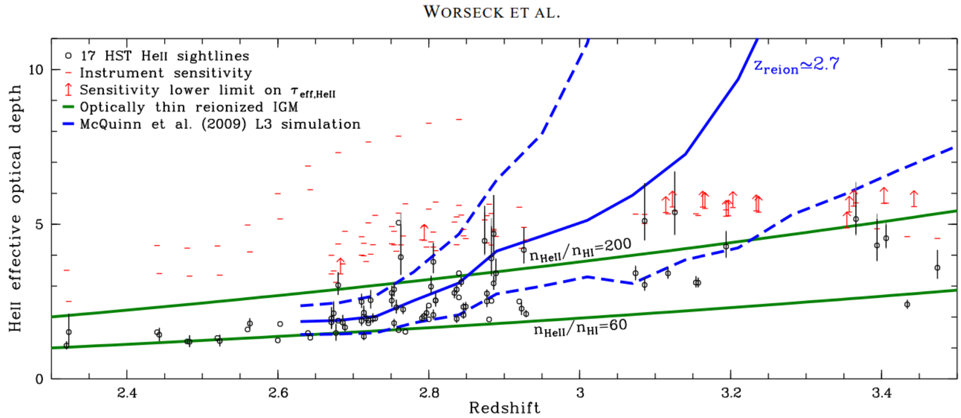

Figure 1.7: Example of the He II effective optical depth in function of redshift for 17 He II sightlines. The measured $\tau_{\mathrm{eff,HeII}}$ values are plotted as black circles with their corresponding statistical error bars and overplotted are the predictions from a model of a He II reionization matching low-redshift observations (Worseck et al. 2016).

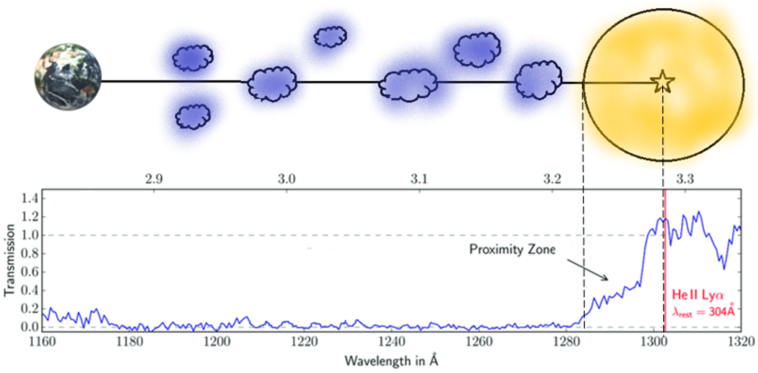

Figure 1.8: Sketch of the proximity zone of a QSO.

systematic errors in the redshift of the QSO estimated from its emission lines, which may impact the distances derived from the absorption systems to the QSO. Secondly, there is a possibility for QSO variability to occur on the photoionization time scale of 10^4 years and the proximity effect reflects the average brightness of QSOs on this time scale, so this brightness would be lower than the current brightness since QSOs are chosen in their bright phase in a limited flux sample. Additionally, some QSOs may be gravitationally lensed, again making them appear more luminous than they are. They are also likely associated with dense regions in the Universe, and the higher gas density in their vicinity may partially compensate for the decrease in the neutral fraction due to their ionizing flux. Some authors (Liske & Williger 2001; Fernandez-Soto et al. 1995; Møller & Kjaergaard 1992) have investigated the transverse proximity effect by taking some measure of the absorption in the region where the proximity effect should occur and comparing it to an

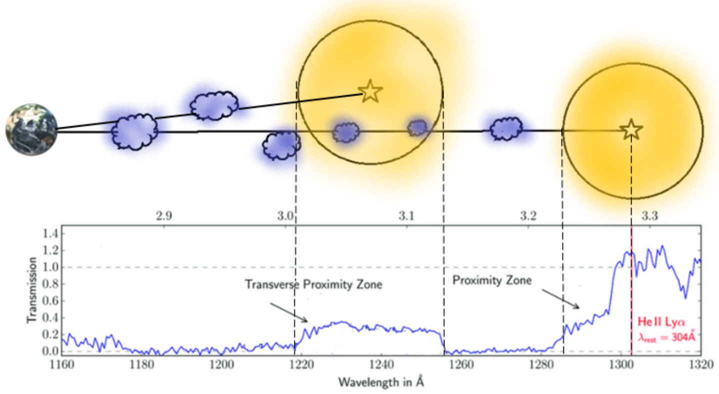

Figure 1.9: Sketch of the transverse proximity zone of a QSO.

empirical model of absorption systems derived from another QSO line of sight. In this case, a measure of the absorption is usually the number of Lyα lines with fitted Voigt profiles found per unit redshift. On the other hand, a different approach has been used in Møller & Kjaergaard (1992); Liske & Williger (2001), based on measuring the mean transmitted flux distribution in the proximity effect region and comparing it to an already modeled transmitted flux distribution, which is derived assuming that the Lyα forest is formed by uncorrelated absorption lines with a distribution of column densities and Doppler parameters obtained from fits to the observed spectra. So far this effect has been detected only for the He II Lyα forest and there is no evidence of its detection in the H I Lyα forest (Schirber et al. 2004).

Proximity zones have been studied both in observation and theory in the past two decades. However, with the limited spectral resolution, most studies have been focused only on measuring or modeling the ‘sizes’ of proximity zones. Observationally, the size of the quasar proximity zone is often defined as the distance from the quasar to the first point along the line of sight where the transmitted flux drops below 10% in a spectrum smoothed by a 20 Å boxcar (Fan et al. 2006). At $z > 3$ the intergalactic He II Lyα forest transmission on similar scales rarely exceeds this threshold (Worseck et al. 2019), so the He II proximity zones are well defined. On the other hand, at lower redshifts, the He II proximity zone sizes become less distinct due to the emergence of the post-reionization of the He II Lyα forest, although some radiative transfer simulations as the one used in Worseck et al. (2021) account for density fluctuations in a predominantly ionized IGM with an initial He II fraction as low as 1%, which is consistent with the inferences from the He II forest (Worseck et al. 2019). In a mostly neutral Universe, the thus defined proximity zone, in the beginning, is limited by the position of the quasar ionization front (I-front), which further depends on the quasar age and the neutral fraction of the abundances in the IGM (Fan et al. 2006). Therefore, these two important physical quantities can be constrained by measuring the proximity zone size distribution and evolution.

Up to this point, there are some differences in the evolution of the H I and He II proximity zone sizes. In general, after a quasar is turned on, the expansion of its ionization zones takes place in both H I and He II, and the former is believed to propagate faster as intergalactic hydrogen has been largely ionized at z = 3 - 4. However, it would take a significant amount of time, on the order of million years, for the light signal to travel over a distance of many Mpc (Zheng et al. 2019). For hydrogen, it is believed that hydrogen's propagation front expands at a nearly light speed due to the highly ionized surroundings (Bolton & Haehnelt 2007; Khrykin et al. 2016). As a result, young quasars at z $\sim$ 3 that display very small or null proximity zones in He II would show a full-sized H I proximity effect (Zheng et al. 2019). Given the flux of metagalactic UV background (UVB) radiation field $\Gamma_{\rm HI} = 10^{-12}\ {\rm s}^{-1}$ (Ryden 2003), the size of an H I proximity zone is around 10 Mpc at redshift z = 3 - 4 (Zheng et al. 2019). For luminous quasars, the size would be approximately 20 Mpc. On the other hand, for He II, the proximity zone sizes are sensitive to redshifts and less certain, although probably larger than their H I counterparts as He II ionizing UVB was developing rapidly (Zheng et al. 2019). Some models (Shull et al. 2010a; Zheng et al. 2015; Worseck et al. 2021), suggest that some of the quasars show quite small He II proximity zones, implying that they are likely young quasars that have not yet built significant high ionization zones in their vicinity. Specifically, in Worseck et al. (2021), they have used a sample of 17 quasars at 2.74 < z < 3.51 to measure the sizes of their highly ionized He II proximity zones.

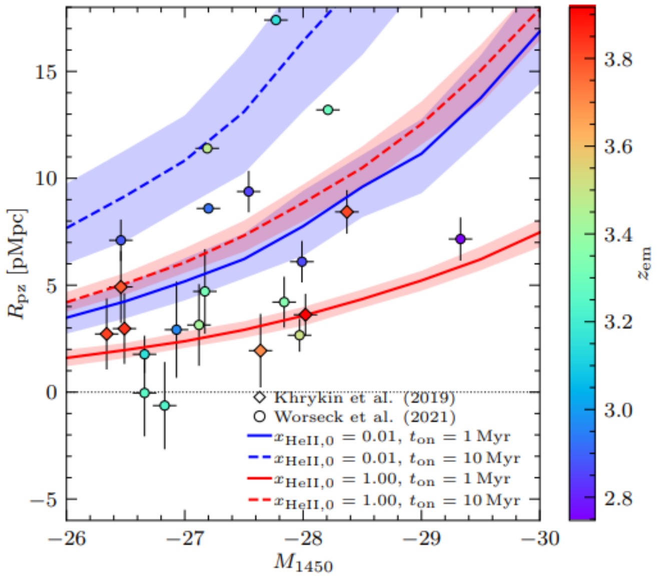

Figure 1.10: This figure shows the He II proximity zone size R_{pz} as a function of the quasar absolute magnitude M_{1450} for the 22 quasars in a sample analyzed by (Worseck et al. 2021).

In this work, they argued that the He II proximity zone sizes span a large range of sizes 2 pMpc < $R_{\rm pz}$ < 15 pMpc, and nine out of 17 presented $R_{\rm pz}$ > 5 pMpc, suggesting that large proximity zones are common (see figure 1.10). Additionally, in Chen & Gnedin (2021) using Cosmic Reionization On Computers (CROC) simulations, they analyzed extremely short proximity zone sizes of quasars with a magnitude of $M_{1450} = -26.66$ at z= 6.11. They found that around 1 - 2% of old quasars (30 Myr old) have extremely small proximity zone sizes (< 1 proper Mpc), of which the vast majority are due to the occurrence of a damped Lyα absorber (DLA) or Lyman limit systems (LLS) along the line of sight. These DLAs and LLSs are contaminated with metal, which offers a way to distinguish them from the normal proximity zones of young quasars. In some other works, they also study the evolution of the proximity zone sizes. For example, in Ryden (2003); Fan et al. (2006), they found a rapid growth of proximity zone sizes during redshifts z = 5.7 - 6.4. However, in Morey et al. (2021) an analysis of a sample of around 34 quasars at z = 5.77 - 6.54 was carried out, finding a slower growth of proximity zone sizes during the same redshift range, with the proximity zones sizes being $\sim$ 5 pMpc after a re-scaling all proximity zone sized to a fixed quasar magnitude of $M_{1450} = -27$.

Table 1.1: Sample of 24 quasars with He II proximity zones from Worseck et al. (2021). The name, magnitude, and the measured He II proximity zone sizes are listed below for an initial He II fraction of $0.01 \leq x_{\mathrm{HeII},0} \leq 1$. In this project, we have included proximity zones with negative values even though they have no physical meaning. They are the result of a large redshift uncertainties.

Quasar	**Magnitude**	**R_{pz} [Mpc]**
HE 2347-4342	-28.69± 0.1	-4.77±0.15
HE2QS J2149-0859	-26.83± 0.1	-0.63±2.04
HE2QS J1706+5904	-26.66± 0.1	-0.04±2.03
HE2QS J2354-2033	-26.88± 0.1	-3.65±1.68
SDSS J1237+0126	-26.66± 0.1	+1.77±0.87
SDSS J2346-0016	-27.97±0.1	+2.66±0.77
SDSS J0818+4908	-26.93±0.1	+2.92±2.25
HE2QS J0916+2408	-27.12± 0.1	+3.14±1.91
HS 0911+4809	-27.84 ±0.1	+4.21±1.19
HE2QS J0233-0149	-27.17±0.1	+4.71±1.98
Q 1602+576	-27.99±0.1	+6.1±0.97
PC 0058+0215	-26.46±0.1	+7.10±0.97
HS 1700+6416	-29.33±0.1	+7.16±1.01
SDSS J0936+2927	-27.20±0.1	+8.0±0.15
HS 1024+1849	-27.54±0.1	+9.38±0.97
SDSS J1253+6817	-27.19±0.1	+11.4±0.12
Q 0302-003	-28.21±0.1	+13.2±0.13
HE2QS J2157+2330	-27.77±0.1	+17.40±0.14
HE2QS J2311-1417	-27.64±0.1	+1.94±1.72
SDSS J1614+4859	-26.34 ±0.1	+2.72±1.66
SDSS J1711+6052	-26.49±0.1	+2.97±1.65
SDSS J1319+5202	-28.02±0.1	+3.62±0.98
SDSS J1137+6237	-26.46±0.1	+4.92±1.68
HE2QS J1630+0435	-28.37±0.1	+8.43±1.02

They also found very small sizes of proximity zones which are more likely because the quasars are extremely young ($t_Q < 10^5$ years). Table 1.1 and figure 1.11 show the data and the

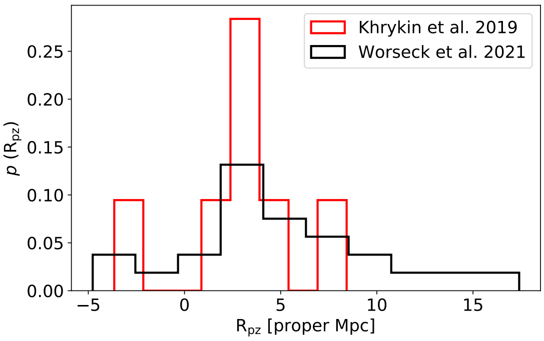

Figure 1.11: Probability density function (PDF) of the observed proximity zones from Worseck et al. (2021) and Khrykin et al. (2019).

probability density function (PDF) of the observed proximity zones from Worseck et al. (2021) and Khrykin et al. (2019). In the next sections, we will compare this data with our radiative transfer simulations.

1.4.5 The lifetime of quasars

A crucial factor in the research of the SMBH-galaxy co-evolution and the reionization history is *the quasar lifetime*, and related to it, *the duty cycle* (t_{dc}), defined as the fraction of time in which a galaxy hosts an active quasar. It is believed that these factors could shed light on the mechanism by which quasars are triggered (theorized to be either merger of galactic centers or secular disk instabilities), how gas is channeled to the center of the galaxy, and what are the properties of the inner accretion disk (Khrykin et al. 2016). Several methods have been used to constrain the t_{dc} but most of them seem to offer weak restrictions on this parameter. For example, the duty cycle of a population of objects has been inferred by comparing its number density and clustering strength but due to the uncertainties in the dark matter halo population of quasars, this method yielded a value of $t_{dc} \sim 10^6 - 10^9$ years (Conroy & White 2012; Adelberger & Steidel 2005).

Other models rely on comparing the time integral of the quasar luminosity function to the present-day number density of black holes but the uncertainty associated is the same order as the previous one. Even though these methods have been used to give a value of the $t_{\rm dc}$, they are not able to constrain the average quasar lifetime ($t_{\rm lt}$). For the latter, there have been methods presented that might determine this factor but the weak constraints obtained applies here as well. One of the methods is based on the H I *proximity effect*, corresponding to a change in the ionization state of H I in a quasar environment as measured by the H I Lyα forest. Based on the presence of a line-of-sight H I proximity effect at z $\sim$ 2 - 4 quasars, it would appear that they have been emitting continuously for a stable timescale, which corresponds to about 10^4 years in the IGM at z $\sim$ 2 - 4 (Khrykin et al. 2016). However, further research (Schawinski et al. 2010, 2015b), based on the photoionization of quasar host galaxies and light travel time arguments postulated a variability of the quasar lifetime to be on short 10^5 years (Ryden 2003).

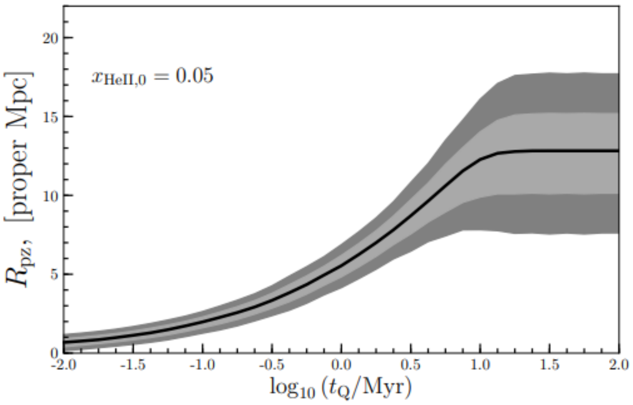

Figure 1.12: Figure showing the dependence of the He II proximity zone size $R_{\rm pz}$ on quasar lifetime $t_{\rm Q}$ from (Khrykin et al. 2019). The light and dark grey shaded areas represent 1σ and 2σ standard deviations of $R_{\rm pz}$, respectively, whereas the solid black line shows the median values.

As with the H I proximity effect, an analogous effect is observed in the He II Lyα forest. In this case, the He II proximity effect has been observed at $2.7 < z < 3.9$ where some well-studied samples (Shull et al. 2010a) have demonstrated the observed variance in the shape and sizes of the He II proximity zones. These methods constrain the t_{lt} to be from $\lesssim 1$ Myr to approximately 31 Myr (Hogan et al. 1997; Zheng et al. 2015). Nevertheless, the assumptions of a homogeneous IGM, which neglect the effect of a clumpy density field on the proximity zone with a He II fraction of unity, lead to only rough estimates of the quasar lifetime. In addition, constraints on the quasar lifetime have also been determined by the *transverse proximity effect*, e.g (Hennawi et al. 2006; Prochaska et al. 2013; Kirkman & Tytler 2008; Schmidt et al. 2018), an effect happening due to the enhancement of the UV radiation field around a foreground quasar which gives rise to increased IGM transmission in a background sightline. In general, the detection of this proximity effect is very challenging since there are several effects like an anisotropic quasar emission or overdensities around quasars which influences directly this measure. For the few quasars for which such detections have been possible, $t_Q = 10 - 30$ Myr has been calculated to provide a lower limit to quasar lifetime based on the transverse light crossing time between foreground and background (Khrykin et al. 2016). Furthermore, the sensitivity of individual He II proximity zones to the time-scale of prior quasar activity of up to 30 Myr offers a unique opportunity to constrain the underlying distribution of episodic quasar lifetimes (Khrykin et al. 2021), which can be compared to predictions from models of galaxy and black hole co-evolution (Worseck et al. 2021).

1.4.6 The growth of supermassive black holes (SMBHs)

A crucial and unanswered question in understanding black holes and galaxy evolution is how supermassive black holes form and grow during very early cosmic epochs. According to some observations (Wu et al. 2015; Bañados et al. 2017; Bañados et al. 2018; Greig et al. 2019) high

Method	Net/Episodic	Lifetime [yr]
Current:		
Evolution	Net	$< 10^9$
Local black holes	Net	$10^7 - 10^8$
Merger scenario	Net	few $\times 10^7$
Mergers & starbursts	Episodic	few $\times 10^8$
Proximity effect	Episodic	$> 10^8$
Radio Jets	Episodic	few $\times 10^8$
Future:		
QSOs at z >6	Episodic	few $\times 10^7$?
Transverse proximity effect	Episodic	10^7?
Clustering	Net	$10^6 - 10^7$?

Table 1.2: Constraints on the QSO lifetime taken from Martini (2003)

redshift quasars (z $\geq$ 6) are found to host SMBHs with masses between $10^9 - 10^{10}$M$_\odot$. The redshifts at which these quasars have been found correspond to less than 1 Gyr after the Big Bang, which raises many questions about how these black holes can grow so drastically in such a short cosmic time. A very massive initial seed along with a continuous accretion at the maximum theoretical rate, also called Eddington luminosity, throughout the whole age of the Universe has been proposed as a way to explain the formation of these SMBH masses (Volonteri 2012; Haiman et al. 2013). In addition, these considerations also indicate that the lifetime of quasars, i.e, the amount of time spent actively accreting matter onto the central SMBH, is on par with Hubble time, which is around 10^9 years at z $\sim$ 6.

Different scenarios have been proposed regarding what might provide the initial seed for the SMBHs to form. The first scenario is related to massive stars. When a massive star runs out of fuel at the last stage of its life, it cannot support itself any longer against its gravity and its core collapses to become a black hole. Thus, a black hole is defined as the result of a massive star collapsing under its gravitational force. This might be a reason for believing that the first generation of massive stars, known as Population III stars, might provide the seeds for the SMBHs within quasars (Volonteri 2010). The masses of these initial seeds are expected to be $M_{\text{seed}} = 100$M$_\odot$ (Valiante et al. 2016), however, as previously said, it would be needed an accretion at the Eddington limit for the entire age of the Universe for the black hole mass to grow up to 10^9M$_\odot$ by z = 6. Even so, radiative feedback is likely to prevent sustained Eddington accretion over such an extended period (Alvarez et al. 2009; Milosavljević et al. 2009). A possible solution to this problem is that SMBH seeds are formed by other means, for instance, through the direct collapse of dense gas in gaseous and metal-free proto-galaxies (since enriched halos would cool efficiently, favoring fragmentation and, thus, star formation) (Lodato & Natarajan 2006; Visbal et al. 2014). The direct collapse of massive gas clouds will produce massive initial black hole seeds of the order of $M_{\text{seed}} = 10^4 - 10^6M_\odot$ in the early Universe, which could explain their very early presence (Visbal et al. 2014). Furthermore, as these black hole seeds have a larger mass than those predicted with the Pop III remnants, the tension between z = 6 quasar formation time and cosmic age is reduced. Black holes in this scenario, however, must still accrete gas over a significant amount of the available time (Tanaka 2014; Visbal et al. 2014). Additionally, simulations in recent years have also revealed that direct collapse black holes are very difficult to achieve (Regan et al. 2014). Another formation scenario has also been proposed, which is based on stellar-dynamical processes. Rather than forming a direct collapse black hole, the collapsing gas is likely to form stars since high redshift dark matter halos are likely already enriched with at least trace amounts of metals (Omukai et al. 2008). Very compact nuclear star clusters may form as a result of these early star formation episodes, where stellar collisions within the cluster can lead to the formation of massive stars as remnants with masses between $M_{\text{seed}} = 10^2 - 10^4 \text{M}_\odot$ (Omukai et al. 2008). Although for now, these scenarios are only theoretical models under study, they might provide some insight into the formation of SMBHs.

As has been discussed in the previous section 1.4.5, identifying the characteristic timescales that govern quasar activity is crucial to understanding the growth of SMBHs. In recent works (Eilers et al. 2017; Worseck et al. 2021; Satyavolu et al. 2022), measures of proximity zone sizes have been used to constrain quasar lifetimes. The solution to the time evolution of the He III ionization front, R_{IF}, can reveal the connection between the quasar lifetime and the proximity zone size (Bolton & Haehnelt 2006; Khrykin et al. 2016),

$$R_{IF} = R_S \left[1 - \exp\left(-\frac{t_Q}{x_{\text{HeII}} t_{\text{rec}}} \right) \right]^{\frac{1}{3}} \tag{1.13}$$

where $t_{rec} = \frac{1}{n_e \alpha_A}$ is the recombination timescale and R_S is the classical Strömgren radius, given by $R_S = \left(\frac{Q_{4\text{Ry}}}{4\pi \alpha_A n_{\text{HeIII}} n_{\text{e}}} \right)$, which is the radius of the sphere in which ionization is exactly balanced by recombination around a source of radiation. In this equation, $Q_{4\text{Ry}}$ is the rate at which He II ionizing photons are emitted by the quasar. This definition of the proximity zone using the evolution of the I-front is closely related to that described in section 1.4.4 although, in this description, some effects are not taken into account, e.g, the overlapping ionized He III regions or large-scale structure effects. As well exemplified in Khrykin et al. (2016), the ionization front R_{IF} seems to be located much further from the quasar (at around 64 cMpc in the example given in Khrykin et al. (2016)) even though the He II transmission saturates before (at 50 cMpc in the example given in Khrykin et al. (2016)).

Furthermore, another important time parameter to take into account when constraining the quasar lifetime and understanding the growth of SMBHs is the Salpeter timescale (Salpeter 1964), given by:

$$t_{\text{S}} = 4.5 \times 10^7 \left(\frac{\epsilon}{0.1} \right) \left(\frac{L}{L_{Edd}} \right) yrs \tag{1.14}$$

where L_{Edd} is the Eddington luminosity, i.e, the maximum luminosity at which the environment of a black hole can shine and still accrete matter, and ϵ corresponds to the efficiency of mass-to-energy conversion. The astrophysical standard assumption for this factor is $\epsilon = 0.1$. With this value for the efficiency and with a maximum luminosity of $L = L_{Edd}$, the Salpeter timescale is $t_S = 44$ Myrs (Salpeter 1964), i.e., the limit imposed by the Eddington luminosity, which implies a black hole will not grow beyond an e-factor in that time frame. The dependency of the Salpeter timescale on the growth of the SMBH is given by:

$$M_{\rm BH} \propto M_{\rm seed} \exp\left(\frac{t}{t_S}\right) \tag{1.15}$$

For instance, the observed small H I proximity zone sizes in Eilers et al. (2017, 2020) which constrains the lifetime of quasars around 10^4 years might be difficult to explain the SMBH formation models. As seen previously, the Salpeter timescale of a black hole growing exponentially at the Eddington limit with a radiative efficiency of 0.1 is $t_S = 44$ Myrs, so a quasar lifetime of 10^4 years would correspond to $\sim 0.005 t_{\rm S}$, then the black hole hardly grows. Nevertheless, as previously seen, direct estimates of the quasar activity can be inferred from the proximity zones of He II quasars at z = 3 - 4, since the long equilibration timescale $t_{\rm eq} \sim 30$ Myrs (Khrykin et al. 2016) is comparable with Salpeter's timescale. However, as published in the same study, the inferred results on the quasar lifetime from their observed proximity zones were around 1 Myr, still not sufficient to prove the formation of the early back holes.

1.4.7 Variability of quasars

Many studies have been conducted in the last decades (Khrykin et al. 2016; Eilers et al. 2017; Khrykin et al. 2019; Eilers et al. 2018, 2020; Worseck et al. 2021), which have used proximity zones to constrain quasar lifetimes. For instance, in Eilers et al. (2017) they analyzed the H I proximity effect in the spectra of 34 quasars at z > 6 and found very small H I proximity zones, implying lifetimes of $t_{\rm Q} \lesssim 0.1$ Myr, with one particular quasar shining for only $t_{\rm Q} \lesssim 0.01$ Myr (Eilers et al. 2018). Moreover, in Khrykin et al. (2019), they measured the He II proximity zone sizes in the spectra of six z ~ 4 quasars, suggesting a lifetime of around 1 Myr. These such short quasar timescales that have been found are, however, very problematic when comparing them with the constraints coming from quasar clustering and current theories about how SMBHs grow (see Table 1.2). If one assumes the light bulb model for the quasar light curves, i.e, a constant luminosity throughout time, then under this assumption the lifetime $t_{\rm Q}$ and the duty cycle t_{dc} are equivalent, and thus they measure the duty cycle as well. However, it appears that the results of Eilers et al. (2017, 2020); Khrykin et al. (2016); Khrykin et al. (2019); Worseck et al. (2021) do not seem to match the high values of t_{dc} implied by the strong clustering quasars at z $\simeq$ 4 measured in Shen et al. (2007); White et al. (2008). Indeed, with the short inferred lifetimes and the assumption of a simple light curve, it would be impossible to grow $10^9 {\rm M}_\odot$ black holes in these quasar hosts.

An alternative approach to resolve this problem has been proposed, which uses the flickering light curve model rather than the light bulb model (Ciotti & Ostriker 2001; Schawinski et al. 2015a; King & Nixon 2015; Satyavolu et al. 2022). In this picture, the ultraviolet continuum emission from the quasar fluctuates as a result of either intrinsic changes in the accretion flow, or time variable obscuration along our line of sight. Thus, the accretion onto SMBHs can be episodic. This variability is quantified using duty cycles and episodic times, being the latter the duration of each luminous episode (Davies et al. 2019). In Worseck et al. (2021), they inferred short episodic times of $\lesssim 1$ Myr for four of the 13 quasars they studied at redshifts ~ 3 from He II proximity zones. Additionally, the authors argue that most black hole growth must have occurred during the obscured period in high-redshift quasars. Furthermore, a similar analytical model is presented by the authors in Davies et al. (2019) that study proximity zone sizes for both blinking light curves and more general light curves and is in good agreement with their simulations. According to the authors, the distribution of proximity zone sizes in such scenarios allows to constrain the episodic lifetime and duty cycle of quasars, disfavoring large variations in quasar luminosity below $< 10^4$ years. This project focuses primarily on variability, so we will explore it in more depth in our results section.

CHAPTER 2

SIMULATIONS AND CODES

Throughout this section, it will be explained how the project has been developed until now, as well as a brief overview of the 1D cosmological radiative transfer that has been used.

2.1 Cosmological hydrodynamical simulations

As has been mentioned in the section 1.4.1, cosmological simulations are indeed fundamental for using the Lyα forest as a tool to obtain the physical properties of the IGM. Many studies have developed very sophisticated computer codes to carry out cosmological simulations but the basic idea always remains the same. The first step is assuming a cosmological model which is specified by the set of cosmological parameters such as H_0, $\Omega_{m,0}$, $\Omega_{b,0}$, $\Omega_{k,0}$, $\Omega_{\Lambda,0}$, and σ_8. The second step is to adopt a primordial spectrum of density fluctuations, which is well determined by CMB observations. Then, we start at the high-z with a set of particles that are evenly distributed as the gravitational potential is taken as uniform, over a grid on a comoving volume and after that, disturb these particles away from this uniform distribution according to a random realization of the primordial fluctuations. The gaseous nature of the IGM requires simulating hydrodynamics along with the gravitating dark matter particles to obtain accurate results. The N-body code integrates the equations of forward motion: particle distribution $\Rightarrow$ gravitational potential; potential gradients $\Rightarrow$ particle accelerations; particle accelerations $\Rightarrow$ particle velocities; particle velocities $\Rightarrow$ particle positions and, additionally, this is coupled with a full hydrodynamics description which accounts for the particle flow and the phenomena related to gas dynamics. This process is repeated, moving forward in time at specific intervals where non-linear gravitational evolution transforms the initial fluctuations into a network of voids and tunnels with intermixed sheets and filaments. Introducing a background of ionizing radiation, e.g. from QSOs and star-forming galaxies, will produce the desired Lyα forest (Vogelsberger et al. 2019).

Specifically in this project, we have been working with lines of sight extracted from a 160 Mpc/h box through massive halos in a large cosmological simulation from the *Sherwood simu-*

lation suite from (Bolton et al. 2016). It was run with a modified version of the parallel Tree-PM smoothing-hydrodynamic particle (SPH) code P-GADGET-3, an updated and extended version of GADGET-2 (Springel 2005). These are some of the largest hydrodynamical simulations of the Lyα forest performed to date, made in volumes $10^3 - 160^3 \mathrm{Mpc}^3/\mathrm{h}^3$ and span almost four orders of magnitude in mass resolution with up to 17.2 billion particles. They employ a variety of physics variations including warm dark matter and galactic outflows (Bolton et al. 2016). The models use the fit ΛCDM cosmological parameters (Planck et al. 2014), where Ω_m = 0.308, Ω_Λ = 0.692, h = 0.678, Ω_b = 0.0482, σ_8 = 0.829 and n = 0.961, with a primordial helium fraction by mass of Y_p = 0.24. The simulations do not include metal line cooling since it is expected to have very little effect on the Lyα forest transmission as the metallicity of the low-density IGM is very low. The photo-ionization and photo-heating of the hydrogen and helium gas are calculated using the spatially uniform ionizing background model (Haardt & Madau 2012). In this model, the gas is assumed to be optically thin and in ionization equilibrium, which is expected to be a very good approximation (except in highly overdense regions) for the post-reionization IGM at z < 5, when hydrogen is highly ionized and the mean free path for ionizing photons is much larger than the typical separation of ionizing source (Worseck et al. 2014). All parameters used, such as ionization fractions, recombination rates, He I dialectical recombination rates, collisional excitation cooling rates, Bremsstrahlung cooling rate, and Compton reverse cooling rate have been taken from different works, well explained in Bolton et al. (2016). Furthermore, star formation is not followed in most of these simulations, the gas particles with temperature T < 10^5 K an overdensity Δ > 1000 become collisionless particles (Viel et al. 2004), which results in an important increase in computing speed at the expense of eliminating cold and dense gas model. This choice has a minimal effect on low column density absorption systems probed by the forest of Lyα (Bolton et al. 2016). They do, however, perform some simulations with the star formation and energy-driven outflow model of Puchwein & Springel (2012) to investigate this. On the other hand, the simulations in this work do not include feedback from active galactic nuclei (AGN), although they have performed one low-resolution run with the AGN feedback model described also in Puchwein & Springel (2012), for examining the Lyα forest at z < 2 since it is expected that AGN feedback impact on Lyα forest transmission statistics at z = 2.25, but has a smaller effect on the Lyα forest at higher redshift (Viel et al. 2013).

2.2 1D radiative transfer algorithm

To model the extent of the cosmological regions H II and He II around high redshift quasars and, at the same time, to trace local changes in the ionization state and gas temperature due to ionizing radiation, a complete treatment of the radiative transfer by hydrogen and helium IGM is required. As already mentioned, in the second part of the project we used the 1D radiative transfer algorithm based on Bolton & Haehnelt (2007). It is not the purpose of this report to be so detailed about it, as everything is well explained in the mentioned paper, but some features of this algorithm will be given.

First, in this code, they include the simplification of ignoring the hydrodynamics of radiation, since luminous quasar fronts are highly supersonic and therefore unaffected by the hydrodynamics of the gas over the short time scales considered here. In addition, photons are conserved regardless of spatial resolution which allows great freedom in the size of the grid cells and the time step. The cosmological model adopted here is a flat Universe dominated by a cosmological constant and non-relativistic matter. Related to the ionizing radiation field, we just have a single source of radiation, the quasar, which follows a power-law spectrum. The source is placed at the beginning of each sightline and traces the change in the ionization state and temperature of the IGM for a specific finite time as the radiation is propagated. In this case, we are considering the case of a single source of radiation namely the quasar which is the only one to properly provide the photons to ionize He III zones. However, that would work for early times, but not for later when there have been formed more sources that can also release He II ionizing photons. Thus, there is included an extra contribution to the ionization rate from a UV background. Taking a uniformly discretized space grid with elements of specific size along the line of sight to the source at a given timestep, assuming a constant luminosity, and taking into account this contribution, the ionization rate per unit volume for H and He was calculated.

Similarly, the photo-heating rate per unit volume for species i has been inferred which in turn includes an optically thin photo-heating rate due to the UV background. The transmission of photons in this code is considered to happen instantaneously avoiding imposing extra limitations or violating photon conservation. The ionization state and the temperature of the hydrogen and helium are computed by solving a set of four coupled first-order ordinary differential equations where the first three determine the abundances of the ionized species. This equation depends on the number of densities of the species, the photo-ionization rates, the collisional ionization rates, the total radiative recombination coefficient, and the helium mass fraction. The fourth differential equation is used to compute the temperature which includes the contribution to cooling by the adiabatic expansion of the Universe.

The algorithm solves the equations using the first-order implicit integration scheme which provides a good balance between accuracy and speed. To solve these equations accurately, a timestep comparable to the hydrogen ionization timescale is adopted which might be too small close to a luminous source. In those cases when the time interval is smaller than the main timestep used to track the position of the I-front, the code sub-cycles over each main time step using smaller time intervals based on the ionization timescale to solve for the ionic abundances. When the rate of change in the electron number density is less than a specific value, the code switches to solve the ionic abundances assuming an ionization equilibrium of the gas. In this situation, only the temperature equation is integrated, allowing much larger time steps to be taken which improves the calculation time. Regarding the cross-sections and rates adopted in this radiative transfer scheme, they follow a model, which includes specific values for the ionizing photon production rate of the source, the spectral index, the hydrogen number density, the mass fraction of helium, and the age of the source, that has been carefully chosen by taking into account that any gas seen in the Lyα absorption lies behind the source I-fronts and is thus optically thin. All the cross-section coefficients, photo-ionization rates, cooling functions, and some other parameters are described in Bolton & Haehnelt (2007).

2.3 Optical depth calculations

As mentioned briefly in the introduction, the main aim of this thesis is to model the proximity zones around quasars at redshift z = 3 and, in order to do so, this project has been divided into different parts. In the first part, the goal was to use some data from the hydrodynamical simulation to make mock observations of the quasar absorption lines, calculating the optical depth and the flux based on Lukić et al. (2014). We intended to get a first contact with the QSO spectrum, as well as get to know the IGM itself by studying, for example, how the temperature or the abundance of neutral hydrogen changes along the different lines of sight and how these quantities depend on each other. To this end, it has been provided 100 sightlines extracted from hydrodynamical simulations at redshift z = 3 including information about the position of the pixel along the line of sight in kpc, the total and neutral hydrogen density for each pixel in cm^{-3}, the temperature in Kelvin, and the peculiar gas velocity in each pixel in $\mathrm{km/s}$. First, the process was carried out for hydrogen, and later we adopted the routine for helium as well.

The cross-section for a resonant line scattering is given by:

$$\sigma_{\upsilon} = \frac{e^2\pi}{m_{\mathrm{e}}c} f_{\mathrm{lu}} \frac{1}{\Delta\nu_{\mathrm{D}}} \phi_{\nu} \tag{2.1}$$

where $e = 4.8 \times 10^{-10}$ $\mathrm{cm}^{\frac{3}{2}}$ $\mathrm{g}^{\frac{1}{2}}$ s^{-1} is the electric charge, $f_{\mathrm{lu}} = 0.416$ is the oscillator strength with the same value for H and He, $m_{\mathrm{e}} = 9.1 \times 10^{-28}$ g the electron mass, $c = 2.99 \times 10^{10}\ \mathrm{cm\,s}^{-1}$ the speed of light, $\Delta\nu_{\mathrm{D}}$ the Doppler width, and ϕ_{ν} is the line profile. At the same time, the Doppler width $\Delta\upsilon_{\mathrm{D}}$ is related to the Doppler parameter b (associated to the velocity broadening scale) as $\Delta\nu_{\mathrm{D}} = \frac{b}{c\nu_0}$ with ν_0 being the line center frequency. Likewise, the Doppler parameter b is associated with the temperature as $b = \sqrt{\frac{2k_{\mathrm{b}}T}{m_{\mathrm{H/He}}}}$ if no extra kinematic components are assumed, where $k_{\mathrm{b}} = 1.38 \times 10^{-16} \mathrm{g}(\frac{\mathrm{cm}}{\mathrm{s}})^2 \mathrm{K}^{-1}$ is the Boltzmann constant and $m_{\mathrm{H/He}}$ corresponds to the mass of the hydrogen or helium atom, respectively. For the hydrogen atom $m_{\mathrm{H}} \sim m_{\mathrm{proton}} = 1.67 \times 10^{-24}$ g and for the helium atom $m_{\mathrm{He}} \sim 4m_{\mathrm{proton}} = 6.64 \times 10^{-24}$ g.

On the other hand, the line profile is given by a Doppler profile which follows a gaussian distribution as:

$$\phi_{\upsilon} = \frac{1}{\pi^{\frac{1}{2}}} exp(-x)^2 \tag{2.2}$$

where $x = (\nu - \nu_0)/\Delta\nu_D$ is the shift from line center. In this way, we obtain:

$$\phi_{\upsilon} = \frac{1}{\pi^{\frac{1}{2}}} exp\left(-\frac{(\nu - \nu_0)^2}{\Delta\nu_{\mathrm{D}}^2}\right) \tag{2.3}$$

It must be noticed that, in general, the line profile is given by the Voigt profile but for temperatures and densities typical in the IGM, the difference in optical depth computed with a Voigt vs Doppler profile is very small (McQuinn 2016). Furthermore, in this case, it is convenient to consider absorption or emission lines not as a function of frequency, but as a function of Doppler velocity relative to some reference frame. Combining the previous equations, the optical depth at a fixed redshift in terms of the velocity is given by:

$$\tau_\upsilon = \frac{e^2 \pi f_{lu} \lambda_0}{m_e c H} \int n_H \frac{1}{\pi^{\frac{1}{2}} b} exp \left(- \frac{(\upsilon - \upsilon_0)}{b} \right)^2 d\upsilon \tag{2.4}$$

where λ_0 corresponds to the rest wavelength of the Lyα transition for H and He respectively. For hydrogen, it has a value of $\lambda_0 = 1215$ Å and for helium $\lambda_0 = 303.7$ Å, υ is the Hubble flow velocity, and H is the Hubble expansion rate at a specific redshift.

In figure 2.1 we can see a representation of the overdensity, the neutral hydrogen fraction, the optical depth, and the flux along one sightline. In the upper panel, the black line with left y-axes shows the overdensity, i.e, the total gas density divided by the mean density, and the blue line with right y-axes shows the neutral hydrogen fraction.

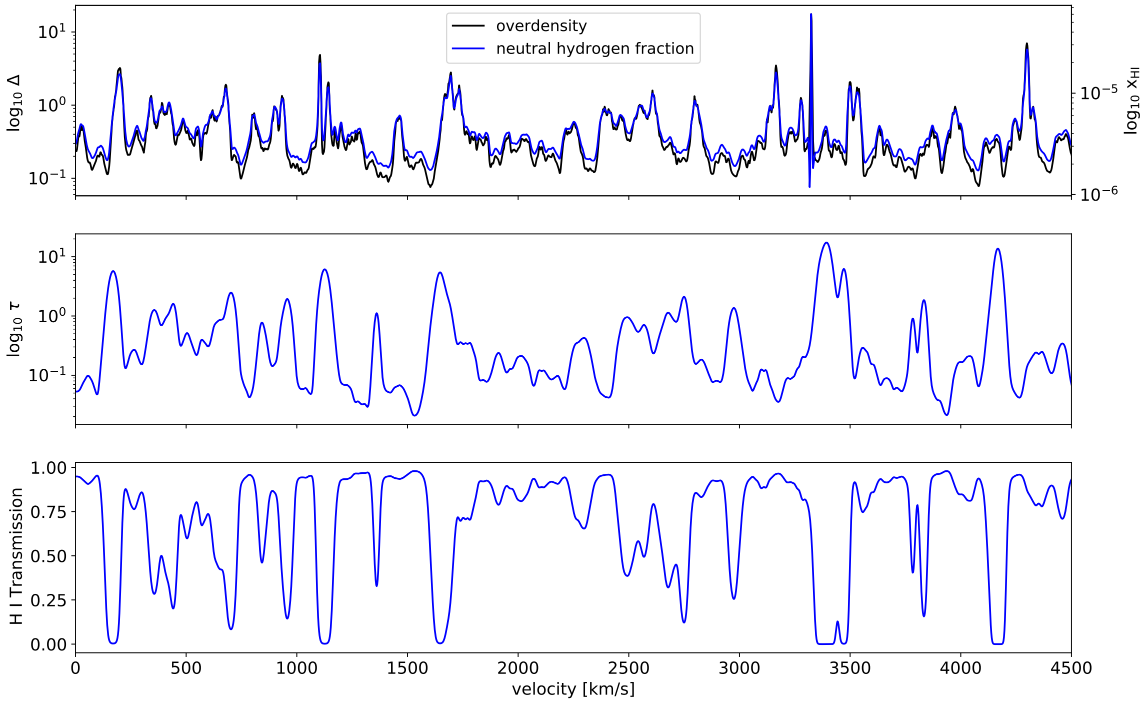

Figure 2.1: Representation of optical depth and flux along the line of sight. The line of sight was obtained by cosmological simulations in the first part of this project.

It can be seen that at redshift z = 3, all the hydrogen is highly ionized, with values of H

I fraction oscillating between $10^{-6} \leq x_{HI} \leq 10^{-4}$. High overdensity regions, i.e. $\Delta = 5 - 10$, are usually partially ionized due to their high density and therefore more shielding and recombination. At high-density peaks, x_{HI} becomes more neutral and traces the density of the gas. The optical depth and flux are shown in the second and third panels. In regions where the optical depth is high, the flux vanishes because those regions are less ionized, so the photons are more likely to be absorbed on their way to us, and therefore the flux we receive is almost zero. On the other hand, those areas where the optical depth is low are highly ionized and photons can escape more easily from possible absorption, resulting in a non-zero flux. Overall, we can see that for a gas with slightly higher overdensities, the optical depth would be greater, therefore, more Lyα forest absorption and less flux received. The optical depth calculations were tested against a pre-existing code, verifying that everything was working properly.

CHAPTER 3

MODELLING PROXIMITY ZONES IN THE LIGHTBULB MODEL

As part of this section, we will first present the results of our radiative transfer code and briefly discuss the properties of the gas, and then introduce the concept of proximity zone and study their dependence on quasar lifetime, He II ionizing background, quasar luminosity, and density fields. Throughout this section, we will use the lightbulb model, which assumes a constant quasar light curve.

3.1 Results of the radiative transfer code

As discussed previously in section 2.2, we have used the 1D radiative transfer algorithm described on Bolton & Haehnelt (2007). First, the code was configured to run in a field of uniform density with the initial ionization state and temperature set by hand. However, as seen in the reionization section (see section 1.3.1), due to the inhomogeneity of the reionization process of H and He, the IGM is not homogeneous, so it is expected to have a contribution from the massive halos along the lines of sight. Consequently, 100 new sightlines passing through massive haloes, which are believed to be the hosts of quasars at redshift 3.2, were provided to run the radiative transfer code on them. We could also manually change some of the most important parameters to simulate different IGM scenarios. A variety of initial hydrogen and helium reionization states were studied as well, starting with high fractions He II and H I, moving to a fully ionized state with high fractions He III and H II, and finally reaching an intermediate state where hydrogen was fully ionized and helium slightly ionized. Since in our particular case we are interested in measuring the proximity zone of the He III front, we set a fully ionized H I and almost complete ionized He II, playing with the He III fraction value, since some observations of the effective optical depth of He II at z $\sim$ 3.2 show that helium may be highly doubly ionized. In addition, by modifying the parameter that measures the number of photons received by the quasar and its lifetime, it was possible to check how the luminosity of the quasar affects the absorption spectra. The dependency of the He II fraction with the initial ionization background and the quasar lifetime are shown in figures 3.1 and 3.2, respectively. Figure 3.1 shows the evolution of the He II fraction along a sightline with different He II initial ionization states, namely, $x_{\mathrm{HeII},0} \in \{0.99, 0.44, 0.01\}$ and $x_{\mathrm{HeIII},0} \in \{0.01, 0.55, 0.99\}$ for $t_Q = 45$ Myrs.

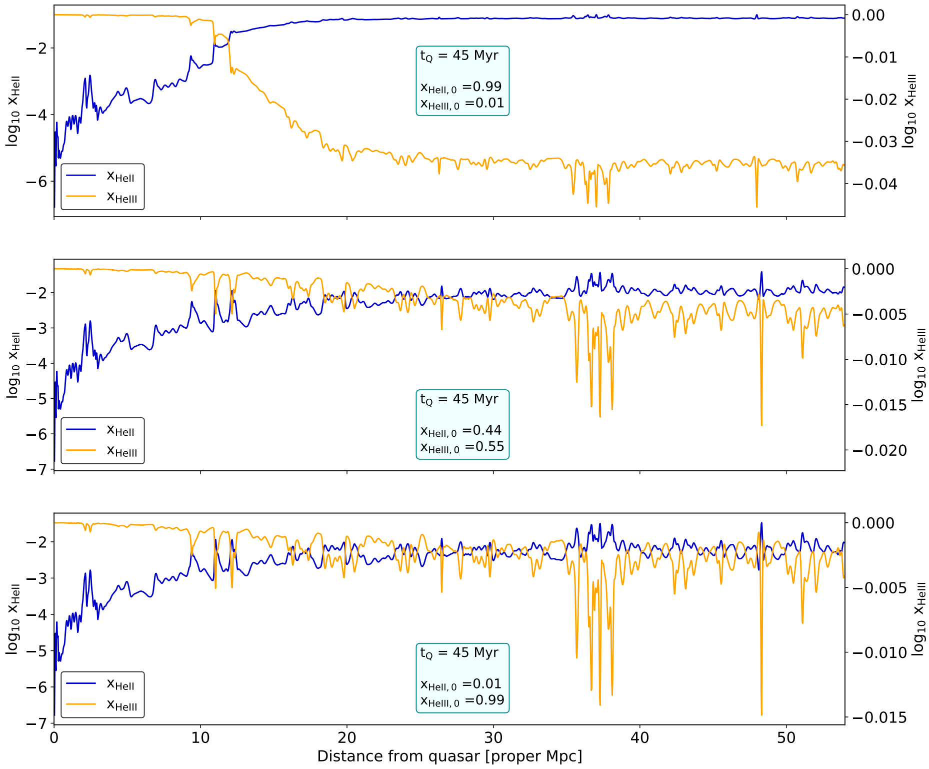

Figure 3.1: Illustration of the evolution of He II and He III fractions along one sightline with different ionization backgrounds.

In the first panel of the figure 3.1, the initial He II background is almost completely ionized. In the second panel, the initial He II conditions correspond to a half-ionized background and in the last panel, the background presents a very high He II fraction. Since the quasar is assumed to be at the origin, we can see that in all cases, we find small amounts of He II ($10^{-6} \leq x_{\mathrm{HeII}} \leq 10^{-4}$) and large amounts of He III ($x_{\mathrm{HeIII}} \sim 1$) near the source, since high-energy photons will ionize the medium around the sources first. On their way far from the quasar and depending on the ionization background, the He II and He III fractions will evolve differently, but eventually return to their initial background state, as can be seen in all the cases.

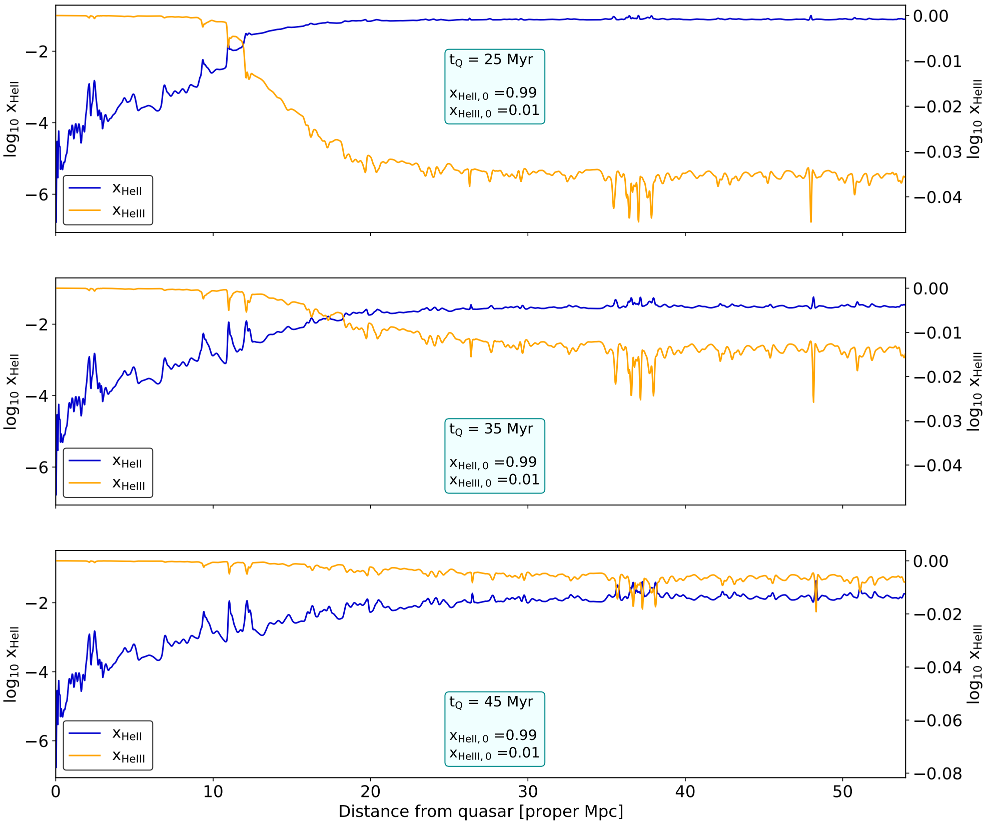

Figure 3.2: Illustration of the dependence of He II and He III fractions along a sightline for different quasar lifetimes.

Figure 3.2 shows the evolution of the He II and He III fractions along a sightline for different quasar lifetimes, namely, $\mathrm{t_Q} \in \{25, 35, 45\}$ Myrs and same initial background state $\mathrm{x_{HeII,0}} = 0.99$ and $\mathrm{x_{HeIII,0}} = 0.01$. According to this figure, the longer the quasar has been shining, the longer it will take for He II and He III to return to their initial ionization states. This is visible in the He III fraction, which shifts from a very dramatic drop in the first panel (shorter quasar lifetime) to a smoother change in the third panel (longer quasar lifetime). In all cases, at large radii, the gas is in form of He II and, at short radii, the gas is in the form of He III, since the He II fraction is fully ionized ($\mathrm{x_{HeII}} \leq 10^{-3}$) due to the proximity to the source.

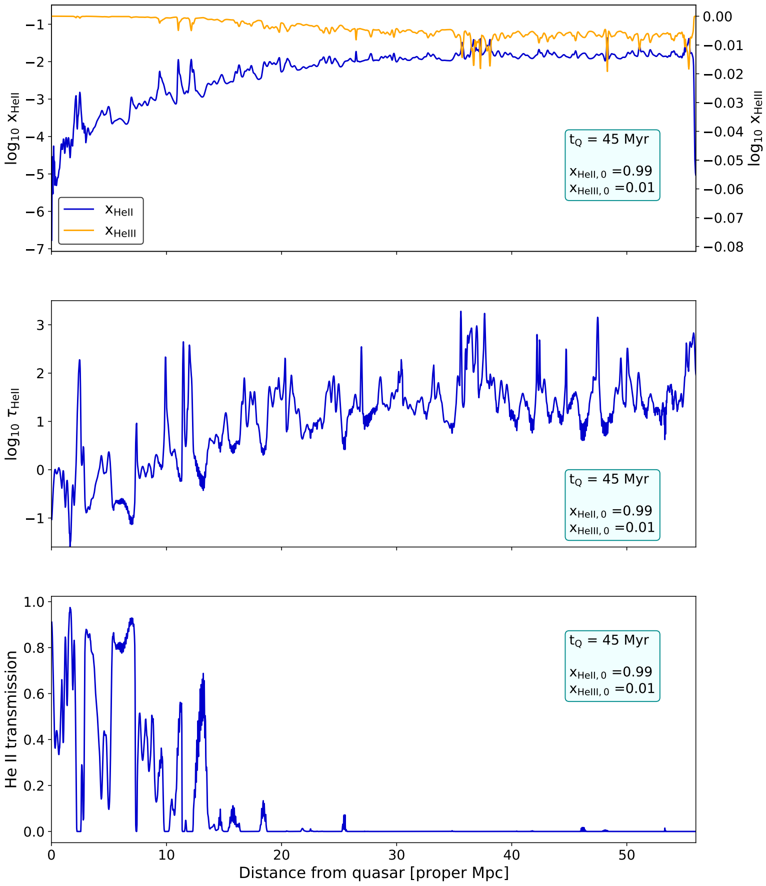

Figure 3.3: Representation of the He II / He III fractions, He II optical depth and He II flux as a function of distance in Mpc for a quasar lifetime of 45 Myrs and an initial ionization background of $x_{\mathrm{HeII,0}} = 0.99$ and $x_{\mathrm{HeIII,0}} = 0.01$ along one line of sight.

Since we are interested in analyzing the He II proximity zones, the He II optical depth calculations as well as the He II fluxes have been implemented. This is shown in the figure 3.3 for a quasar lifetime of 45 Myrs and an initial ionization background of $x_{\mathrm{HeII,0}} = 0.99$ and $x_{\mathrm{HeIII,0}} = 0.01$. The second and third panels display a large He II optical depth and the He II transmission, respectively. The proximity zone signature can be appreciated in the He II transmission (third panel) as an increase in flux at small radii arising from the high quasar ionization rate. At large radii we can see a long Gunn Peterson (GP) through, often observed in the spectra of quasars at redshift around 3.2 (Worseck et al. 2021), where the He II flux decays to almost zero. This is a direct consequence of the large optical depth of He II seen in the second panel, which depends on the choice of the initial ionization background.

3.2 Proximity zone sizes and the lightbulb model

We calculated the size of the proximity zones of a quasar using the method described in Worseck et al. (2021). In general, the size of the proximity zone will depend on the lifetime of the quasar, the ionizing background of He II (the initial fraction of He II), the luminosity of the quasar, and the density fields.

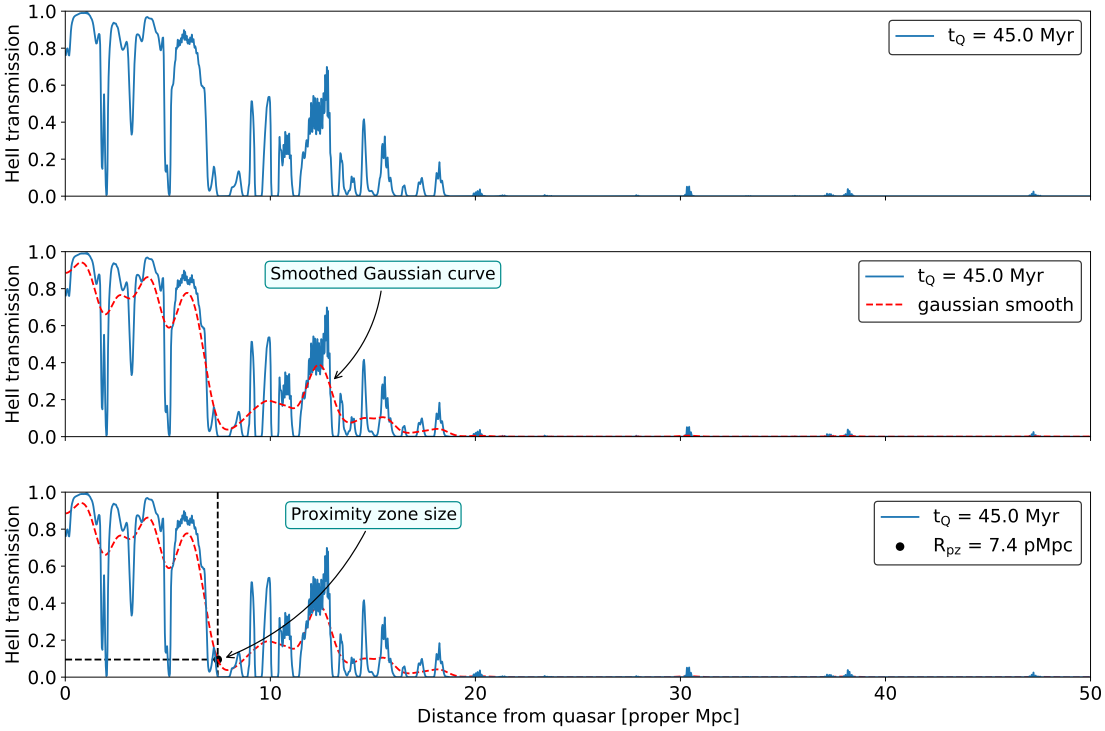

Figure 3.4: First panel: He II transmission. The second panel: smoothed Gaussian spectrum in dashed red line with a FWHM of 1 pMpc. Third panel: representation of the proximity zone size at the point where the smoothed spectrum drops below 10 %.

The luminosity generally is determined by observations but since we are only simulating, we can play with this variable. In this paper, they use a Gaussian filter with a full-width-half-maximum (FWHM) of 1 proper Mpc to smooth the spectra. The size of the proximity zone is therefore the distance between the quasar and the point where the smoothed spectrum first drops below 10 % (see figure 3.4). In order to implement this in the code, we need to specify sigma σ, which coincides with the number of pixels in the array corresponding to the standard deviation of the Gaussian. The FWHM and sigma are related by FWHM = $2.355\sigma^2$. Once this was implemented, different proximity zones could be measured for different lines of sight by changing the parameters of the initial ionization, the quasar lifetime, and the luminosity.

3.2.1 Variation of the proximity zone with the ionizing background

An example of how the proximity zone changes with the ionizing background is given in figure 3.5. As can be seen from the figure, the variation barely changes from a very ionized background where the fraction of He II is $x_{\mathrm{HeII},0} = 0.01$ in the first panel to a background state with

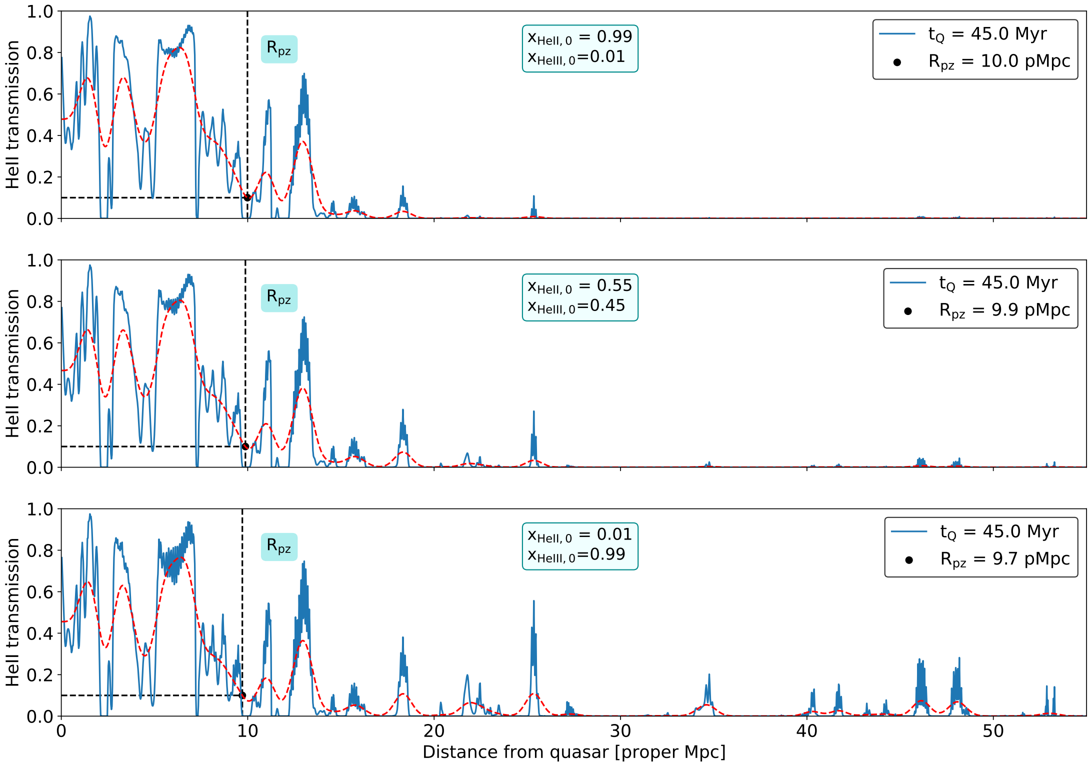

Figure 3.5: This figure shows the variation of the proximity zone sizes with the UVB with a luminosity of $L = 1.195 \times 10^{47}$erg s^{-1}

$x_{\mathrm{HeII},0} = 0.99$ in the second panel which, at the same time, shows a slightly larger $\mathrm{R_{pz}}$. A half-ionized initial background example is also given in the third panel.

---

[2] https://en.wikipedia.org/wiki/Full_width_at_half_maximum#cite_note-1

Additionally, the transmission profiles (the blue curves) exhibit more transmission at larger distances from the quasar for lower values of He II and higher values of He III. This is expected since the shape of the transmission profile depends on both the initial He II fraction (which is set by the ionizing background) and the amount of photoelectronic heating of the IGM (which results from the ionization of the He II), also known as the "thermal proximity effect" (see section 1.4.4). Thus, in those models with low $x_{\mathrm{HeII,0}}$, the increase in the transmission at larger radii is due to a higher He III background as compared to models with $x_{\mathrm{HeII,0}} > 0.50$ (second and third panel of the figure 3.5).

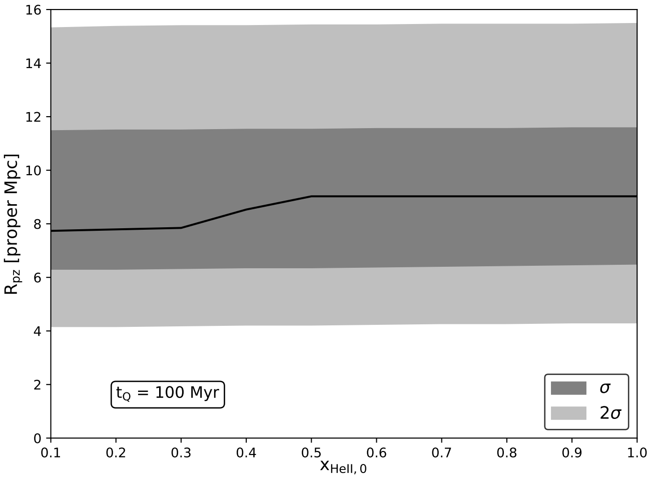

Figure 3.6: He II proximity zone sizes as a function of the He II fraction $x_{HeII,0}$ at fixed $t_Q = 100$ Myr. The black line shows the median values of the R_{pz} and the dark and light grey shaded areas correspond to 1σ and 2σ standard deviations of the R_{pz}, respectively.

Furthermore, for small distances (closer to the quasar), the photoionization rate from the quasar $\Gamma^{\mathrm{QSO}}_{\mathrm{HeII}}$ dominates the total photoionization, impacting the proximity zone size more than the He II background ionization state. On the other hand, at larger distances (far away from the quasar), the He II background photoionization rate $\Gamma^{\mathrm{bkg}}_{\mathrm{HeII}}$ dominates and so the effect of the He II ionization background is more prominent. We might notice, however, that if we recall the definition of the proximity zone as the distance between the quasar and the point at which smoothed transmission first drops below 10 percent (see section 3.2), this definition only takes into account the effects of photoionization generated by the quasar $\Gamma^{\mathrm{QSO}}_{\mathrm{HeII}}$. This can be seen by looking at the transmission at larger radii where $\Gamma^{\mathrm{bkg}}_{\mathrm{HeII}}$ dominates. The transmission due to He II ionization background rarely exceeds the 10 percent threshold, concluding that this threshold is too big to include any effect coming from it.

To sum up, the dependency of the proximity zone with the ionizing background involves some interesting effects. First, an increase in the transmission due to the thermal proximity effect, which becomes stronger the more He II is present in the IGM. Second, an increase in the transmission due to a high initial fraction of He III and a small initial fraction of He II, and third, the 10 percent threshold is too high to include effects of the $\Gamma_{\rm HeII}^{\rm bkg}$. For a more comprehensive picture of this dependency, we extended the study by using all the sightlines through the simulation and post-processing with our 1D radiative transfer code. Figure 3.6 illustrates the variation of all the He II proximity zone sizes as a function of the He II fraction at a fixed quasar lifetime of 100 Myrs. Based on this figure, we can conclude that the proximity zone size is not strongly dependent on the initial ionizing background when the quasar lifetime is long enough.

3.2.2 Variation of the proximity zone with the quasar lifetime

The proximity zone depends on how long the quasar has been shining. The figure 3.7 illustrates how the size of the proximity zone changes with different quasar lifetimes, namely, $\rm t_Q \in \{10, 30, 100\}$ Myrs along one sightline.

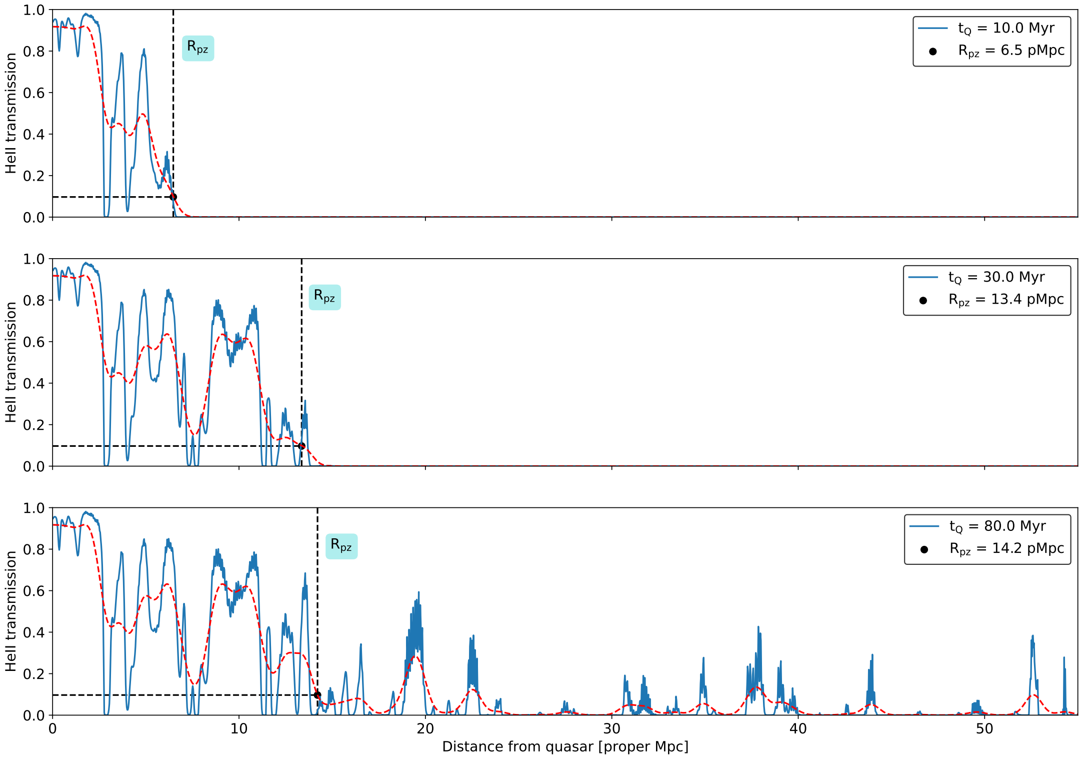

Figure 3.7: This figure shows the variation of the proximity zone sizes with the quasar lifetime with a luminosity of $\rm L = 1.19 \times 10^{47} erg\ s^{-1}$

The reason for the dependency of the proximity zone size on the quasar lifetime is based on the response of the IGM to changes in the radiation field. The sizes of the proximity zones gradually increase during short quasar lifetimes due to a change in the ionization of the radiation field until it reaches an equilibrium value given by $\mathrm{t_{eq}} = \frac{1}{\Gamma^{\mathrm{HeII}}_{\mathrm{bkg}}} \approx 30$ Myrs for He II at redshifts $z \approx 3 - 4$ (Khrykin et al. 2016). Afterwards, the proximity zone is insensitive to the lifetime. This would explain why the choice of the quasar lifetimes in figure 3.7 are not randomly chosen. There are, indeed, differences in $\mathrm{R_{pz}}$ before reaching equilibrium, illustrated in the first and second panels for a $\mathrm{t_Q}$ of 10 and 30 Myrs, respectively. However, in the second and the third panel, the latter with $\mathrm{t_Q}$=100 Myr, the difference in the $\mathrm{R_{pz}}$ barely changes, since right after 30 Myr the size does not depend on $\mathrm{t_Q}$ anymore.

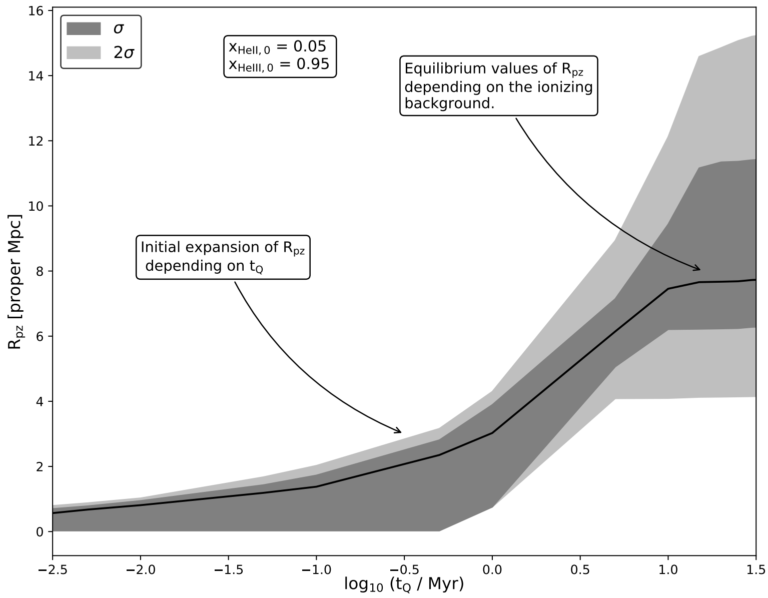

Figure 3.8: Representation of the He II proximity zone sizes $\mathrm{R_{pz}}$ as a function of the quasar lifetime $\mathrm{t_Q}$ with a fixed $\mathrm{x_{HeII,0}} = 0.05$ and $\mathrm{x_{HeIII,0}} = 0.95$. The black line shows the median values of the $\mathrm{R_{pz}}$ and the dark and light grey shaded areas correspond to 1σ and 2σ standard deviations of the $\mathrm{R_{pz}}$, respectively.

Expanding the study to all the sightlines as in the previous case, we were able to obtain all proximity zone sizes for different values of the quasar lifetime. Thus, a plot similar to that above (see figure 1.12) was created, as shown in figure 3.8 where the shaded contours refer to 1-2σ respectively. In this figure, we can clearly see the dependency of the $\mathrm{R_{pz}}$ on $\mathrm{t_Q}$ as well as the equilibrium value reached around 30 Myrs. In practice, the comparison of this figure with observations might give a constraint on how long an individual object has been shining for (Eilers et al. 2018; Khrykin et al. 2019).

3.2.3 Variation of the proximity zone with the luminosity

This scenario is illustrated in figure 3.9. In this plot, one can see the impact of the photon production rate on the structure of the proximity zone size. All panels show the transmission along one sightline with a fixed quasar lifetime of $t_Q = 40$ Myrs, a very ionized initial background ($x_{HeIII,0} = 0.99$), and, a luminosity of $L \in \{4.75 \times 10^{46}, 3 \times 10^{47}, 1.89 \times 10^{48}\}$ erg s^{-1}.

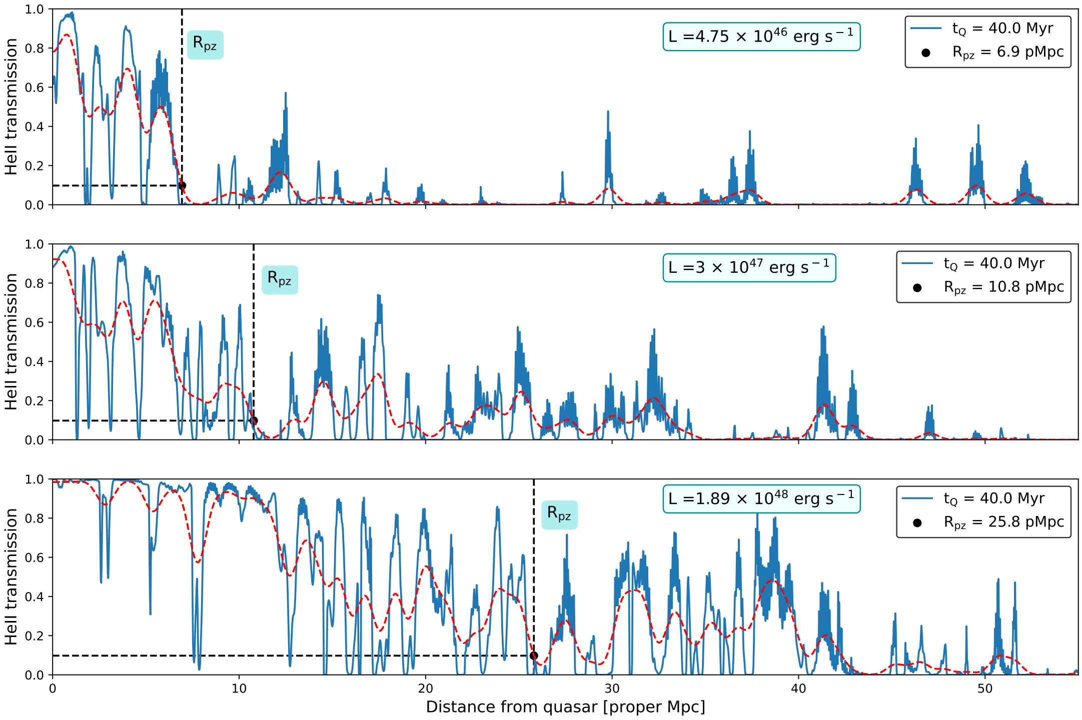

Figure 3.9: This figure shows the variation of the proximity zone size with the luminosity. The blue lines correspond to a quasar lifetime of 40 Myr.

One can see two interesting effects. First, as expected, brighter quasars present a higher photon production rate, increasing the ionization rate, which in turn expands the proximity zone. Second, the overall transmission profile drops sharply below the 10% threshold when we decrease the photon production rate, i.e, toward lower luminosities, as comparing the first and third panels. Additionally, this dependency can be explained in terms of the equilibrium timescale. As seen previously, before reaching the equilibrium value, at lower distances from the quasar, the proximity zone has a dependency on the quasar's lifetime. It turns out that the equilibration distance, R_{eq}, scales with the photon production rate Q_γ, as $R_{eq} \propto Q_\gamma^{\frac{1}{2}}$ (Khrykin 2016). This way, an increase in the photon production rate results in a larger size of the proximity zone.

Further exploration of this dependency has included the reproduction of a similar figure to the one shown in Worseck et al. (2021) (see figure 3.10), using our radiative transfer simulations at redshift 3.2 over all the sightlines. The figure shows the average $\mathrm{R_{pz}(M_{1450})}$ for different models varying He II fractions $\mathrm{x_{HeII,0}} \in \{0.01, 1\}$ and quasar lifetimes $\mathrm{t_Q} \in \{1, 10\}$ Myr. For each model, the shaded regions correspond to the 16-84th percentile scatter. Additionally, some data observations were also included, namely, a sample of 24 proximity zones between -28.69 $\leq \mathrm{M_{1450}} \leq$ -26.34 from Worseck et al. (2021) and another sample of 7 quasars between -28.37 $\leq \mathrm{M_{1450}} \leq$ -26.46 from Khrykin et al. (2019), all with their respective systematic errors. The observed data are shown in table 1.1 and its distribution is represented in figure 1.11.

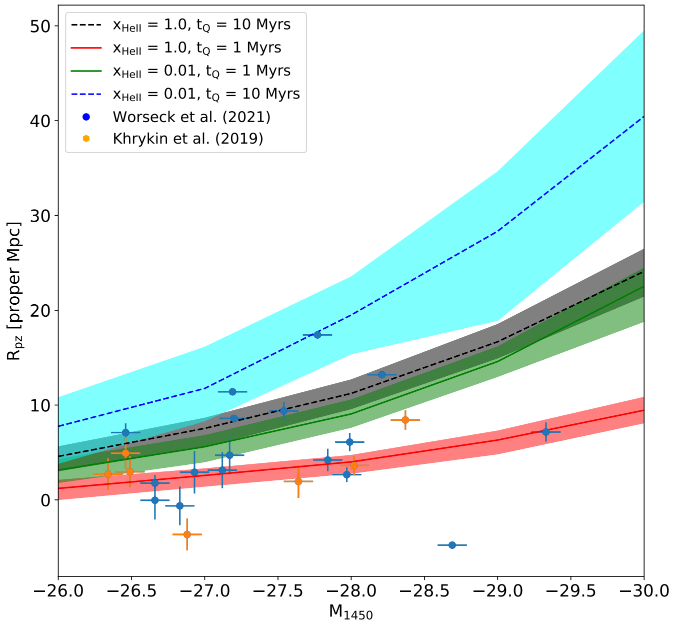

Figure 3.10: Representation of the He II proximity zone sizes $\mathrm{R_{pz}}$ as a function of the absolute magnitude $\mathrm{M_{1450}}$. The colored lines represent the average of $\mathrm{R_{pz}}$ including its 16-84th percentile scatter from the radiative transfer simulation at $z = 3.2$ for different initial He II fractions and quasar lifetimes. Some dataset observations are overplotted: the blue data points are taken from Worseck et al. (2021) and the yellow data points are from Khrykin et al. (2019) (see Table 1.1). Both with their respective errors.

While both of these previous works (Khrykin et al. 2019; Worseck et al. 2021) perform proximity zone calculations, they both use the data derived from Worseck et al. (2019). As shown in the plot, for some observed proximity zones there exists a small correlation with the simulated data, specifically with $\mathrm{t_Q} = 1$ Myr and $\mathrm{x_{HeII,0}} = 1.0$ model. However, those that present small proximity sizes cannot be simulated by any of the cosmological models discussed.

Based on this finding, we might think that the assumption we made (see section 2.2) that the quasar turns on once and has constant luminosity (lightbulb model) might not be true. Quasars may instead experience periods of low and high accretion rates (Davies et al. 2019), also known as the "flickering model". In the following sections, we will explore this effect in more detail.

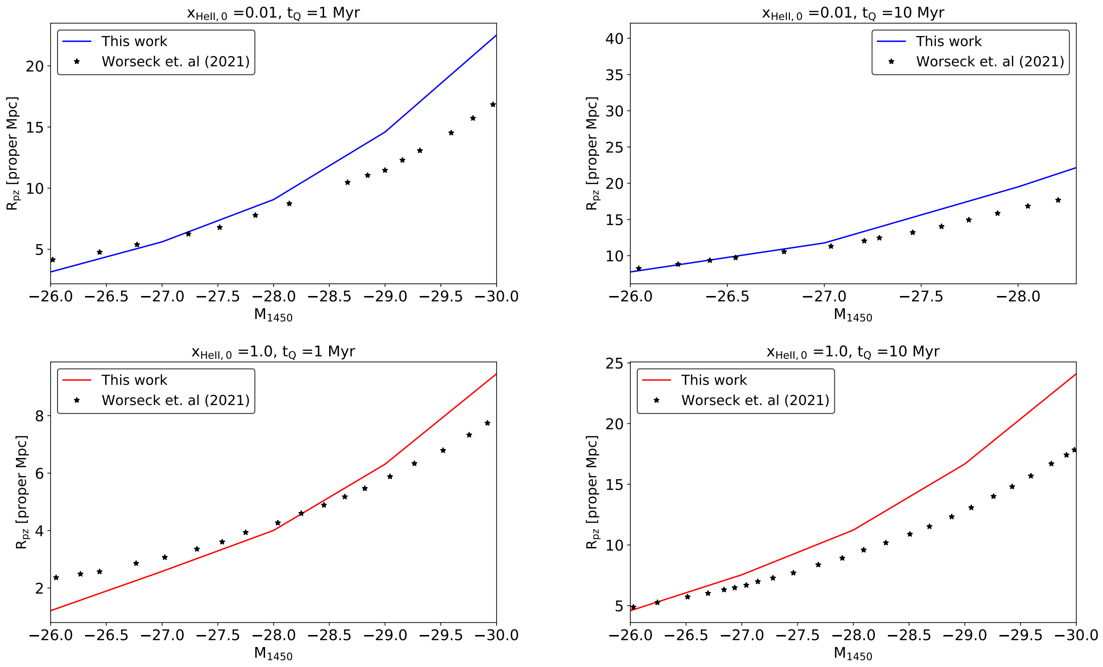

Figure 3.11: Comparison of the proximity zone sizes $R_{\rm pz}$ as a function of magnitude M_{1450} between our RT code and that used in Worseck et al. (2021) for each model. The first upper panel corresponds to an initial He II fraction of $x_{\rm HeII,0} = 0.01$ and quasar lifetimes of 1 and 10 Myrs. The bottom panel shows the models where the initial He II fraction is $x_{\rm HeII,0} = 1.0$ for quasar lifetimes of 1 and 10 Myrs, respectively.

A comparative analysis of the RT results used in this study with other approaches carried out in this field may be of interest. This reason motivated the figure 3.11 that compares our results with those reported in Worseck et al. (2021). The authors also used a combination of hydrodynamical simulations and one-dimensional radiative transfer of He II quasar proximity zones, described in Khrykin et al. (2016), to explain the diversity in the sizes of the proximity zones and to infer quasar on-times. This was accomplished by processing the skewers with a 1D radiative transfer algorithm based on C^2-Ray code (Mellema et al. 2006). As illustrated in figure 3.11, we compare each model from our work and theirs one by one. Overall, the agreement is not bad, considering the different hydrodynamic simulations being processed, the different radiative transfer codes employed, and the different methods used for setting the initial ionization state of the gas. In our case, we have used an average value for the ionization state everywhere, while the results in Worseck et al. (2021) include an inhomogeneous initial ionization background.

3.2.4 Distribution of the proximity zone sizes

As we may have noticed in the figures 3.6, 3.8, 3.10 from this work and figure 1.12 from Khrykin et al. (2016), when we use all the sightlines from the simulations and run our 1D radiative transfer code on them we obtain a broad distribution of the R_{pz}, i.e, for the same quasar lifetime, that is,

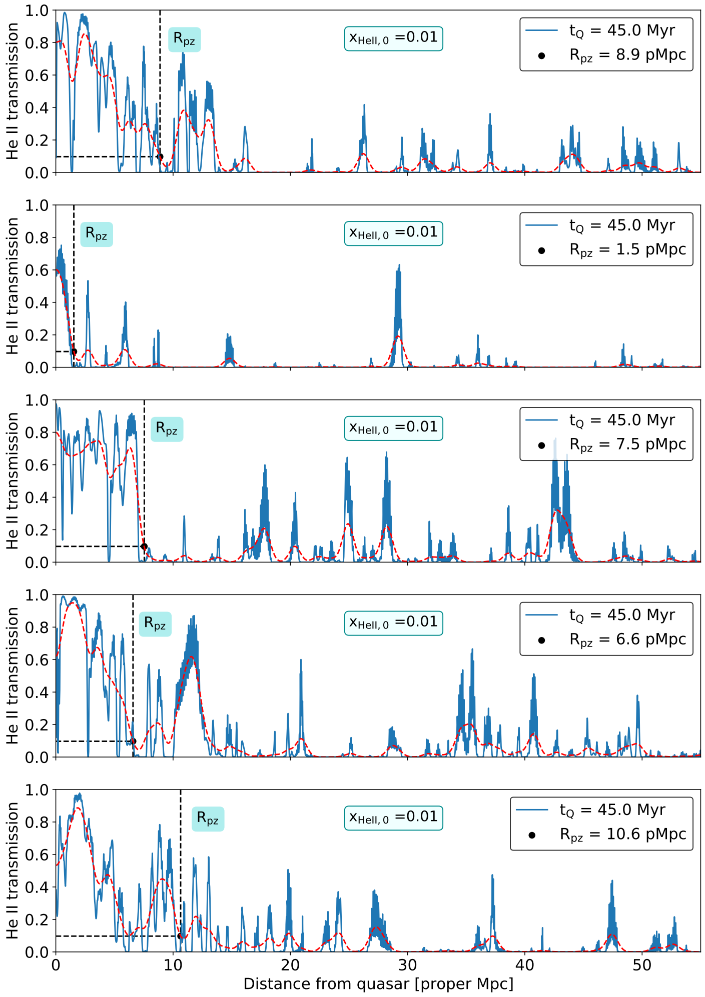

Figure 3.12: Representation of the change in the He II transmission for five different sightlines with the same parameter model. An initial He II ionization fraction of $x_{\mathrm{HeII},0} = 0.01$ and a quasar lifetime of $t_Q = 45$ Myr were chosen. The change in the He II transmission is due to the density fluctuations in the IGM.

for the same quasar lifetime or He II fraction, the size of the proximity zone fluctuates between specific values. Hence, we may have oversimplified our previous assumptions about He II fractions, lifetimes, and luminosities. Actually, not only will the He II background fluctuate from one line of sight to another but also the quasar will have a distribution of the lifetimes. This fact is clearly represented in figure 3.12, where we set the same model parameters for different sightlines. The reason behind the variability in the transmission of different sightlines is the density fluctuations. As the density fluctuates in the IGM around quasars, R_{pz} varies significantly, complicating the constraint of parameters in the vicinity of quasars. Moreover, the uncertainty associated with the quasar redshift also adds significant scatter.

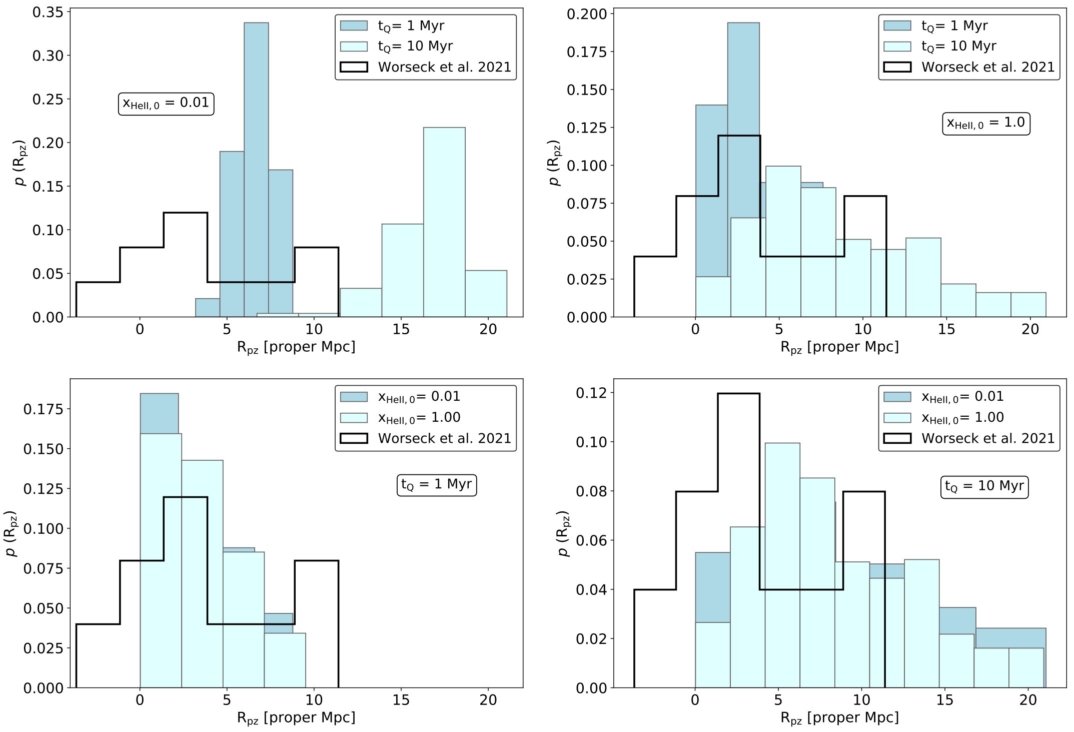

Figure 3.13: Probability density function (PDF) of the proximity zones in our radiative transfer simulations for different quasar lifetimes and He II fractions. The upper left panel shows the PDF for $x_{HeII,0} = 0.01$ and the upper right panel for $x_{HeII,0} = 1.0$. Blue and cyan-shaded histograms in both figures correspond to 1 Myr and 10 Myr, respectively. Similarly, the lower left panel shows the PDF for $t_Q = 1$ Myr and the lower right panel for $t_Q = 10$ Myr. Blue and cyan-shaded histograms in both figures correspond to $x_{HeII,0} = 0.01$ and $x_{HeII,0} = 1.0$, respectively. In black is the observed probability function of the proximity zone sizes with a magnitude of $-26.50 \leq M_{1450} \leq -27.50$ from Worseck et al. (2021), (see table 1.1).

For example, in Khrykin et al. (2019), the largest redshift errors produce an uncertainty of

$\sigma(\mathrm{R_{pz}}) = 1.7$ Mpc, similar to the smallest proximity zone measurements. Thus, a comparison between observations and radiative transfer models might be helpful to constrain the lifetime of a quasar.

For a more detailed analysis, the figure below illustrates the probability density function (PDF) of the observed proximity zone from Worseck et al. (2021) along with the predicted PDFs from our radiative transfer simulations. In this figure, only the observational data with magnitudes between $-26.50 \leq M_{1450} \leq -27.50$ from the table 1.1 was included. The upper left panel of the figure 3.13 shows the distribution for $\mathrm{x_{HeII,0}} = 0.01$ and different quasar lifetimes $\mathrm{t_Q} \in \{1, 10\}$ Myrs, and in the upper right panel we can see the distribution of $\mathrm{R_{pz}}$ for the same values of $\mathrm{t_Q}$ but $\mathrm{x_{HeII,0}} = 1.0$ instead. Similarly, the lower left panel shows the PDF fixed to $\mathrm{t_Q} = 1$ Myr, and the lower right panel illustrates the PDF fixed to a quasar lifetime of $\mathrm{t_Q} = 1$ Myr, both of them for He II fractions of $\mathrm{x_{HeII,0}} \in \{0.01, 1.00\}$. As we can see, the PDF distribution plot reveals interesting information. The upper panels suggest that $\mathrm{t_Q} = 1$ Myr and $\mathrm{x_{HeII,0}} = 1.0$ appears to be the most preferred model by the observed data. In the bottom panels, we can see an overlap between the histograms for different values of $\mathrm{x_{HeII,0}}$, which is a direct result of the weak dependence of the proximity zone sizes with the initial He II fraction (see subsection 3.2.1). Furthermore, according to Khrykin et al. (2019), this sensitivity and redshift uncertainties make inferring He II fraction information very difficult.

3.3 Summary

In this chapter, we described how to model the proximity zone sizes using the lightbulb approach. The results of our radiative transfer simulations were first presented, which include the evolution of the overdensity, temperature, and H II and He II fractions along a sightline. From these results, we acquired a wealth of information regarding the gas properties of IGM. Additionally, we studied proximity zones in depth, studying how they are affected by background ionizing radiation, quasar lifetime, luminosity, and density fields. Our results indicate that proximity zones are barely affected by the ionization background but are dependent on the quasar lifetime (until the equilibration timescale is reached), luminosity, and density field. Comparing our RT models with observations, we found that a quasar lifetime of 1 Myr best explained the observed data. However, for this quasar lifetime, the black hole barely has time to grow into a supermassive black hole.

CHAPTER 4

MODELLING PROXIMITY ZONES IN THE VARIABLE MODEL

The analysis from the previous section led us to conclude that none of the models we discussed can simulate the small proximity sizes observed in Worseck et al. (2021). Possibly that is because we assumed the quasar would turn on once and have a constant luminosity. In this section, our approach will change and we will consider that the luminosity may vary during low and high quasar accretion rates.

So far, all the analyses carried out in this project have assumed that the quasar has a constant luminosity over time. This approach is called the “lightbulb model”. However, according to some observations (Martini & Schneider 2003; Rumbaugh et al. 2018; Schawinski et al. 2015a) quasars do not behave like constant “lightbulbs” but are instead likely to undergo periods of low and high accretion rates, also called “flickering quasar model”. In the flickering quasar model, the variability in the quasar’s light curves may vary because of intrinsic variations in accretion rates or variable obscuration by clouds in the broad line region (BLR) as they pass through our line of sight (Rumbaugh et al. 2018). In fact, they may vary by 10% - 30%, corresponding to ~ 0.1 mag to ~ 0.3 mag, over approximately 15 years, as shown in Rumbaugh et al. (2018). The relevant timescale associated with changes in the accretion rate is the viscous timescale (in a weak magnetic field, the matter in the accretion disc rotates non-rigidly, causing magneto-rotational instability, which in turn leads to turbulence that contributes to viscosity), which is typically on the order of 10^5 years (Schawinski et al. 2015a; King & Nixon 2015). Generally, the IGM is capable of probing quasar variability on timescales comparable to the equilibration time of the gas, i.e. $t_{\rm eq} \approx \Gamma_{\rm HeII}^{-1} = 10^6$ years due to finite response time to the radiation of the quasar. As shown in Davies et al. (2019) for hydrogen, the proximity zones in the presence of a flickering quasar with uniform background radiation are sensitive to the episodic lifetime and duty cycle. An illustration of these parameters is shown in Figure 4.1 and they are defined as follows:

- The episodic time is the duration of each luminous episode, i.e, t_{on}.
- The duty cycle corresponds to the fraction of the quasar lifetime for which a quasar is shining and it is described as:

$$f_{\text{duty}} = t_{\text{on}}/\left(t_{\text{on}} + t_{\text{off}}\right) \tag{4.1}$$

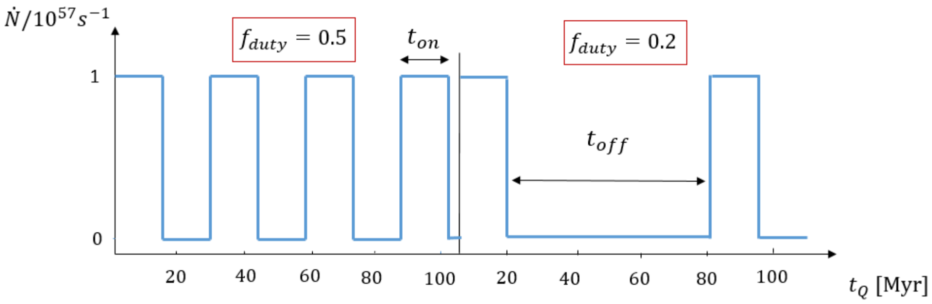

Figure 4.1: Illustration of the relevant parameters in the flickering model for a light curve. The figure shows the number of photons released by the source as a function of quasar lifetime.

Thus, in this work, we present a scenario described by a quasar that turns on and off periodically for a fixed duty cycle. During the quasar's active period, t_{on}, i.e, when it can be observed, it radiates continuously, ionizing its surroundings and increasing the He III fraction. Once it turns off, t_{off}, the He II fraction will settle down to its equilibrium value due to background ionization on a timescale of 10^6 years. The purpose of this section is to examine how the properties of the gas, the He II fractions, as well as the proximity zones behave under variability.

4.1 Behaviour of the He II fractions under variability

A comparison of the behavior of the He II fractions for the flickering and the lightbulb models is illustrated in figure 4.2. In the former, we chose the first consecutive on-time, off-time, and on-time episodes of the quasar.

- **First on-time episode**. In the top row, we see the development of the He II fraction for the first on-time episode compared to the lightbulb model for the same period. As we can see, the quasar behaves exactly like the constant model, regardless of the initial ionization background. Near the quasar almost the entire He II fraction oscillates between 10^{-5} - 10^{-6}, i.e. is fully ionized. As we move away from the quasar, the He II fraction restores the initial ionization conditions. For initial backgrounds where the He II fraction was higher, the change is more noticeable (see discussion in 3.2.1).

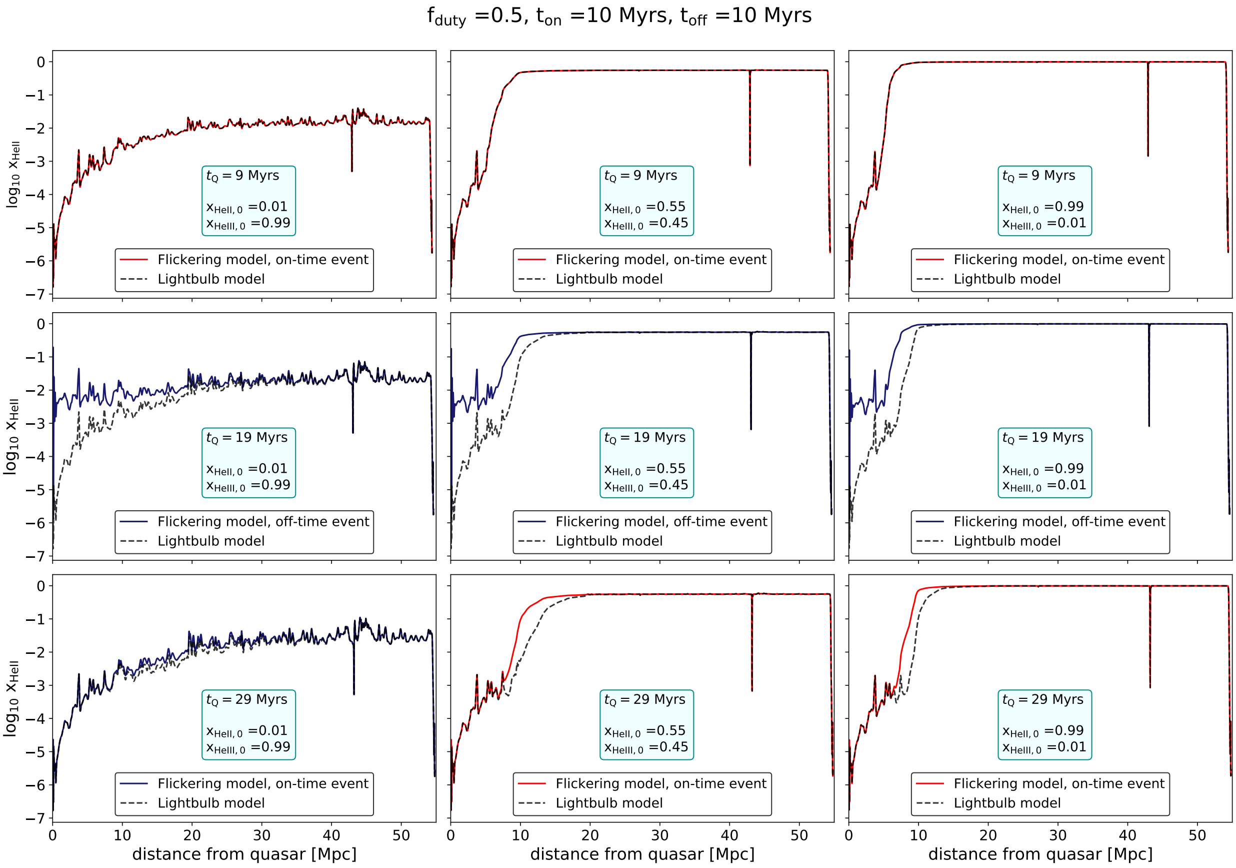

Figure 4.2: Evolution of the He II fraction as a function of the distance for a duty cycle of $f_{\text{duty}} = 0.5$, a quasar on-time of $t_{\text{on}} = 10$ Myr and a quasar off-time of $t_{\text{off}} = 10$ Myr. The top row of the figure shows the evolution of the He II fraction in response to the first on-time quasar episode in the flickering model along with the lightbulb model. The middle and bottom rows show the evolution of the He II fraction for both models for the first off-time quasar episode and the subsequent quasar on-time episode, respectively. Additionally, each column shows the evolution when different initial ionization backgrounds are considered. All of the models presented correspond to a quasar lifetime of 100 Myrs.

- **First off-time episode**. In the middle row, we see the evolution of He II during the time the quasar is switched off. In this quasar-free situation, there is no very remarkable evolution of the He II fraction as a function of distance. However, we see a detachment from the lightbulb model for short distances and different behavior compared to the previous on-time scenario. The degree of ionization is smaller, with values around $10^{-2} - 10^{-3}$ in all the cases. This is expected since there is no quasar present, although we can still see higher ionization at short distances in the lightbulb model. At longer distances, the He II faction restores the background conditions.
- **Second on-time episode**. The following on-time episode is shown in the bottom row. This situation is very similar to that in the upper row, except that this time we see a small

deviation from the lightbulb model. As the previous off-time episode was comparable to the equilibrium timescale, the gas in the IGM had time to recombine, so when the next on-time episode occurs, more work is needed to attain the previous on-time ionization state.

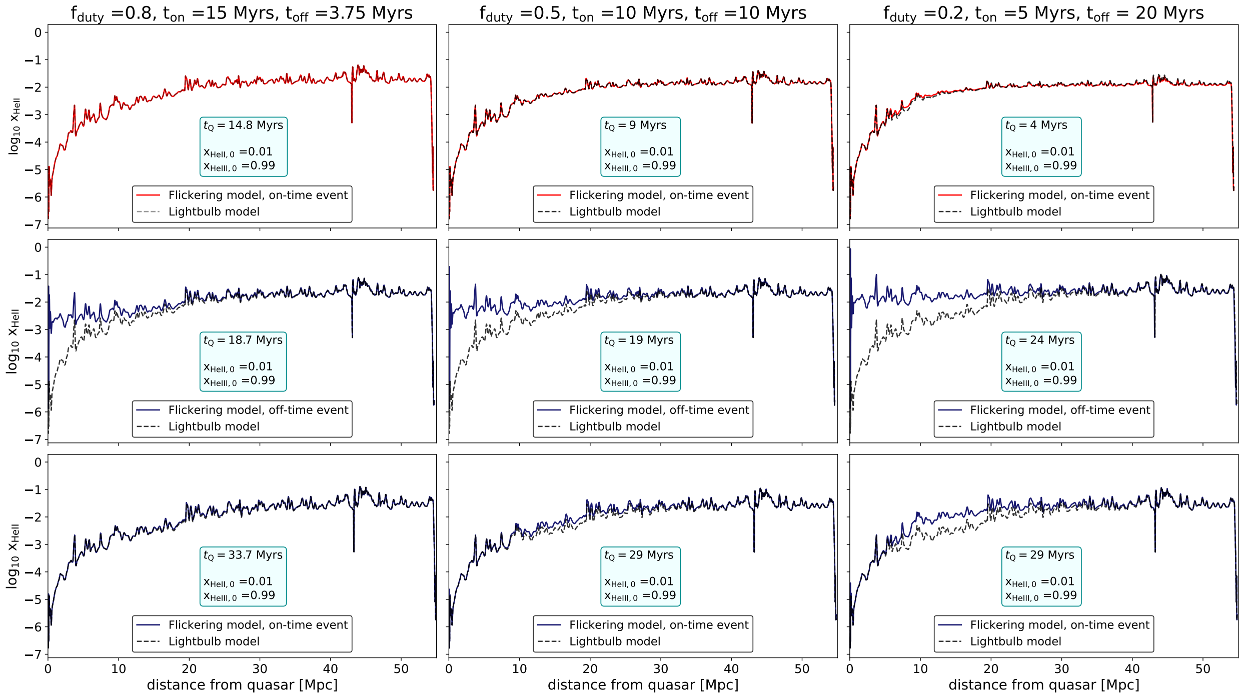

Figure 4.3: Evolution of the He II fraction as a function of the distance for different duty cycles, $f_{\rm duty} \in \{0.8, 0.5, 0.2\}$, quasar on-times $t_{\rm on} \in \{15, 10, 5\}$ Myrs and quasar off-times $t_{\rm off} \in \{3.75, 10, 20\}$ Myrs, respectively. The initial He I and He II fractions for all the models are $x_{\rm HeII,0} = 0.01$ and $x_{\rm HeIII,0} = 0.99$. The lightbulb model together with the flickering model for the first on-time quasar episode is shown in the top row. Similarly, the middle and the bottom rows show the He II fraction evolution for both models for the first quasar off-time and the subsequent quasar on-time episodes, respectively.

To understand how the He II fraction evolves as the quasar's duty cycles, on-times, and off-times change, we explore different models with duty cycle values between $\rm f_{duty} \in \{0.8, 0.5, 0.2\}$, quasar on-times $\rm t_{on} \in \{15, 10, 5\}$ Myrs and quasar off-times $\rm t_{off} \in \{3.75, 10, 20\}$ Myrs, respectively. This can be represented in figure 4.3. The top row of each model follows the He II fraction evolution for the first quasar on-time episode. According to our previous discussion, the on-time episode follows the same trend as the lightbulb model. It seems that the degree of ionization around a quasar barely varies from model to model. Conversely, in the middle row, the evolution of the He II fraction at the first off-time episode is illustrated. All the models in this situation exhibit very similar He II evolution, as expected in a quasar-free scenario. Additionally, the last row shows the consecutive on-time episodes. As shown in the previous figure, we see a small deviation from the lightbulb model, however, when the previous off-time episode is longer (third column), the deviation in the following on-time is larger. The reason for this is that after being absent for a prolonged time, quasars take longer to reestablish the previous on-time ionization conditions.

4.2 He II fluxes under variability

We will now explore the behavior of the He II transmission in the flickering model. The evolution of the He II fluxes as a function of the distance for a duty cycle of $f_{\rm duty} = 0.5$, an on-time $t_{\rm on} = 10$ Myr and an off-time $t_{\rm off} = 10$ Myr for different initial He II ionization fractions $x_{\rm HeII,0} \in \{0.01, 0.55, 0.99\}$ can be seen in figure 4.4.

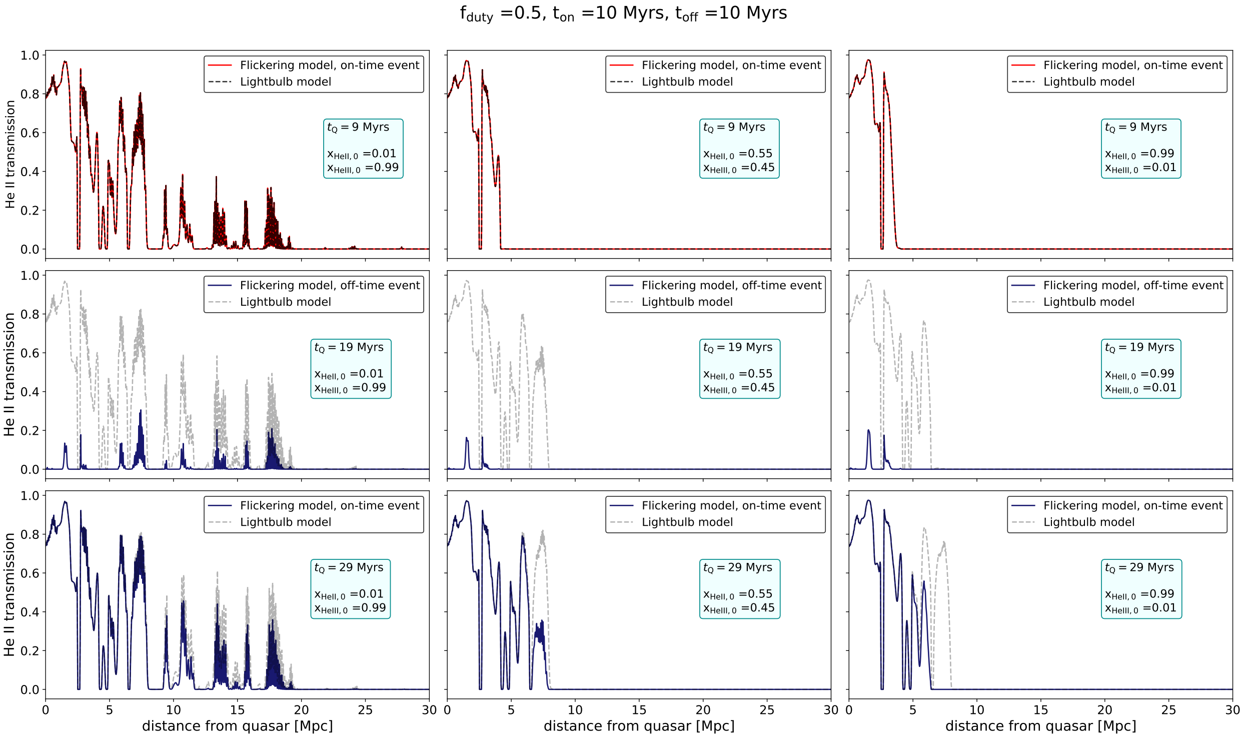

Figure 4.4: Evolution of the He II fluxes as a function of the distance for a duty cycle of $f_{\rm duty} = 0.5$, a quasar on-time of $t_{\rm on} = 10$ Myr and a quasar off-time of $t_{\rm off} = 10$ Myr.The top row of the figure shows the evolution of the He II fluxes in response to the first on-time quasar episode in the flickering model along with the lightbulb model. The middle and bottom rows show the evolution of the He II fluxes for both models for the first quasar off-time and the subsequent quasar on-time episodes, respectively. Additionally, each column shows the evolution when different initial ionization backgrounds are considered. All of the models presented correspond to a quasar lifetime of 100 Myrs.

- **First on-time episode**.The upper row shows the He II fluxes for the first on-time episode. As expected, the proximity zone signature is always visible due to the high ionization rate coming from the quasar at small radii following the same pattern as those predicted by the lightbulb model, although its size changes due to the different initial ionization states.

- **First off-time episode**. The second row shows He II fluxes in a quasar-free environment. In this case, there is no proximity zone signature and the tendency barely follows a lightbulb model as we would expect when there is no quasar. Moreover, the initial ionization states dominate those absorption lines that appear in all cases.
- **Second on-time episode**. On the bottom row, we can see the evolution of the He II fluxes for the next on-time episode. Compared to the previous on-time, in this case, we recover the proximity zone signature, but it diverges from the lightbulb model due to the time it takes for the intergalactic medium to restore the previous on-time ionization.

It must be emphasized that the quasar will only be detectable during the on-time episodes, the off-time fluxes are only shown here for illustration.

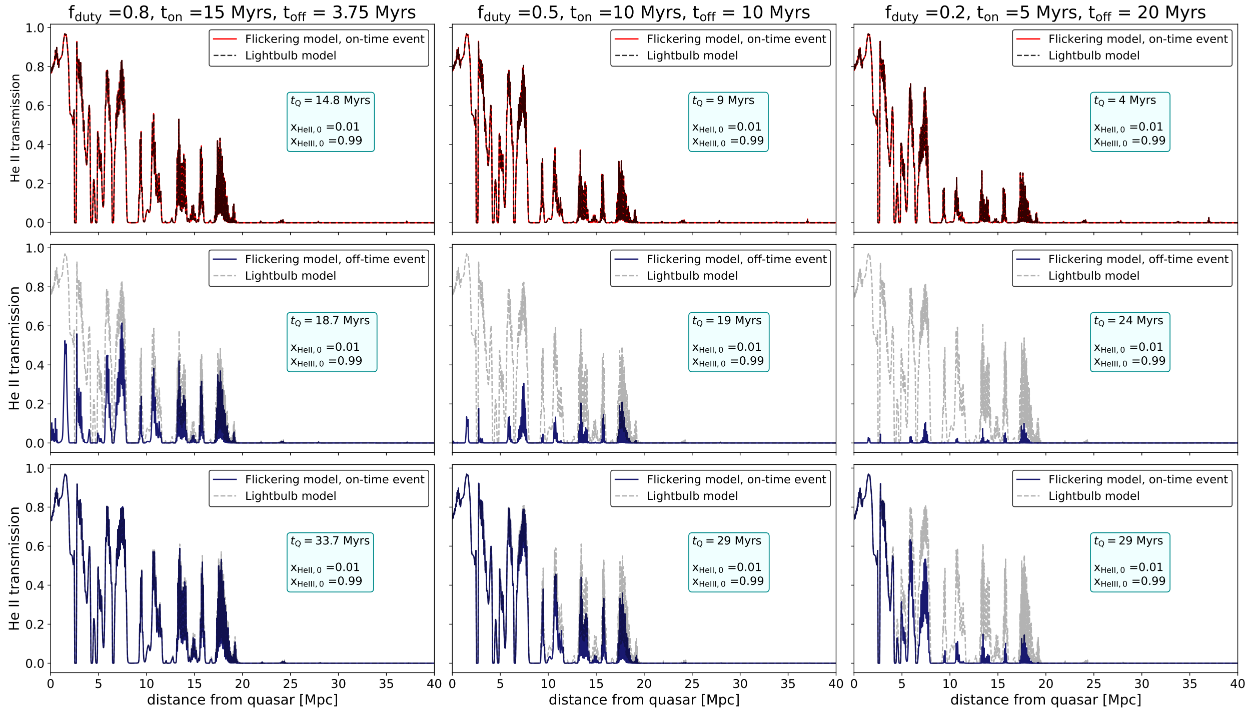

Figure 4.5: Evolution of the He II fluxes as a function of the distance for different duty cycles, $f_{\text{duty}} \in \{0.8, 0.5, 0.2\}$, quasar on-times $t_{\text{on}} \in \{15, 10, 5\}$ Myrs and quasar off-times $t_{\text{off}} \in \{3.75, 10, 20\}$ Myrs, respectively. The initial He I and He II fractions for all the models are $x_{\text{HeII},0} = 0.01$ and $x_{\text{HeIII},0} = 0.99$. The lightbulb model together with the flickering model for the first on-time quasar episode is shown in the top row. Similarly, the middle and the bottom rows show the He II fluxes evolution for both models for the first quasar off-time and the subsequent quasar on-time episodes, respectively.

Figure 4.5 shows the evolution of the He II fluxes for different duty cycles $\mathrm{f_{duty}} \in \{0.8, 0.5, 0.2\}$ and on-times $\mathrm{t_{on}} \in \{15, 10, 5\}$ Myrs. In all the cases, the He II fluxes behave very similarly to those explained before. We find, however, that for a longer duty cycle (first column), more absorption lines are seen in the off-time episode (middle row) and the He II transmission barely differs from the lightbulb model in the following on-time episode. This is because the quasar is off for such a short time that the IGM barely has time to adjust to a quasar-free scenario before it turns on again. On the other hand, the inverse situation is seen for a small duty cycle (third column). Here the quasar is off for 20 Myrs, so the IGM has enough time to settle to a new ionization state before the next on-time episode. As soon as the quasar is turned on again (third last row), we see that the He II transmission shifts from the lightbulb model. This is because the quasar had not enough time to ionize the IGM around it to the same extent as it did in the constant model.

4.3 Behaviour of the proximity zones under variability

In this section, the behavior of the proximity zones under variability will be discussed. Figure 4.6 displays an example derived from our simulations for one sightline in the upper panel and 100 sightlines in the middle panel. The duty cycle, in this case, is $f_{\mathrm{duty}} = 0.5$, the quasar on-time is $t_{\mathrm{on}} = 10$ Myrs, and the quasar off-time is $t_{\mathrm{off}} = 10$ Myrs. Both panels present a dashed blue line that represents the lightbulb model, which shows that when a quasar turns on, the proximity zone initially increases, but settles to a constant value after reaching equilibration, as discussed in section 3. On the other hand, the red solid line in both panels shows how the proximity zone changes as the source turn on and off periodically. In this case, the proximity zone is very close to the equilibrium values found by the constant model when the quasar is on. However, when the quasar turns off, all the gas close to it recombines, resulting in a reduction of the size of the proximity zone. This is due to the changes in the He III fraction and corresponding He II Lyα forest as discussed previously. Moreover, the bottom panel shows how the proximity zone sizes are distributed in this model for a magnitude of $\mathrm{M_{1450}} = -27$. The distributions are derived only when the black hole is shining and is accessible to the observer. Specifically, in this case, they correspond to the last accretion burst. The comparison of the constant and the variable distributions reveals that the variable model covers a broader range of small proximity zones than the lightbulb model. Thus, variability allows us to observe small proximity zones, even for the last accretion burst, which corresponds to a quasar lifetime of $t_{\mathrm{Q}} = 80 - 90$ Myrs.

To better understand the variability, we have proposed different models where we change duty cycles and quasar on-times using one and 100 sightlines. For instance, the figure 4.7 shows the evolution of the proximity zone as a function of the quasar lifetime for a fixed duty cycle $\mathrm{f_{duty}} = 0.2$ and different quasar on-times $\mathrm{t_{on}} \in \{5, 10, 15\}$ Myr. The top row shows the evolution of both the flickering quasar model represented by a solid red line and the lightbulb model by a dashed blue line along one sightline as before. Similarly, the middle row also shows both models, but in this case, the solid and dashed lines represent the median values for 100 sightlines. The first column illustrates the evolution for $\mathrm{t_{on}} = 5$ Myrs, i.e. the quasar is not on long enough to reach equilibrium, so each crest has a sharp tip. In this situation, the proximity zone increases

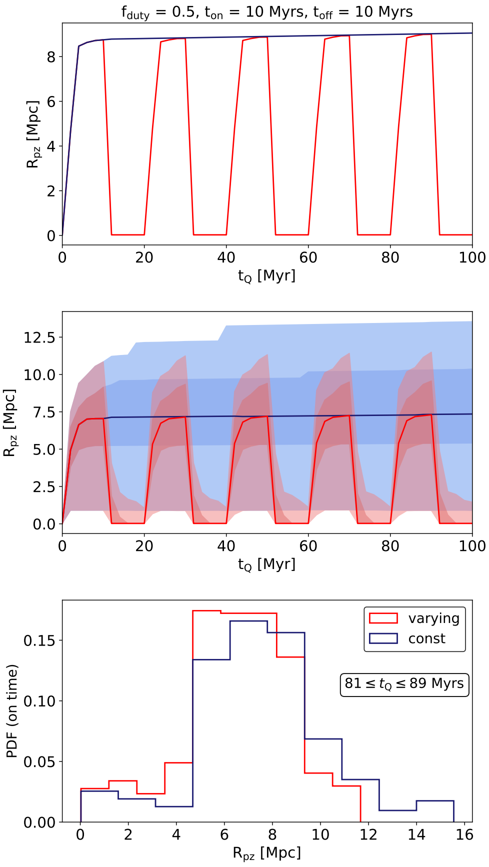

Figure 4.6: This figure shows the proximity zones as a function of the quasar lifetime for the lightbulb and flickering quasar models with $f_{\mathrm{duty}} = 0.5$, $t_{\mathrm{on}} = 10$ Myrs and $t_{\mathrm{off}} = 10$ Myrs. The blue dashed line represents the lightbulb model for one sightline in the upper panel and the median value of 100 sightlines in the middle panel. Additionally, the red line represents the flickering quasar model for one sightline in the upper panel, as well as the median of 100 sightlines in the middle panel. The dark and light blue/red shaded areas in the bottom panel correspond to 1σ and 2σ standard deviations of the $\mathrm{R_{pz}}$, respectively. The bottom panel shows the probability density function (PDF) of the proximity zones for the last accretion burst. The blue line represents the $\mathrm{R_{pz}}$ distribution for the lightbulb model, while the red line shows the $\mathrm{R_{pz}}$ distribution for the flickering model.

during the quasar on-time episode as the nearby gas is ionized, but the on-time is insufficient to reach an equilibrium value consistent with that found by the constant model. Immediately after the 5 Myrs, when the quasar shuts down, the proximity zone begins to decrease as the gas around the quasar recombines and returns to its original ionization state. The same situation applies to the second and third columns, however, in the third scenario, when the quasar on-time is 15 Myrs, we can observe flatter tips. The reason for that is that the quasar on-times are comparable to the equilibration timescale, i.e, the quasar radiates long enough for the proximity zones to reach an equilibration value, which is close to that found by the constant model.

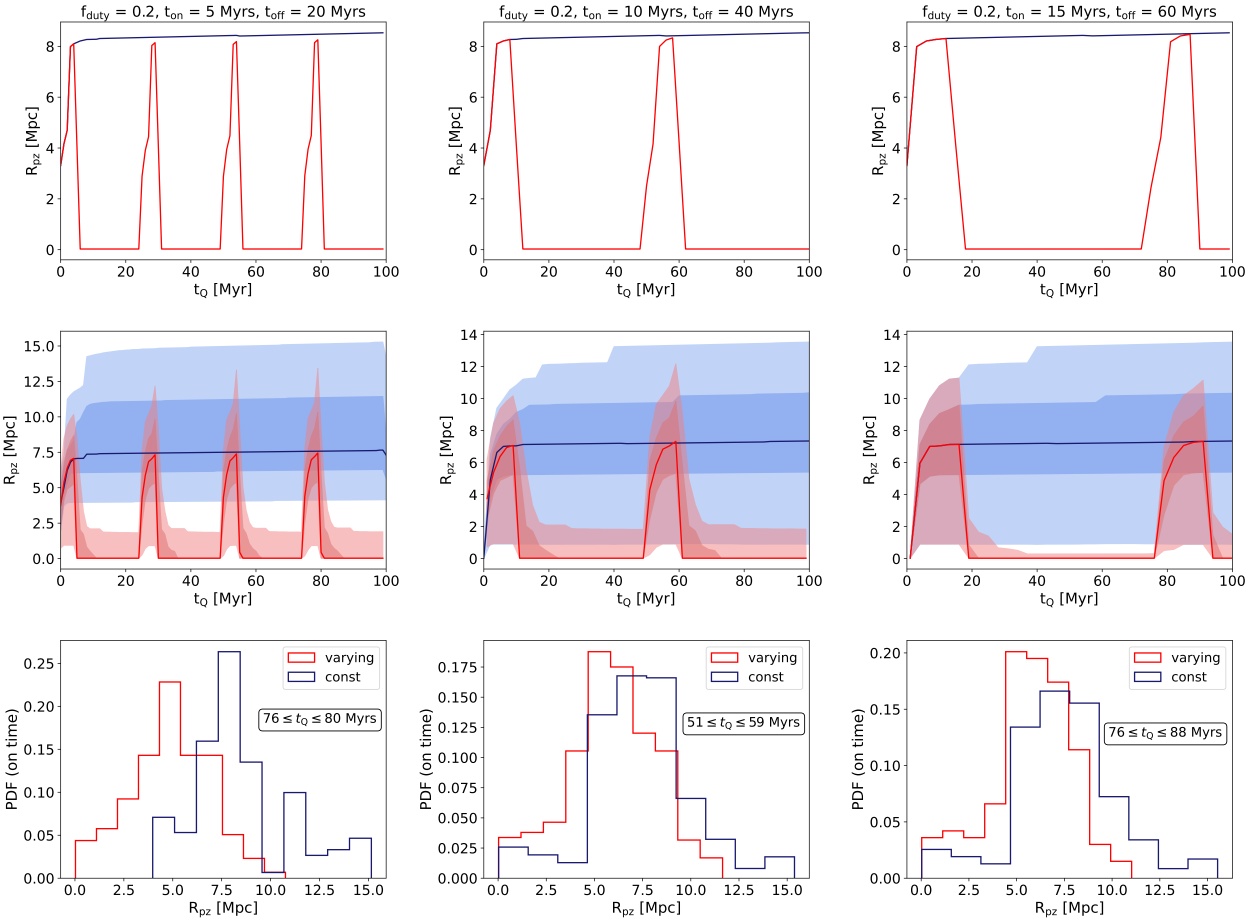

Figure 4.7: Evolution of the proximity zone as a function of the quasar lifetime for a fixed duty cycle $f_{\rm duty} = 0.2$ and varying on-time $t_{\rm on} \in \{5, 10, 15\}$ Myr. Both the flickering and lightbulb models, represented by the solid red and blue dashed lines along a line of sight, are shown in the top row. Similarly, the median values for 100 sightlines of the lightbulb and flickering quasar models are shown in the bottom row. The blue/red shaded areas correspond to 1-2σ standard deviations. The bottom panel shows the probability density function (PDF) of the proximity zones for the last accretion burst. The blue line represents the $R_{\rm pz}$ distribution for the lightbulb model, while the red line shows the $R_{\rm pz}$ distribution for the flickering model.

In all the cases, the quasar off-time is large enough for effective recombination to occur, restoring the He II fraction to its initial value before the start of its next on-time episode. In general, when the equilibration timescale is shorter than the time it is in the off state, the evolution of the proximity zone differs significantly from the evolution of the lightbulb model, as shown by the standard deviations, represented by the red/blue shaded regions in figure 4.7. In addition, the bottom panel shows the R_{pz} distributions for each case. For all models, t_{off} is long enough to allow the gas to adjust to the background photoionization rate, which reduces the proximity zone size and results in a larger small distribution than for the lightbulb model. Furthermore, this effect is even more prominent when the on-time episodes are also smaller, such as $t_{on} = 5$ Myrs. This is because the on-time is shorter than the equilibration timescale and thus, the proximity zone barely has time to grow too much before the off-time episode occurs, resulting in a small proximity zone. Hence, the probability density function has a larger distribution of small proximity sizes in the first model (first column) than in the other ones.

Another different scenario is shown in figure 4.8. In this case, the figure illustrates the evolution of the proximity zone as a function of the quasar lifetime for a fixed quasar on time $t_{on} = 15$ Myrs and different duty cycles $f_{duty} \in \{0.2, 0.5, 0.8\}$. As we can see, the quasar on time is comparable to the equilibration time scale in all models, and therefore the highest value of the proximity zone reaches the constant value given by the constant model. Additionally, with shorter quasar off times and longer duty cycles, the gas does not have enough time to recombine properly, allowing the quasar to better preserve the IGM ionization state in every on-time episode, causing fewer changes in the size of the proximity zones. In this case, the proximity zone could reach its lightbulb values. However, at shorter duty cycles and longer quasar off times, when the quasar is absent for a time comparable to the equilibration time scale, the IGM gas has enough time to recombine and hence the proximity zone becomes smaller until the He II fraction reaches its initial equilibrium values. In this situation, the proximity zone remains much smaller than its lightbulb value at all times. As compared to the previous analysis for figure 4.8 and looking at the standard deviation (shaded regions) in this situation, we can conclude that, overall, the evolution of the proximity zone is similar to that of the lightbulb model for off-times much smaller than the equilibration timescale. The distributions of the proximity zone sizes for each model are presented in the bottom panel. Following our previous discussion, in smaller duty cycles, the quasar is off for longer periods, allowing the proximity zone to disappear as the gas has sufficient time to adjust to the background photoionization rate, consequently, the distribution extends to smaller proximity zones for smaller duty cycles (first column) as it does for larger duty cycles (third column). The models discussed in this section as well as some extra ones explored in this project are shown in figure B.1. Similarly, the probability density functions (PDF) for all the models are shown in figure B.2.

As we did previously for the lightbulb model, we investigated the sizes of the proximity zones as a function of the quasar magnitude for the flickering model, which is shown in figure 4.9. This figure illustrates the average $R_{pz}(M_{1450})$ for different models with a He II fraction of $x_{HeII,0} = 0.1$. In this case, the RT models describe a quasar lifetime of $t_Q \in \{91, 94\}$ Myrs, corresponding to the last accretion burst episode, and are characterized by duty cycles of

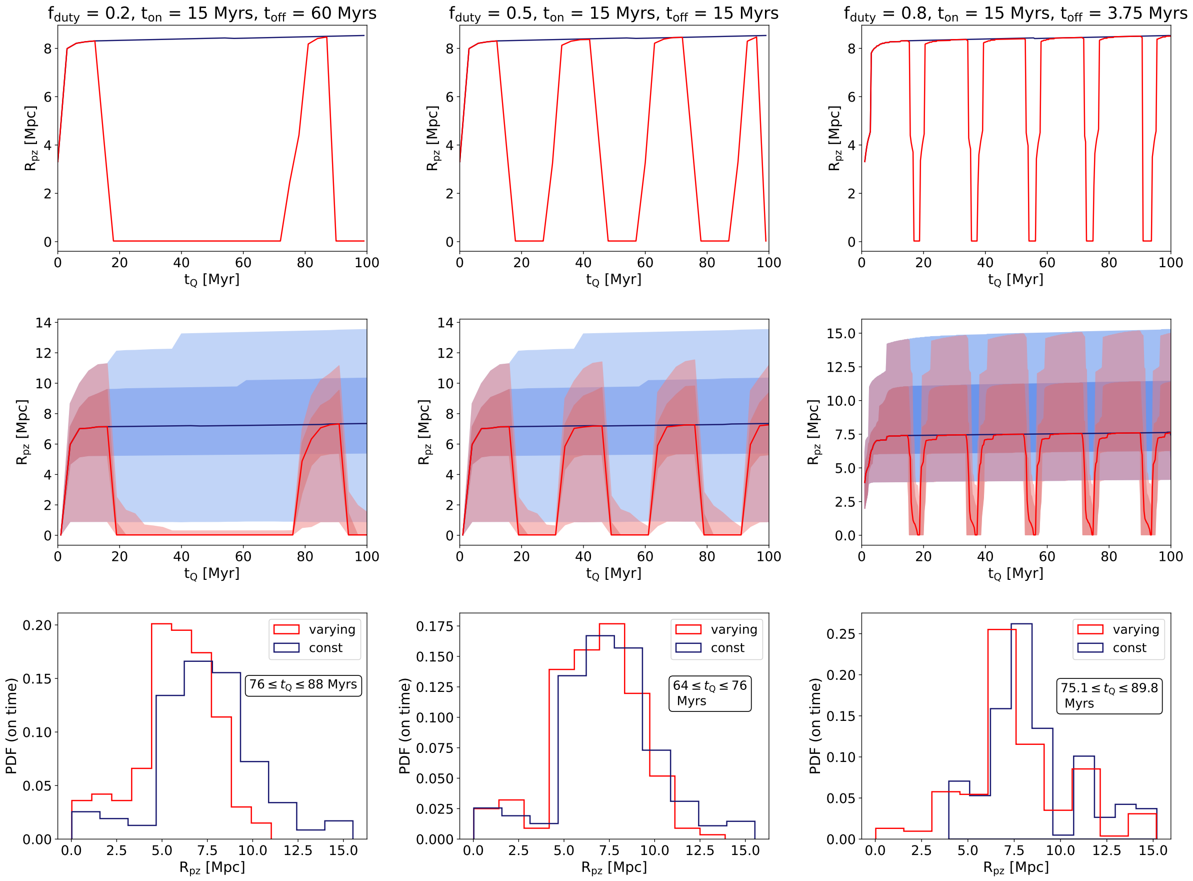

Figure 4.8: Evolution of the proximity zone as a function of the quasar lifetime for a fixed quasar on-time $t_{on} = 15$ Myr and varying duty cycle $f_{duty} \in \{0.2, 0.5, 0.8\}$. Both the flickering and lightbulb models, represented by the solid red and blue dashed lines along a line of sight, are shown in the top row. Similarly, the median values for 100 sightlines of the lightbulb and flickering quasar models are shown in the bottom row. The blue/red shaded areas correspond to 1-2σ standard deviations. The bottom panel shows the probability density function (PDF) of the proximity zones for the last accretion burst. The blue line represents the R_{pz} distribution for the lightbulb model, while the red line shows the R_{pz} distribution for the flickering model.

$f_{duty} \in \{0.1, 0.5\}$ and on times $t_{on} \in \{1, 5\}$ Myrs. Furthermore, we included observational data from Khrykin et al. (2019) and Worseck et al. (2021) in comparison with our two models. Interestingly, at all magnitudes, the large proximity zones were well predicted by the lightbulb approach and were consistent with flickering quasars with long on-times and larger duty cycles. However, smaller proximity zones cannot be fitted by lightbulb models (only for very short quasar lifetimes), but instead by flickering models with a small episodic on-time and a small duty cycle. In our case, the best fit occurs when the on-time is $t_{\rm on} = 1$ Myr and the duty cycle is $f_{\rm duty} = 0.1$. As the last quasar accretion event occurred between $88 \leq t_{\rm Q} \leq 91$ Myrs, we can conclude that when using the flickering quasar approach, we might measure small proximity zones for relatively long quasar lifetimes. The fact that those models with small duty cycles are the best fit would mean that the quasar is not accreting all the time, because the on-time episodes are also small. However, accretion from the black hole, and thus, an increase in growth may also occur during the off-time episodes, as discussed in Davies et al. (2019) and Worseck et al. (2021). Some theories attempt to explain the growth of black holes during off-time periods. For instance, according to Antonucci (1993), orientation effects can cause this, which means that the black hole continues to accrete and shine but not in the direction of the sightline considered. This phenomenon can also be attributed to small-scale physics near black holes, such as photon trapping, which occurs when photons are unable to escape because efficient accretion of an optically thick material prevents photon diffusion (Begelman 1979). In addition, obscuration can also be caused by dust accumulated near a supermassive black hole owing to supernovae (Yajima et al. 2017).

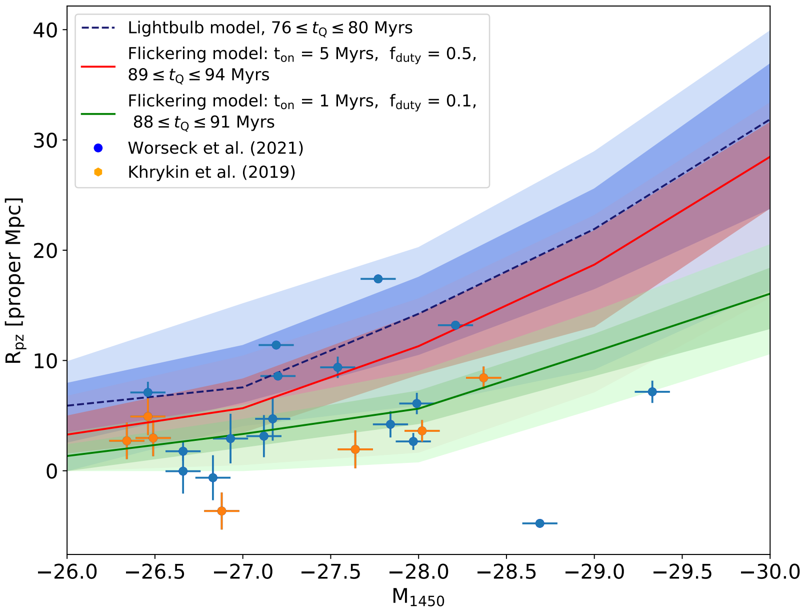

Figure 4.9: Representation of the He II proximity zone sizes $\mathrm{R_{pz}}$ as a function of the absolute magnitude $\mathrm{M_{1450}}$. The colored lines represent the average of $\mathrm{R_{pz}}$ including its 16-84th percentile scatter from the radiative transfer simulation at $\mathrm{z} = 3.2$ for the flickering and the lightbulb models. Some dataset observations are overplotted: the blue data points are taken from Worseck et al. (2021) and the yellow data points are from Khrykin et al. (2019). Both with their respective errors.

4.4 Summary

In this chapter, we have explored the proximity zones using the flickering model. We have learned about gas properties and fluxes when the source is periodically turned on and off. The study was conducted by varying the duration of the on-times and duty cycles. Similarly, the proximity zone behavior was analyzed, and we concluded that small duty cycles could produce small proximity zone sizes for long quasar lifetimes.

CHAPTER 5

CONCLUSIONS AND FUTURE WORK

This thesis presents the first study of varying sources and He II proximity zones in an attempt to reconcile the small observed proximity zone sizes with the growth time required for supermassive black holes. In the final section, we summarize the results obtained, including the caveats of this study, and suggest improvements for future research.

5.1 Results and conclusions

First, we used 100 sightlines from hydrodynamical simulations to make mock observations of the quasar absorption lines during the reionization of He II in the Universe at redshift 3.2. The goal of this part was to learn about the IGM through the calculation of optical depths and fluxes. As a first step, the codes were set up to run in a uniform density field, but because reionization occurs in an inhomogeneous manner in the universe, we adapted the code to include contributions from massive halos along the lines of sight in order to create a more realistic patchy He II reionization. Additionally, in the simulations, the initial ionization fractions of helium were varied to simulate the different IGM scenarios. We may conclude that in areas with high optical depths, the flux we receive is almost zero because those regions are less ionized; therefore, photons are more likely to be absorbed as they travel toward us. In contrast, those areas with low optical depth tend to be highly ionized, which allows photons to escape from possible absorption more easily, resulting in non-zero fluxes. Furthermore, a gas with a slightly higher overdensity will have a greater optical depth, which will result in a greater amount of Lyα forest absorption, and thus, lower transmission.

Proximity zones were introduced in the second part of the project as the distance between the quasar and the point at which the smoothed spectrum first dropped below 10%. Their presence was reflected in the quasar spectra as an increase in the He II transmission in the area closest to the quasar. Moreover, we studied the dependence of the proximity zone on the quasar lifetime, initial ionization fractions, luminosity, and density fields. As a first approach, we used a model that considers the quasar light curves constant over the quasar lifetime, called the lightbulb model. Some interesting conclusions were reached when studying the different dependencies:

- Studying the relationship between the proximity zone and the ionizing background resulted in an increase in transmission along the line of sight due to the existence of a small fraction of He II and a high fraction of He III. However, the study was extended to all sightlines for a better understanding, concluding that, overall, for long quasar lifetimes, the proximity zone size is not strongly dependent on the initial ionizing background.
- Our analysis of how proximity zones depend on quasar lifetimes concluded that they gradually grow in size during short quasar lifetimes because of changes in the ionization of the radiation field until they reach an equilibrium value. When this equilibrium is reached, the proximity zones become independent of the quasar lifetime.
- The dependence of the proximity zone on the luminosity was also explored. In this case, as expected, brighter quasars present a higher photon production rate, increasing the ionization rate, which in turn expands the proximity zone.

Moreover, we extend the study to all sightlines for various He II fractions and quasar lifetimes. None of the models based on the lightbulb approach can predict the observed small proximity sizes except for very short quasar lifetimes. In light of this, we conclude that we may not be correct when assuming constant light curves, leading us to change our approach.

In the third part, we investigate the proximity zones using the flickering model. Thus, we presented a scenario of a quasar that periodically turns on and off. The purpose of this part was to examine how the gas properties, He II fractions, and proximity zones behave under variability. The highlights of our study are as follows:

- Quasars behave very similarly to the lightbulb model during on-time episodes, regardless of the initial ionization background. However, the He II fraction did not exhibit a particularly remarkable evolution in the off-time episodes, although we observed a detachment from the lightbulb model at short distances and a different behavior when compared to the on-time scenarios, which was expected because there was no quasar present in this episode. Furthermore, we extended our study to different models by changing the duty cycles, as well as the duration of the on- and off-time episodes. We conclude that the evolution of the He II fraction and degree of ionization in all models behave as expected from the previous sections.
- The proximity zone was visible in the He II transmission for on-time episodes, with an expected change due to different ionization backgrounds. Conversely, off-time episodes lose this feature, leaving only absorption signatures that depend on the background ionization. In the case of off-time episodes, this feature disappears, leaving only some absorption signatures that depend on the initial ionization background. However, we must recall that quasars are not visible during off-episodes.

- By fixing different scenarios with different duty cycles and different quasar on and off times, we explored the behavior of the proximity zones under variability. The general conclusion is that the evolution of proximity zones depends to a large extent on whether the quasar on and off times are comparable to the equilibrium timescale. When the quasar is off for times longer than this timescale (smaller duty cycles), very effective recombination of the gas occurs, and the He II fraction returns to its original (quasar-free) state. Because of this efficient recombination of the gas, when the quasar is turned on again, more work is needed from the quasar to reach the same ionization state of the gas as in the previous on-time episode. Thus, the quasar on time must be long enough for the proximity zone to reach the equilibration values given by the light bulb model. Otherwise, the proximity zone will remain smaller than its light-bulb value at all times. However, when the quasar off-time is shorter than the equilibration timescale (larger duty cycles), the gas around the quasar does not have enough time to recombine, making it easier for the quasar to restore the gas to its previous ionization state in the next on-time episode. With a quasar on time greater than the equilibration timescale, the proximity zones will follow a very similar evolution to that of the light bulb model.

- When comparing our flickering models with some observations, we concluded that models with a small duty cycle of $f_{\rm duty} = 0.1$ and an on-time of $t_{\rm on} = 1$ Myr could produce small proximity zone sizes for long quasar lifetimes. Thus, a small quasar lifetime is not required in this approach, as for the lightbulb model, to explain the observations. In this case, the black holes have sufficient time to grow, and small proximity zones can still be observed.

5.2 Caveats and future work

As seen in this work, episodic light curves can be used to explain the small observed He II proximity zone sizes, even the observed H II proximity zones studied in other projects (Davies et al. 2019; Satyavolu et al. 2022). However, there are some limitations to our work that should be taken into consideration for future developments in this field to be successful. First, two factors determine the response of proximity zones to flickering light curves: the shape of the light curve and the ionization state of the IGM around the quasar. In this study, we assumed simple episodic light curves with constant burst durations for the on- and off-times along the sightline. However, this approach may not be the real case; instead, accretion and obscuration bursts may differ in duration along the same sightline. Additionally, the patchy morphology of helium reionization was not properly included because we set median values for the initial He II and He III fractions along the line of sight in all our radiative transfer models. To describe a more realistic scenario, future works might have to include fluctuations in the He fractions owing to this patchy environment. Finally, we compared our radiative transfer models with observational data. Nevertheless, one must consider the fact that the observed proximity zones have large redshift uncertainties, which limits our ability to precisely measure the lifetimes of individual quasars. Thus, in order to infer quasar lifetimes, we must ensure that we are comparing the right observational data with the right RT models; future research should focus on obtaining accurate redshifts of these and other He II quasars.

* * *

In conclusion, studying the absorption features in the spectra of the most distant quasars will greatly enhance our understanding of the physical mechanisms responsible for how galaxies and supermassive black holes evolve. Furthermore, the future generation of ground and space-based instruments will provide us with a wealth of information about the early stages of the evolution of the Universe. I am delighted to have been a part of this project, which has allowed me to deepen my knowledge of this field. This work represents only the beginning of a very long and exciting journey through the uncharted fields of Astrophysics.

BIBLIOGRAPHY

Ade, P. A. R., Aghanim, N., Arnaud, M., et al. 2016, Astronomy Astrophysics, 594, A13

Adelberger, K. L. & Steidel, C. C. 2005, The Astrophysical Journal, 630, 50

Aghanim, N., Akrami, Y., Ashdown, M., et al. 2020, Astronomy & Astrophysics, 641, A6

Alvarez, M. A., Wise, J. H., & Abel, T. 2009, ApJ, 701, L133

Antonucci, R. 1993, Annual Review of Astronomy and Astrophysics, 31, 473

Bañados, E., Venemans, B. P., Mazzucchelli, C., et al. 2018, Nature, 553, 473

Bañados, E., Venemans, B. P., Mazzucchelli, C., et al. 2017, Nature, 553, 473

Becker, G. D., Bolton, J. S., Madau, P., et al. 2015, MNRAS, 447, 3402

Begelman, M. C. 1979, MNRAS, 187, 237

Bolton, J. S. & Haehnelt, M. G. 2006, Monthly Notices of the Royal Astronomical Society, 374, 493

Bolton, J. S. & Haehnelt, M. G. 2007, Monthly Notices of the Royal Astronomical Society, 374, 493

Bolton, J. S., Puchwein, E., Sijacki, D., et al. 2016, Monthly Notices of the Royal Astronomical Society, 464, 897

Caleb, M., Flynn, C., & Stappers, B. W. 2019, Monthly Notices of the Royal Astronomical Society, 485, 2281

Chen, H. & Gnedin, N. Y. 2021, The Astrophysical Journal, 911, 60

Ciotti, L. & Ostriker, J. P. 2001, The Astrophysical Journal, 551, 131

Conroy, C. & White, M. 2012, The Astrophysical Journal, 762, 70

Cool, R. J., Kochanek, C. S., Eisenstein, D. J., et al. 2006, The Astronomical Journal, 132, 823

Davies, F. B., Hennawi, J. F., & Eilers, A.-C. 2019, ApJ, 884, L19

Davies, F. B., Hennawi, J. F., & Eilers, A.-C. 2019, Monthly Notices of the Royal Astronomical Society, 493, 1330

Dijkstra M., Prochaska, J. O. M. H. M. 2019, Lyman-alpha as an Astrophysical and Cosmological Tool

Eilers, A.-C., Davies, F. B., Hennawi, J. F., et al. 2017, The Astrophysical Journal, 840, 24

Eilers, A.-C., Hennawi, J. F., & Davies, F. B. 2018, The Astrophysical Journal, 867, 30

Eilers, A.-C., Hennawi, J. F., Decarli, R., et al. 2020, The Astrophysical Journal, 900, 37

Fan, X., Strauss, M. A., Becker, R. H., et al. 2006, AJ, 132, 117

Fechner, C. & Reimers, D. 2007, A&A, 463, 69

Fernandez-Soto, A., Barcons, X., Carballo, R., & Webb, J. K. 1995, Monthly Notices of the Royal Astronomical Society, 277, 235

Ferrara, A., Pettini, M., & Shchekinov, Y. 2000, Monthly Notices of the Royal Astronomical Society, 319, 539

Fukugita, M. & Peebles, P. J. E. 2004, The Astrophysical Journal, 616, 643

Furlanetto, S. R. & Oh, S. P. 2008, The Astrophysical Journal, 681, 1

Gnedin, N. Y. 2000, ApJ, 535, 530

Greig, B., Mesinger, A., & Bañados, E. 2019, Monthly Notices of the Royal Astronomical Society, 484, 5094

Gunn, J. E. & Peterson, B. A. 1965, ApJ, 142, 1633

Haardt, F. & Madau, P. 2012, ApJ, 746, 125

Haiman, Z., Wiklind, T., Mobasher, B., & Bromm, V. 2013, Astrophysics and Space Science Library, Vol. 396, The First Galaxies

Hao, J.-M., Yuan, Y.-F., & Wang, L. 2015, Monthly Notices of the Royal Astronomical Society, 451, 1875

Heisenberg, W. 1927, Zeitschrift fur Physik, 43, 172

Hennawi, J. F., Prochaska, J. X., Burles, S., et al. 2006, The Astrophysical Journal, 651, 61

Hogan, C. J., Anderson, S. F., & Rugers, M. H. 1997, AJ, 113, 1495

Hui, L. & Gnedin, N. Y. 1997, Monthly Notices of the Royal Astronomical Society, 292, 27

Inomata, K., Kawasaki, M., Kusenko, A., & Yang, L. 2018, Journal of Cosmology and Astroparticle Physics, 2018, 003

Khrykin, I. S. 2016, PhD thesis, The Faculty of Physics and Astronomy > Dekanat der Fakultät für Physik und Astronomie

Khrykin, I. S., Hennawi, J. F., McQuinn, M., & Worseck, G. 2016, The Astrophysical Journal, 824, 133

Khrykin, I. S., Hennawi, J. F., & Worseck, G. 2019, MNRAS, 484, 3897

Khrykin, I. S., Hennawi, J. F., Worseck, G., & Davies, F. B. 2021, MNRAS, 505, 649

King, A. & Nixon, C. 2015, Monthly Notices of the Royal Astronomical Society: Letters, 453, L46

Kirkman, D. & Tytler, D. 2008, Monthly Notices of the Royal Astronomical Society, 391, 1457

Liske, J. & Williger, G. M. 2001, Monthly Notices of the Royal Astronomical Society, 328, 653

Lodato, G. & Natarajan, P. 2006, Monthly Notices of the Royal Astronomical Society, 371, 1813

Lukić , Z., Stark, C. W., Nugent, P., et al. 2014, Monthly Notices of the Royal Astronomical Society, 446, 3697

Makan, K., Worseck, G., Davies, F. B., et al. 2021, ApJ, 912, 38

Martini, P. 2003, QSO Lifetimes

Martini, P. & Schneider, D. P. 2003, ApJ, 597, L109

McQuinn, M. 2016, Annual Review of Astronomy and Astrophysics, 54, 313

McQuinn, M., Lidz, A., Zaldarriaga, M., et al. 2009, The Astrophysical Journal, 694, 842

McQuinn, M. & Switzer, E. R. 2010, Monthly Notices of the Royal Astronomical Society, 408, 1945

Mellema, G., Iliev, I. T., Alvarez, M. A., & Shapiro, P. R. 2006, New Astronomy, 11, 374

Merloni, A. & Heinz, S. 2013, Evolution of Active Galactic Nuclei, ed. T. D. Oswalt & W. C. Keel (Dordrecht: Springer Netherlands), 503–566

Milosavljević, M., Bromm, V., Couch, S. M., & Oh, S. P. 2009, ApJ, 698, 766

Miralda-Escude, J. 1998, The Astrophysical Journal, 501, 15

Møller, P. & Kjaergaard, P. 1992, A&A, 258, 234

Morey, K. A., Eilers, A.-C., Davies, F. B., Hennawi, J. F., & Simcoe, R. A. 2021, The Astrophysical Journal, 921, 88

Nanayakkara, T., Brinchmann, J., Glazebrook, K., et al. 2020, The Astrophysical Journal, 889, 180

Omukai, K., Schneider, R., & Haiman, Z. 2008, The Astrophysical Journal, 686, 801

Planck, Aghanim, N., Armitage-Caplan, C., et al. 2014, Astronomy &amp Astrophysics, 571, A16

Power, C., Wynn, G. A., Combet, C., & Wilkinson, M. I. 2009, Monthly Notices of the Royal Astronomical Society, 395, 1146

Press, W. H. & Schechter, P. 1974, ApJ, 187, 425

Pritchard, J. R. & Loeb, A. 2012, Reports on Progress in Physics, 75, 086901

Prochaska, J. X., Hennawi, J. F., Lee, K.-G., et al. 2013, The Astrophysical Journal, 776, 136

Puchwein, E. & Springel, V. 2012, Monthly Notices of the Royal Astronomical Society, 428, 2966

Regan, J. A., Johansson, P. H., & Wise, J. H. 2014, The Astrophysical Journal, 795, 137

Reichardt, C. L., Patil, S., Ade, P. A. R., et al. 2021, The Astrophysical Journal, 908, 199

Rumbaugh, N., Shen, Y., Morganson, E., et al. 2018, The Astrophysical Journal, 854, 160

Ryden, B. 2003, Introduction to cosmology / Barbara Ryden. San Francisco, CA, USA: Addison Wesley, ISBN 0-8053-8912-1, 2003, IX + 244 pp.

Salpeter, E. E. 1964, ApJ, 140, 796

Sanderbeck, P. R. U., D'Aloisio, A., & McQuinn, M. J. 2016, Monthly Notices of the Royal Astronomical Society, 460, 1885

Satyavolu, S., Kulkarni, G., Keating, L. C., & Haehnelt, M. G. 2022, The need for obscured supermassive black hole growth to explain quasar proximity zones in the epoch of reionization

Schawinski, K., Evans, D. A., Virani, S., et al. 2010, The Astrophysical Journal, 724, L30

Schawinski, K., Koss, M., Berney, S., & Sartori, L. 2015a, Monthly Notices of the Royal Astronomical Society, 451

Schawinski, K., Koss, M., Berney, S., & Sartori, L. F. 2015b, Monthly Notices of the Royal Astronomical Society, 451, 2517

Schirber, M., Miralda-Escude, J., & McDonald, P. 2004, The Astrophysical Journal, 610, 105

Schmidt, T. M., Hennawi, J. F., Worseck, G., et al. 2018, The Astrophysical Journal, 861, 122

Shakura, N. I. & Sunyaev, R. A. 1973, A&A, 24, 337

Shen, Y., Strauss, M. A., Oguri, M., et al. 2007, The Astronomical Journal, 133, 2222

Shull, J. M., France, K., Danforth, C. W., Smith, B., & Tumlinson, J. 2010a, The Astrophysical Journal, 722, 1312

Shull, M., France, K., Danforth, C., Smith, B., & Tumlinson, J. 2010b, Hubble/COS Observations of the Quasar HE 2347-4342: Probing the Epoch of He II Patchy Reionization at Redshifts z = 2.4-2.9

Springel, V. 2005, Monthly Notices of the Royal Astronomical Society, 364, 1105

Springel, V., White, S. D. M., Jenkins, A., et al. 2005, Nature, 435, 629

Sunyaev, R. A. & Zeldovich, Y. B. 1980, MNRAS, 190, 413

Tanaka, T. L. 2014, Classical and Quantum Gravity, 31, 244005

Tsujikawa, S. 2003, Introductory review of cosmic inflation

Valiante, R., Schneider, R., Volonteri, M., & Omukai, K. 2016, Monthly Notices of the Royal Astronomical Society, 457, 3356

Viel, M., Becker, G. D., Bolton, J. S., & Haehnelt, M. G. 2013, Phys. Rev. D, 88, 043502

Viel, M., Haehnelt, M. G., & Springel, V. 2004, Monthly Notices of the Royal Astronomical Society, 354, 684

Visbal, E., Haiman, Z., & Bryan, G. L. 2014, Monthly Notices of the Royal Astronomical Society, 445, 1056

Vogelsberger, M., Marinacci, F., Torrey, P., & Puchwein, E. 2019, Cosmological Simulations of Galaxy Formation

Volonteri, M. 2010, A&A Rev., 18, 279

Volonteri, M. 2012, Science, 337, 544

Wang, F., Davies, F. B., Yang, J., et al. 2020, The Astrophysical Journal, 896, 23

Wang, F., Yang, J., Fan, X., et al. 2021, The Astrophysical Journal Letters, 907, L1

Wang, F., Yang, J., Fan, X., et al. 2019, The Astrophysical Journal, 884, 30

White, M., Martini, P., & Cohn, J. D. 2008, Monthly Notices of the Royal Astronomical Society, 390, 1179

White, S. D. M. & Rees, M. J. 1978, MNRAS, 183, 341

Worseck, G., Davies, F. B., Hennawi, J. F., & Prochaska, J. X. 2019, The Astrophysical Journal, 875, 111

Worseck, G., Khrykin, I. S., Hennawi, J. F., Prochaska, J. X., & Farina, E. P. 2021, Monthly Notices of the Royal Astronomical Society, 505, 5084

Worseck, G., Prochaska, J. X., Hennawi, J. F., & McQuinn, M. 2016, The Astrophysical Journal, 825, 144

Worseck, G., Prochaska, J. X., McQuinn, M., et al. 2011, The Astrophysical Journal, 733, L24

Worseck, G., Prochaska, J. X., O'Meara, J. M., et al. 2014, Monthly Notices of the Royal Astronomical Society, 445, 1745

Wu, X.-B., Wang, F., Fan, X., et al. 2015, Nature, 518, 512

Yajima, H., Ricotti, M., Park, K., & Sugimura, K. 2017, The Astrophysical Journal, 846, 3

Zheng, W., Meiksin, A., & Syphers, D. 2019, The Astrophysical Journal, 883, 123

Zheng, W., Syphers, D., Meiksin, A., et al. 2015, The Astrophysical Journal, 806, 142

APPENDIX A

ZUSAMMENFASSUNG

Der letzte große Phasenübergang im Universum fand während der Ära der Helium-Reionisierung statt. Harte Photonen wurden von Quasaren, welche von supermassereichen Schwarzen Löchern angetrieben werden, erzeugt und ionisierten das Helium im intergalaktischen Medium doppelt. Beobachtungen des He-II-Lyman-α-Waldes, eines Musters von Absorptionslinien in den Spektren dieser Quasare, können Aufschluss über den Ionisationsgrad des intergalaktischen Mediums bei diesen Rotverschiebungen geben. Insbesondere weisen die Regionen, die den Quasaren am nächsten liegen, einen höheren Ionisationsgrad auf. Dieser Effekt wird durch Photonen verursacht welche direkt von den Quasaren kommen. Solche Regionen werden als "Proximity Zones", also Nahzonen, bezeichnet und ihre Größe wird durch die Eigenschaften des intergalaktischen Mediums sowie den Eigenschaften des Quasars selbst bestimmt. In diesem Projekt wollen wir diese Nahzonen modellieren und ihren Einfluss auf den He-II-Lyman-α Wald analysieren. Eine Kombination aus kosmologischen hydrodynamischen Simulationen und 1D-Strahlungstransportrechnungen wird verwendet, um synthetische Beobachtungen des He-II-Lyman-α-Waldes zu machen. Diese dienen dazu, die Größe der simulierten Quasar-Nahzonen zu messen und mit echten Beobachtungen zu vergleichen. In dieser Arbeit wurden zwei verschiedene Ansätze verfolgt. Im ersten Fall betrachten wir konstante Quellen, man spricht auch vom "Glühbirnenmodell", bei dem die Leuchtkraft des Quasars konstant bleibt, sobald der Quasar erstmals aktiv wird. Im zweiten Fall wird von variierenden Quellen ausgegangen, dem sogenannten "flackernden Modell", bei dem sich die Leuchtkraft des Quasars als Reaktion auf die Änderung der Akkretionsrate ändert. Unsere Untersuchung zeigt, dass ein flackerndes Lichtkurvenmodell mit einem großen Anteil im hellen Zustand von $f_{\rm duty} = 0.5$ und einer "Einschaltdauer" von jeweils 5 Megajahren (Ma) die größeren beobachteten Nahzonen bei einer langen Quasarlebensdauer von $89 \leq t_{\rm Q} \leq 94$ Ma erklären kann. Im Gegensatz dazu kann ein kleiner Anteil im hellen Zustand von $f_{\rm duty} = 0.1$ und eine Einschaltdauer von jeweils 1 Ma die kleineren Nahzonen, die während der Helium-Reionisierungsepoche gemessen werden, auch für eine lange Quasarlebensdauer von $88 \leq t_{\rm Q} \leq 91$ Ma erklären. Nach diesem Modell können Schwarze Löcher also über längere Quasarlebensdauern hinweg wachsen, und es lassen

sich dennoch auch kleine Nahzonen beobachtet.

APPENDIX B

FLICKERING MODELS AND PROXIMITY ZONE DISTRIBUTIONS

For completeness, in this section, we include all the flickering models we studied during this project, along with their proximity zone distributions.

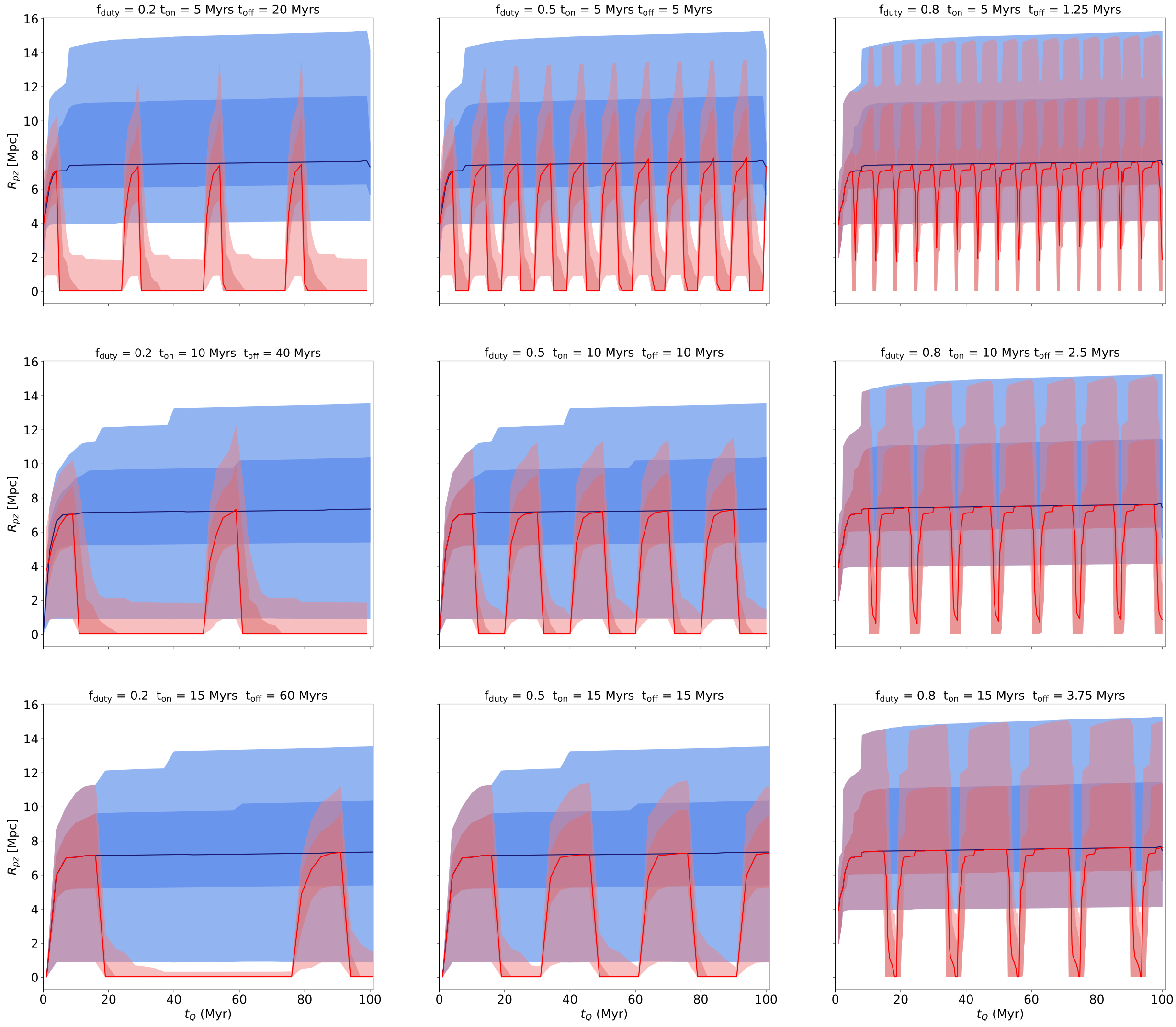

Figure B.1: Evolution of the proximity zone sizes as a function of the quasar lifetime for different duty cycles and quasar on-times. The blue and red solid lines represent the median of 100 sightlines for the lightbulb and the flickering model, respectively. In addition, the dark and light blue/red shaded areas correspond to 1σ and 2σ standard deviations.

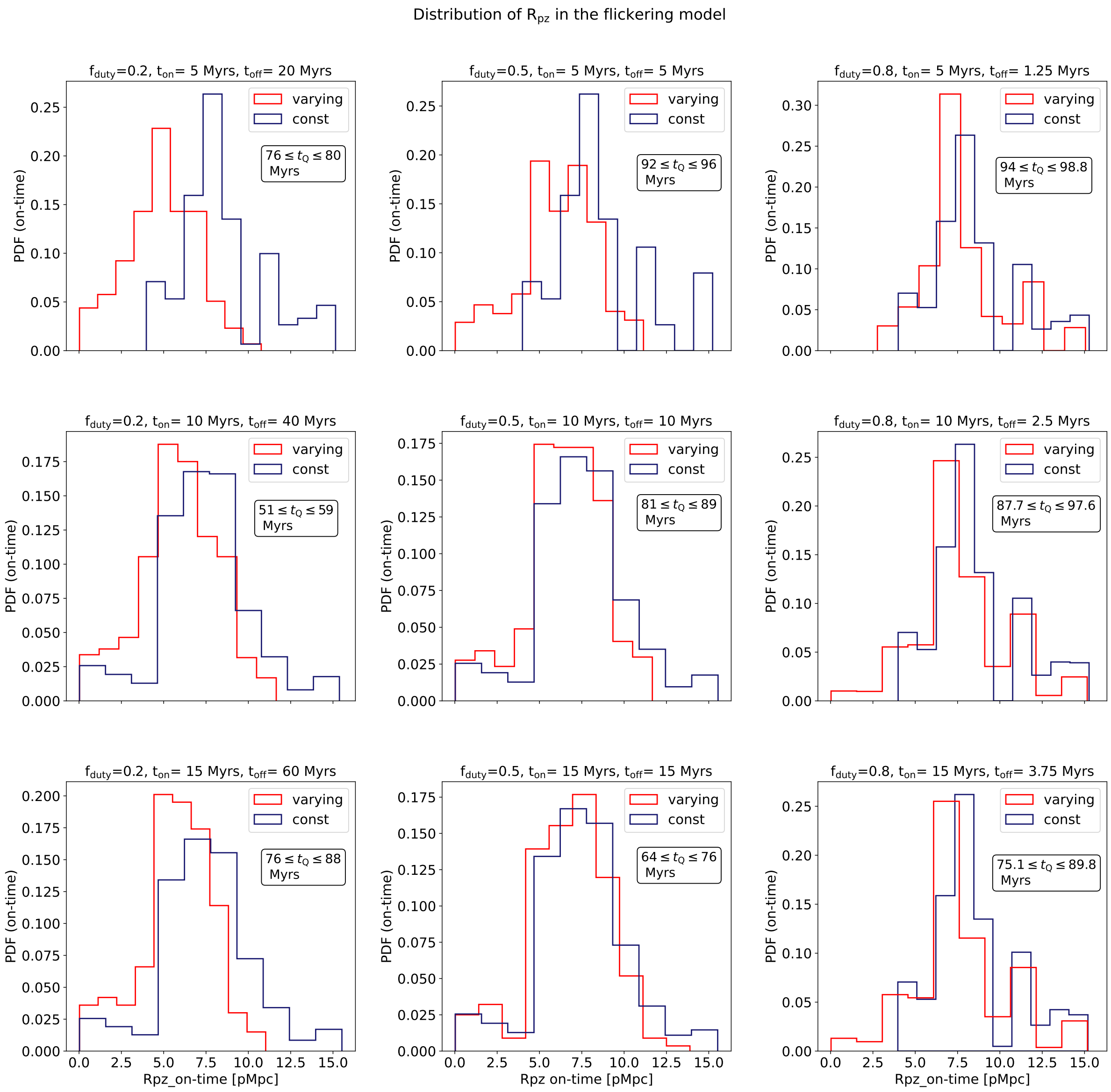

Figure B.2: Probability density functions (PDF) of the proximity zone sizes for different duty cycles and quasar on-times. The blue and red solid lines illustrate the lightbulb and the flickering model, respectively.